Characteristic angle-beta concept in electron arc therapy

Vlado Robar

Medical Physics Unit

McGill University, Montréal

December 1995

A Thesis submitted to the Faculty of Graduate Studies and Research in partial fulfilment of the requirements for the degree of Master of Science

National Library
of Canada

Acquisitions and
Bibliographic Services Branch

395 Wellington Street
Ottawa, Ontario
K1A 0N4

Bibliothèque nationale
du Canada

Direction des acquisitions et
des services bibliographiques

395, rue Wellington
Ottawa (Ontario)
K1A 0N4

Your file Votre référence

Our file Notre référence

ISBN 0-612-19847-2

Canada

Abstract

Electron arc therapy is the treatment of choice for tumours involving large curved surfaces. At the Montreal General Hospital a unique approach to the electron arc therapy was developed in 1986 and has been used clinically ever since. The approach is based on the concept of the characteristic angle beta.

We measured radial percentage depth doses in a polystyrene cylindrical phantom irradiated with electron arc beams having angles beta in the range from 5° to 100°, for 9 MeV, 12 MeV, 15 MeV, and 18 MeV electron beam energies. We showed that the characteristic angle-β concept can be extended to the beams with nominal energy of 18 MeV. The validity of the empirical relationship, relating the doses in two beams with different energies, was confirmed. A linear relationship between the angle β and the depth of dose maximum, the depth of the 85% depth dose, and the depth of the 50% depth dose, was established. The surface dose dependence on the angle β was also determined and the bremsstrahlung contamination in the electron arc therapy studied.

Résumé

L'électronthérapie en arc est le traitement de choix pour les larges tumeurs de surface courbée. À l'Hôpital Général de Montréal une approche unique au traitement en arc, fondée sur le concept de l'angle caractéristique, a été developpée en 1986 et est utilisée depuis ce temps.

Nous avons mesuré les rendements en profondeur radiaux dans un phantom cylindrique de polystyrène, lorsqu'irradié par des faisceaux d'électrons en arc, ayant des angles β de 5° à 100°. Les énergies des faisceaux d'électrons utilisées sont celles disponibles à partir d'un accélérateur linéaire Clinac-18 (9 MeV, 12 MeV, 15 MeV et 18 MeV). Nous avons démontré que le concept de l'angle charactéristique peut être étendu aux faisceaux d'énergie nominale de 18 MeV. Nous avons confirmé la relation empirique reliant la dose obtenue à partir d'un faisceau d'énergie quelconque, à celle d'un autre faisceau d'énergie différente. Nous avons trouvé des relations linéaires entre l'angle β et la profondeur de dose maximale, ainsi que celle du rendement en profondeur de 85% et celle de 50%. La dépendance de la dose en surface avec l'angle β fut determinée. Finalement, nous avons étudié la contamination en rayonnement de freinage inhérente à l'électronthérapie en arc.

Povzetek

Elektronska ločna terapija je namenjena za zdravljenje tumorjev, ki zajemajo velike, ukrivljene površine. V Splošni bolnišnici v Montrealu, Kanada, so razvili edinstven pristop k elektronski ločni terapiji leta 1986 in ga od takrat uspešno klinično uporabljajo.

Izmerili smo radialne odstotke globinskih doz v polistirenskem cilindričnem fantomu, obsevanem z elektronskimi ločnimi žarki s karakterističnimi koti beta med 5^0 in 100^0 ter z elektronskimi energijami 9 MeV, 12 MeV, 15 MeV in 18 MeV. Pokazali smo, da lahko koncept karakterističnega kota beta raztegnemo na elektronske žarke z nominalno energijo 18 MeV. Preverili smo veljavnost empirične enačbe, ki povezuje dozi dveh žarkov z različnimi energijami. Ugotovili smo linearno zvezo med kotom beta in globino doznega maksimuma, globino 85% globinske doze ter globino 50% globinske doze, respektivno. Določili smo tudi odvisnost površinske doze od kota beta in študirali kontaminacijo z zavornim sevanjem v elektronski ločni terapiji.

Acknowledgments

I want to acknowledge the contributions of several people without whom this thesis could not have been completed. First I want to thank my supervisor, Professor Ervin B. Podgorsak, for his help, guidance, and his readiness for discussion throughout the last year. If it had not been for Dr. Podgorsak, I would not have come to study in Canada in the first place. The thesis has been completed at the Medical Physics department of the Montreal General Hospital with the financial support from the Medical Research Council of Canada through Dr. Podgorsak.

I learned the TLD analysis from the clinical physicist Ms. Marina Pla. She was instrumental in developing the characteristic angle β approach at McGill University and introduced me to the practical aspects of electron arc irradiation in phantoms and to clinical applications of the electron arc therapy. The discussion of the TLD energy response with her is also sincerely appreciated.

Clinical physicist Mr. Michael D.C. Evans was always ready to help me, particularly concerning the use of the Markus chamber and the ophthalmic applicator. Mr. Joe Larkin took care of my old Mac whenever it showed tendency to shut down forever. Mr. Corey Zankowski performed the required Monte Carlo simulations and contributed Figure 2.2 to the thesis. I am taking this opportunity to thank my fellow students Messrs. Arthur Curtin-Savard, François DeBlois, Tony Falco, Normand Frenière and Dimitre Hristov, for making my two years in Montreal, despite homesickness, reasonably pleasant. My sincere appreciation goes to Ms. Lyssanne Normandeau, Ms. Micheline Gosselin and Mr. Normand Frenière for helping me to translate the abstract into French.

I also thank the Institute of Oncology in Ljubljana, Slovenia, for giving me the opportunity to study at McGill, and my colleagues at the Institute's Radiophysics department, especially Dr. Marko Habič, for encouraging me to complete my studies at McGill and for staying in touch with me.

Finally I want to thank Sabina for all her love despite 6500 kilometres separating us.

Table of contents

Chapter 1
Introduction

1.1 Radiotherapy

Radiotherapy is one of the three modern modalities for treating malignant diseases. The other two modalities are surgery and chemotherapy. Over 50% of cancer patients are treated with radiotherapy alone or in conjunction with the other two cancer therapy modalities. The aim of radiotherapy is to eradicate the tumour by means of ionizing radiation while minimizing the radiation damage to normal tissue surrounding the tumour.

A beam of high energy rays or particles (X rays, γ rays, neutrons, electrons, protons, pions, heavy ions...) is brought into a tumour volume which has been previously determined by a radiation oncologist. The amount of radiation delivered to the tumour (called the dose) is limited by the relationship between the local tumour control probability which increases with increasing dose, and the probability of radiation induced complications which also increases with increasing dose. The dose is by definition the energy absorbed per unit mass of the absorbing medium and its unit is Gray (1 Gy = 1 J/kg). This relationship for a typical tumour is illustrated in Fig. 1.1. Through decades of clinical research in radiation oncology the appropriate dose and dose delivery regimen have been determined for treatment of different anatomical sites.

Ionizing radiation can be delivered either from an internal source of radiation (brachytherapy) or from an external source of radiation (teletherapy). Internal sources are radionuclides inserted directly into cavities in human body (for example, oral and nasal cavity, esophagus, lungs, rectum, vagina), or they are inserted into the body interstitially placed inside needles or surgically implanted applicators. The most frequently used

brachytherapy sources are iridium-192, cesium-137, iodine-125, gold-198, cobalt-60, and strontium-90 sources.[1] They all emit γ rays, except for strontium-90 which is a pure emitter of β particles .

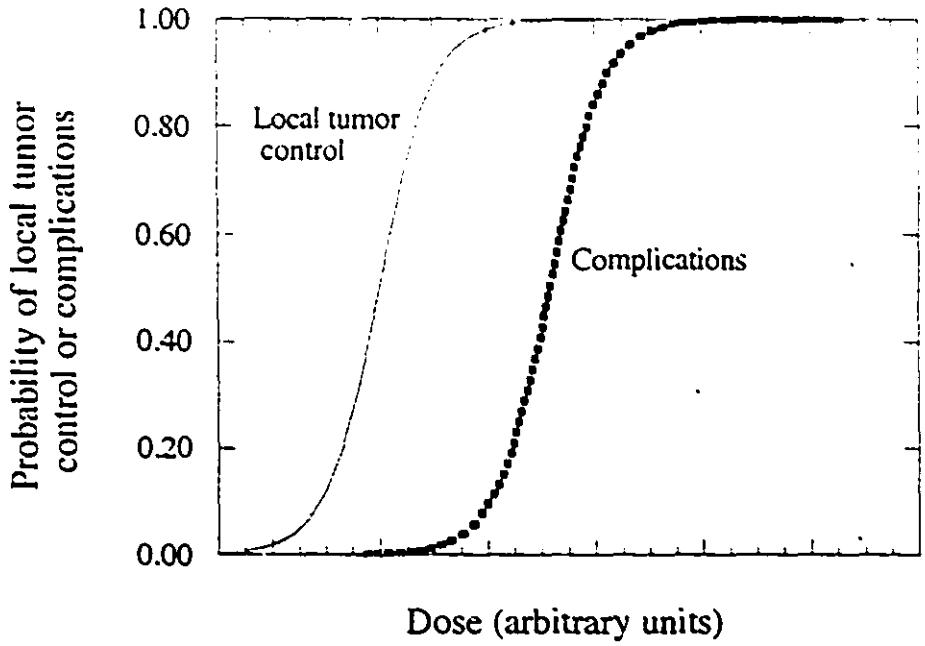

Figure 1.1 Probability of local tumour control and probability of complications are both sigmoid functions of absorbed dose. If the two curves are well separated, a high rate of tumour control can be achieved with a small complication rate. The closer together are the two curves, the more difficult it is to achieve a maximum tumour control with a low morbidity.

An isotope source, a particle accelerator, or a nuclear reactor may be used as an external source of ionizing radiation. In the past, radium-226 and cesium-137 units had been used as sources of γ rays, but in recent decades they have been largely replaced by cobalt-60 units. The average energy of photons from radium-226, cesium-137, and cobalt-60 is 0.83 MeV, 0.662 MeV, and 1.25 MeV, respectively.[1]

The particle accelerators, most frequently met in contemporary radiation therapy, are electron accelerators. They have been installed in the majority of modern radiation therapy centres in the developed world. On the other hand, other accelerators like proton, pion, and heavy ion accelerators offer exotic and very expensive treatment modalities, and have been installed in a few prestigious, research-oriented centres in the developed countries.

Electron linear accelerators are used to produce high energy electron beams with sharply defined kinetic energies in the range between 5 MeV and 35 MeV. Furthermore, if a high energy electron beam impinges on a target, megavoltage X rays (bremsstrahlung) are produced through the radiation losses of electrons in the target. This makes modern electron accelerators capable of producing electron beams as well as photon beams.

Megavoltage photon beams and electron beams are by far the most frequently used radiotherapy modalities. Both types of beams are characterized by their respective percentage depth dose curves, which illustrate the energy deposition characteristics and the penetration of the beams in tissue.

Megavoltage photon beams are usually used for treatments of deep seated tumours in the form of a single field, a parallel opposed pair of fields, a four field box, or some other even more complicated irradiation technique, such as total body irradiation, radiosurgery, or conformal radiotherapy. On the other hand, due to their finite range, electron beams are mainly used for treatments of superficial lesions which do not extend deeply under the skin surface, such as the treatment of skin and lip cancer, chest wall irradiation after mastectomy, or treatment of head and neck cancer. Electron beams are also employed for some special irradiation procedures, such as total skin irradiation and electron arc therapy.

1.1.1 Photon beams

In Fig. 1.2. we show characteristic percentage depth dose curves for two clinical photon beams. One is a cobalt-60 beam and the other a 10 MV photon beam produced in a Varian Clinac-18 linear accelerator. A small surface dose is characteristic for megavoltage photon beams and this so called *skin-sparing effect* is very important in radiotherapy. Beyond the surface, the dose sharply increases to the depth of dose maximum, and this region of dose increase with depth is referred to as the build-up region. The surface dose and depth of dose maximum are functions of field size and beam energy. For constant field size the surface dose decreases and the depth of dose maximum increases with increasing beam energy. For example, the depth of dose maximum is 5 mm for cobalt-60 beams and 4 cm for 25 MV photon beams. Beyond the depth of dose maximum the dose falls off approximately exponentially with depth. The spectrum of a given photon beam does not change appreciably as the beam penetrates into medium.

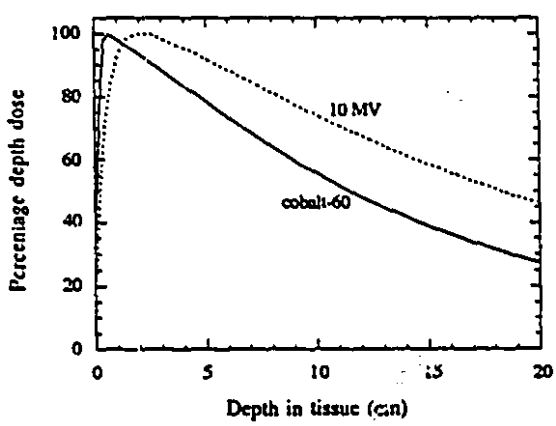

Figure 1.2 Percentage depth doses for a cobalt-60 beam (solid curve) and a 10 MV photon beam (dotted curve). For both beams the field size is 10×10 cm^2. For the cobalt-60 beam the source-skin distance (SSD) is 80 cm and for the 10 MV beam it is 100 cm.

1.1.2 Electron beams

As evident from Fig. 1.3, which shows a typical electron beam depth dose distribution, the penetration characteristics of high energy electron beams are quite different from those of megavoltage photon beams. Electron beams exhibit a large surface dose which is equal to ≈ 80% for 6 MeV electron beams and ≈ 95% for 22 MeV electron beams. This makes electron beams convenient for skin treatment (in contrast to low surface percentage dose for megavoltage X-ray beams, which is desirable for treatments where skin is not affected by disease - skin sparing effect). Generally, the surface dose of electron beams increases with increasing beam energy, in contrast to the behaviour of megavoltage X-ray beams.

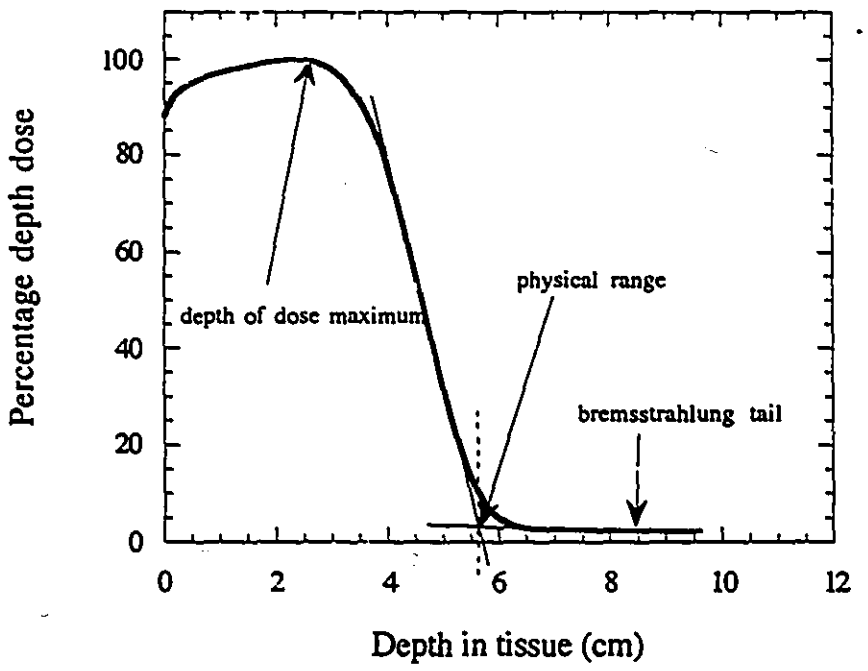

Figure 1.3 A typical percentage depth dose curve for a clinical electron beam: kinetic energy = 12 MeV, field size = 10×10 cm^2, SSD = 100 cm. Characteristic features of clinical electron beams such as the depth of dose maximum, physical range, and bremsstrahlung tail are shown.

In electron beams, the dose slowly increases from the surface to the depth of dose maximum. Percentage depth dose is relatively homogeneous up to a certain depth, and then sharply decreases to a value of just a few percent near the depth equal to the physical range of electrons R_p in the absorbing medium. Usually the depth of the 85% depth dose, R_{85}, is considered to be a clinical limit of relevance, and is referred to as the treatment range. R_{85} as well as R_p are proportional to the incident energy of the electron beam, therefore the beam with the best clinical properties for a particular treatment can be chosen out of a variety of beams provided by modern linear accelerators. The depth at which this sharp slope of percentage depth dose curve ends characterizes the physical range R_p of a particular electron beam. Beyond the physical electron range R_p the dose is equal to only a few percent of the maximum dose. This small remaining dose is due to the photon contamination of the electron beam. Energetic electrons lose a portion of their energy in the form of bremsstrahlung interacting with the atomic nuclei in the linac's head, air, and also inside the patient. This bremsstrahlung forms a continuous spectrum of X rays with the maximum spectrum energy equal to the maximum kinetic energy of electrons. Because the bremsstrahlung production increases linearly with the atomic number of interacting nucleus Z, a major contribution to the photon contamination originates in the collimator jaws of the linac. The percentage of bremsstrahlung dose contribution relative to the maximum dose increases with the mean energy of the electron beam from 0.6% for the 6 MeV beam up to 6.3% for the 22 MeV beam on Varian Clinac-2300 C/D linear accelerator, extrapolated back to the depth equal to R_p for the given electron beam.

In contrast to the behaviour of photon beams, the spectrum of a clinical electron beam is changing continuously as the beam penetrates into the medium. At the exit window of an electron accelerator the spectrum is essentially monoenergetic. After traveling through the beam collimation system and the air column toward the patient, the mean energy of the beam decreases and the line shape of the spectrum spreads out. As the

beam penetrates into the medium, this effect is even more important and the mean energy $\bar{E}_z$ at a depth z in the medium can be approximately expressed by Harder's equation:[2]

$$\bar{E}_z = \bar{E}_o (1 - z / R_p) \quad , \qquad (1.1)$$

where R_p is the physical range of the electron beam in the medium and $\bar{E}_o$ is the mean electron beam energy at the surface of the medium.

1.1.3 Proton beams

A high energy proton beam produced in a cyclotron (which is a circular particle accelerator) may be used for treatment of lesions requiring a very accurate spatial dose distribution. As shown in Fig. 1.4, the penetration of proton beams into tissue is a characteristic of heavy charged particles, . The surface dose is relatively low and the dose distribution remains flat almost to the depth equal to the range of protons in the absorbing medium. However, toward the end of protons' path in the absorbing material a sharp rise in dose, referred to as Bragg peak, occurs. The Bragg peak is due to the increasing stopping power of protons with the decreasing energy of the proton beam in the absorbing medium. A single Bragg peak (solid curve in Fig. 1.4) is generally too narrow for use in radiotherapy treatment (width of only a few mm at the depth of the 90% dose) but it can be spread to the desired extent by the superposition of many Bragg peaks occurring at varying depths in tissue. This may be accomplished either by placing a bolus absorber with a variable thickness between the exit window of the cyclotron and the patient or by directly modifying the energy of the proton beam. In both cases the mean energy of the proton beam entering the patient decreases and consequently the depth of the Bragg peak in tissue also decreases with the increasing bolus thickness. As the beams with the continuously changing entrance energy are superimposed, the Bragg peak spreads over a larger range of

depths (dashed curve in Fig. 1.4). On the other hand, the surface dose increases with the superposition of several beams and the advantage of low surface dose of the single proton beam is lost, as also shown in Fig. 1.4.

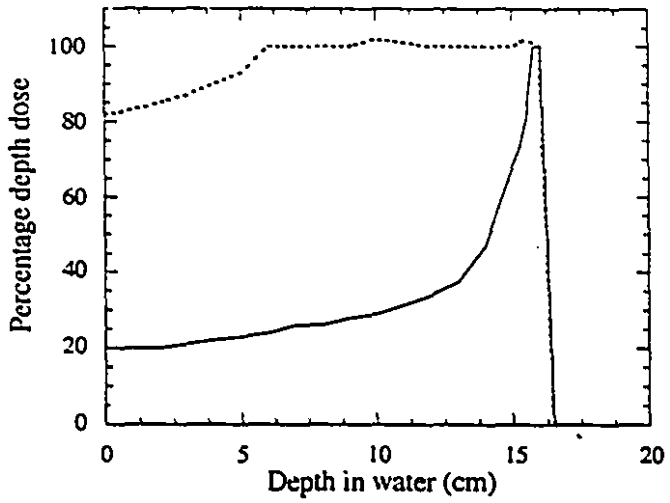

Figure 1.4 The penetration of a 160 MeV proton beam into water. Solid curve represents a single proton beam and typical narrow Bragg peak is seen. Dashed curve represents a spread out proton beam with uniform dose distribution over a broad depth range.[3]

1.1.4 Neutron beams

A nuclear reactor may also be used for radiotherapy as a source of neutrons with various kinetic energies. Neutrons can also be obtained in a cyclotron by bombarding a suitable target with a high energy deuteron beam ($^2H^+$). Neutrons exhibit depth doses similar to those of photons, because they, like photons, have no charge (for example, a 14 MeV neutron beam penetration into tissue is similar to that of a cobalt-60 beam, shown in Fig. 1.2). Their advantage over photons is that they exhibit a lower oxygen enhancement ratio (OER) than photons, and this makes them suitable for treatment of poorly oxygenated tumours. OER is defined as the ratio of the dose required to produce a given biological effect with no oxygen present, to the dose required to produce the same effect in air at standard pressure (101.3 kPa).[4] The presence of oxygen during the irradiation acts as a

sensitizing agent, with biological effects of ionizing radiation larger in the presence of oxygen than in its absence. For the megavoltage photon and electron beams (also known as low linear energy transfer (LET) beams) the OER is approximately equal to 3, while for megavoltage neutron beams the OER is close to 1. In large tumours the blood vessels are often poorly formed leading to regions which are inadequately supplied with oxygen, while the healthy tissue is usually well oxygenated. To minimize the radiation induced damage to healthy tissue, the prescription dose to the tumour volume must be below a certain limit, which may not be sufficient to eradicate all the hypoxic cells when a megavoltage photon or electron beam is used. Because the OER is close to 1 for a neutron beam, the dose response of hypoxic cells and of oxygenated cells is similar, making the neutron beam treatment a better choice for the hypoxic class of tumours. However, because of expensive facilities, treatments with neutron beams are available only in a few specialized radiotherapy centres around the world.

1.1.5 Boron neutron capture therapy

Another promising possibility of using neutron beams is based on the capture of thermal neutrons by boron nuclei ^{10}B, transforming them to ^{11}B nuclei. The cross section for the reaction

$$n + {}^{10}B \rightarrow {}^{11}B + \gamma$$

is very large ($\approx 10^{-21}$ cm^2 for 0.01 eV neutrons) and is proportional to v^{-1}, where v is the velocity of the neutron.[5] The ^{11}B nucleus is unstable and instantaneously decays into two highly densely ionizing particles, one α particle and one ^7Li particle, which have a range of approximately 12 μm in tissue.[6] The potential of this so called boron neutron capture

therapy (BNCT) lies in marking the cancerous cells, particularly of some brain tumours, with compounds containing ^{10}B nuclei, irradiating the tumour volume with a neutron beam, and achieving a spatially localized killing of tumour cells by high LET α particles and ^{7}Li ions. This treatment modality is still in the trial phase, but has already proven its potential for treatment of brain tumours.

1.2 The rationale for the thesis

In the Radiation Oncology Department of the Montreal General Hospital a unique approach to electron arc therapy has been developed in the late 1980s.[7,8] The approach is based on the original concept of a characteristic angle beta. For each patient treated with this technique, a treatment plan is required which accurately shows the dose distributions to be obtained with the proposed treatment approach.

Treatment planning systems which are currently available are not capable of generating dose distributions in patients treated with electron arc therapy, therefore a custom-written software has been developed at the Montreal General Hospital to solve this particular problem. The software depends on a set of measured dose distributions in a tissue equivalent phantom as input. The purpose of this thesis was to measure these dose distributions with a sufficient accuracy for a variety of characteristic angles and for all electron beam energies that are available on the Varian Clinac-18 linear accelerator, which is used for electron arc therapy at the Montreal General Hospital.

Thermoluminescent dosimetry is the most suitable technique for measurements of dose distributions in electron arc therapy, therefore the properties of LiF thermoluminescent dosimeters, relevant to the dosimetry of electron beams, were investigated. The most important issues addressed were the linearity of dosimeters and their relative response per

unit dose to electron beams of various energies. In this research project the relative response of thermoluminescent dosimeters to electron beams of various kinetic energies has been thoroughly examined and a model for its behaviour has been proposed.

1.3 Thesis organization

The thesis is presented with six chapters, with the first chapter providing the background information on radiation therapy in general and radiation beams in particular. Chapter 1 also provides an introduction to the thesis subject.

The second and third chapters describe the apparatus used in the experimental part of the project. In the second chapter an overview of medical electron accelerators (betatrons, linear accelerators, and microtrons) is given, and the radiation sources which have been used in this thesis are described in detail.

Devices used in our experiments to measure dose distributions are described in the third chapter. The first section of the third chapter describes phantoms and phantom materials that have been used in our experiments. A parallel-plate ionization chamber has been used to calibrate thermoluminescent dosimeters and to determine their relative response, so basic properties of ionization chambers and the design of the Markus parallel-plate chamber are discussed in the second section of the third chapter. Thermoluminescent dosimetry is the main experimental method used in this thesis and is thoroughly described in the third section of the Chapter 3.

The fourth chapter describes the relative response of the TLD-100 dosimeters to electron beams with various kinetic energies. Two different methods are used in the investigation of this problem. We proposed a plausible model, which explains the energy

dependence of the TLD-100 relative response, and we validated the model with Monte Carlo simulation.

The fifth chapter describes electron arc therapy as one of the advanced techniques in modern radiotherapy. A few different approaches to electron arc therapy used clinically to date are reviewed and the subsequent discussion is centered on the characteristic angle-β concept developed at McGill University. In the second section of the chapter we discuss the measurement of radial percentage depth dose distributions in phantoms and present results relevant to the clinical aspects of electron arc therapy. Photon contamination of electron arc beams is described in the third section of Chapter 5.

In Chapter 6 a conclusion is presented and some suggestions for the future work relevant to the thesis subject are given.

1.4 References:

1. F.M. Khan, The physics of radiation therapy, 2nd edition, Williams & Wilkins, Maryland, U.S.A. (1994).
2. F.M. Khan, K.P. Doppke, K.R. Hogstrom, G.J. Kutcher, R. Nath, S.C. Prasad, J.A. Purdy, M. Rosenfeld, B.L. Werner, "Clinical electron-beam dosimetry: Report of AAPM Radiation Therapy Committee Task Group No.25", Med. Phys. **18**, 73-109 (1991).
3. J.M. Sisterson, "Clinical use of protons and ion beams from a world-wide perspective", Nucl. Instrum. Meth. **B 10/11**, 1350-1352 (1989).
4. H.E. Johns and J.R. Cunningham, "The Physics of Radiology", 4th edition, Charles C. Thomas, Springfield, Illinois (1984).
5. R.D. Evans, "The atomic nucleus", McGraw-Hill, New York (1958).
6. S.C. Saris, G.R. Solares, D.E. Wazer, G. Cano, S.E. Kerley, M.A. Joyce, L.S. Adelman, O.K. Harling, H. Madoc-Jones, R.G. Zamenhof, "Boron neutron capture therapy for murine malignant gliomas" , Cancer Research **52**, 4672-4677 (1992).
7. M. Pla, E.B. Podgorsak, C.R. Freeman, L. Souhami, J. Guerra, "Physical aspects of the angle-β concept in electron arc therapy", Int. J. Radiat. Oncol. Biol. Phys. **20**, 1331-1339 (1991).
8. M. Pla, E.B. Podgorsak, C. Pla, "The characteristic angle-β concept in electron arc therapy", Radiol. Oncol. **28**, 49-57 (1994).

Chapter 2
Experimental apparatus and radiation sources

2.1 Electron accelerators

High energy electron beams are playing an important role in modern radiation therapy. They were first used in radiotherapy in 1947, but it took quite a long time before they came into routine use in the majority of radiotherapy departments by the late 1970s. Devices for generating electron beams can be divided into three large groups: *betatrons*, *linear accelerators*, and *microtrons*. In this section an overview of electron accelerators with an emphasis on linear electron accelerators is given.

2.1.1 Betatron

The main component of a betatron is a toroid-like evacuated porcelain tube (doughnut) placed between the poles of a specially shaped magnet, which is powered by an alternating voltage.[1] Because the magnetic field is changing sinusoidally with time, it produces a sinusoidally time-varying electric field which accelerates electrons injected into the tube. If the magnetic field strength is correctly chosen, it keeps electrons on circular paths, confined within the doughnut. When electrons reach their maximum energy after a large number of revolutions in the doughnut, they are deflected from the doughnut by an electron "peeler", which is basically a laminated soft iron channel, placed tangentially to the electron equilibrium orbit.[2] Inside the channel there is no magnetic field, thus the electrons' trajectory becomes a straight line leading directly to the exit window in the doughnut and toward the patient. Alternatively, a target may be placed on the path of the electron beam to produce a bremsstrahlung megavoltage X-ray beam.

The main disadvantages of betatrons are their non-isocentric mounting, their low dose rate, and a fairly noisy operation. On the other hand, they are capable of generating electron beams having a wide range of energies and are considerably cheaper than the other two types of electron accelerators used clinically. Nowadays betatrons have become obscure and remain in clinical use only in a few radiotherapy centres around the world.

2.1.2. Linear accelerator

A linear accelerator (linac) is a more complicated device than the betatron, but is considerably more practical for radiotherapy. Therefore linacs have gained a wide-spread use in radiotherapy in the last 20 years. The high energy electron beam from a linac may be used either directly for treatment of superficial lesions or it can be used to produce X rays through a deceleration of the electron beam in a thick target. These X rays have a continuous spectrum of energies (Fig. 2.1), which is cut at the maximum kinetic energy of electrons impinging on the target, and they are well-suited for treatment of deep-seated tumours. Most modern accelerators offer both radiation modalities, with photon beams having one or two (dual energy accelerator) different nominal energies in the range from 6 MV to 25 MV, and electron beams with up to six different energies in the energy range from 5 MeV to 35 MeV.

In a linear accelerator electrons are produced in the electron gun by thermionic emission from a hot tungsten filament and they are injected in discrete pulses into the accelerator waveguide with a kinetic energy of about 50 keV. Inside the waveguide the electrons are accelerated by microwaves produced either in a klystron or magnetron. A power supply provides DC power to the modulator, which produces a few microseconds long high voltage pulses. These pulses are then delivered to the magnetron or klystron and

to the electron gun as well. Microwave bursts generated in the magnetron or klystron are injected into the waveguide, as are the electron pulses from the electron gun. The waveguide itself is an evacuated copper tube with cylindrical resonant cavities, divided by copper diaphragms of different diameter and spacing.

The microwaves used for acceleration of electrons can be either of a traveling or a standing wave type. In the case of traveling waves, a pulse of electrons emitted from the electron gun is injected into the waveguide. The initial velocity of injected electrons is equal to a fraction of the speed of light in vacuum, and then the electrons travel toward the end of the waveguide in phase with the traveling wave. In the waveguide the electrons are continuously gaining energy from the electric field, because the electric field direction is always opposite to the electron velocity vector. When traveling waves are used to accelerate electrons, the end of the waveguide has to be terminated with a "dummy" load to absorb the residual microwave power and to prevent a backward reflection of the radiofrequency waves.

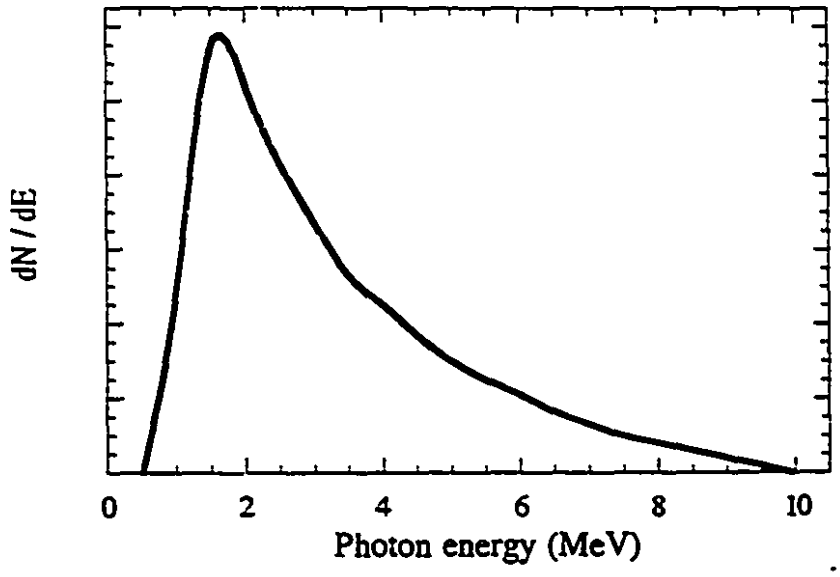

Figure 2.1 A typical energy spectrum of a 10 MV photon beam, obtained by Monte Carlo simulation.

In a standing wave type of a linac, two waves of equal amplitude and frequency travel along the waveguide in opposite directions, adding up to a standing wave. Again, as electrons travel through the waveguide, they experience an accelerating electric field always in the direction opposite to their velocity and they are gaining kinetic energy continuously on their path.

The maximum kinetic energy of electrons in a linac depends primarily on the length of the waveguide. In linear accelerators, used in radiotherapy, this length usually does not exceed 2 m, and the corresponding maximum energy is less than 35 MeV, while the longest linear accelerator in the world is in Stanford, California. Its 3.2 km length provides electrons with 10 GeV kinetic energy, and these electrons are used for research in elementary particle physics.

An electron pencil beam with approximately 3 mm in diameter reaches the end of the accelerating waveguide with its maximum kinetic energy. A beam transport and collimation system, shown schematically for a Clinac-18 linac in Fig. 2.2, brings the beam out of the accelerator and shapes it into a clinically useful beam. After leaving the accelerating waveguide, the electron beam is first bent by a 270° achromatic bending magnet. If the accelerator is used in the photon mode, the beam then impinges onto a copper target and a beam of X rays is produced in the target. The intensity distribution of these X rays has a strong forward peak, but nevertheless a large and heavy primary collimation system is used to limit the photon beam into a narrow cone diverging from the target and to shield against the undesired radiation.

A thin beryllium window separates a vacuum sealed part of the linac containing the bending magnet and the X-ray target from the remaining part of the beam shaping system. Both the transverse and radial profiles of the X ray beam leaving the target are highly non-

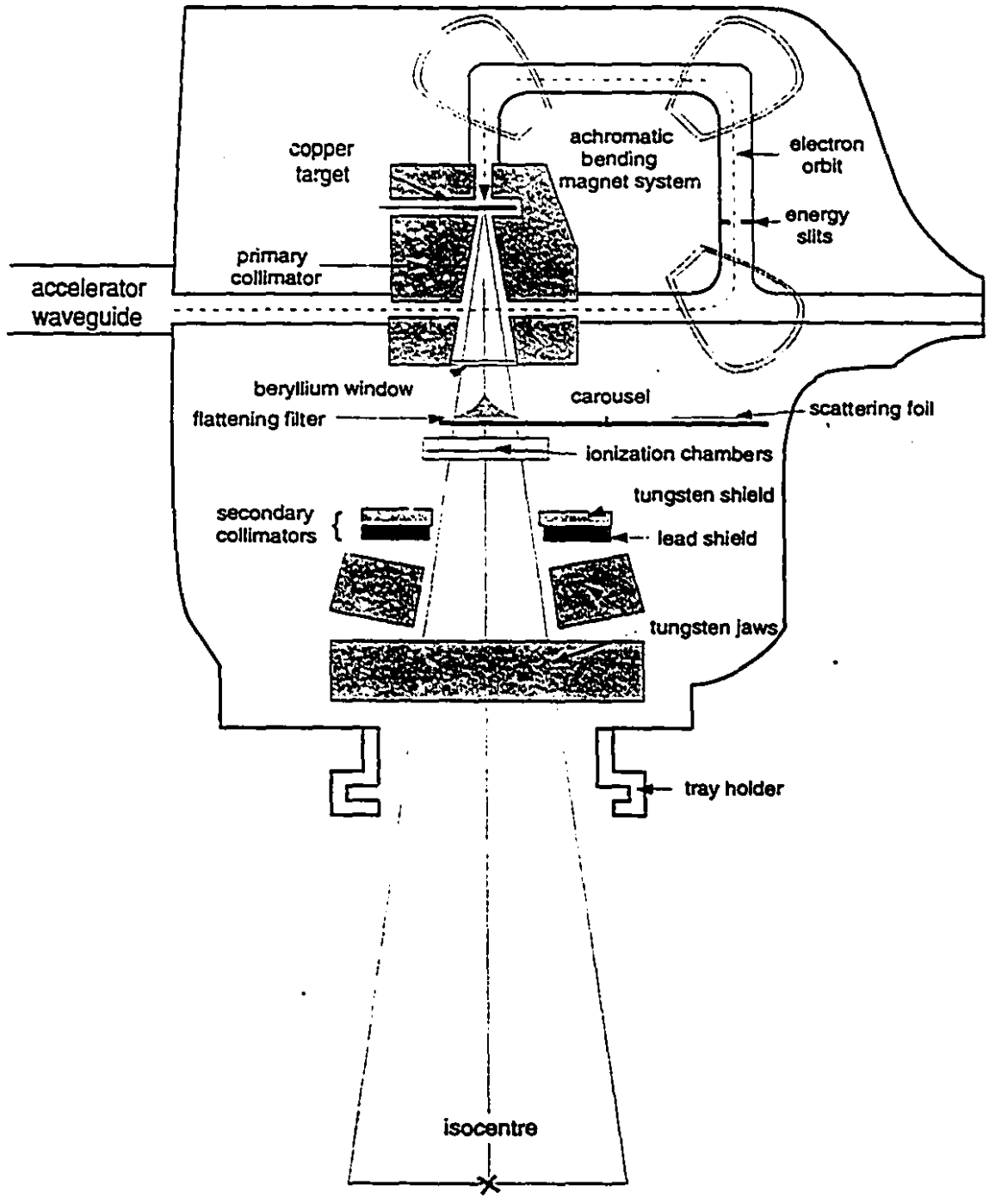

Figure 2.2 Schematic diagram of the Varian Clinac-18 treatment head.

uniform (mainly forward peaked), so a copper flattening filter is used to flatten the beam into a clinically useful beam profile.

The beam then passes through monitor ionization chambers, which measure the output of the linear accelerator, expressed in monitor units (MU). The chambers also monitor the transverse and the radial symmetry of the beam. The radiation beam ionizes the air in the chambers and the integrated ionization current is converted into dose monitor units by a logic circuit. Dual ionization chambers and a beam-on timer are used to ensure patient safety in case of the primary chamber failure. If the primary chamber fails, the secondary chamber will terminate the treatment at a predetermined number of MUs exceeding the number of MUs set on the primary chamber. If both chambers fail, the timer will terminate the exposure.

A secondary collimation system of the beam which defines the maximum square treatment size of the photon beam follows the ionization chambers. To allow smaller square or rectangular treatment fields another collimating system is used. It is located below the secondary collimators and it consists of two pairs of independently movable tungsten jaws, one above the other and placed perpendicularly to one another, one pair for the X-direction and one pair for the Y-direction. The tangential mounting of the jaws reduces the geometric beam penumbra. Usually each pair of jaws is coupled making the radiation field symmetric about the beam axis, however, recently developed linacs allow independent movement of each jaw to define an asymmetric radiation field.

When a linear accelerator is used in an electron mode, the copper target is removed and the pencil electron beam is brought to the collimation system. However, a pencil beam is not useful for clinical applications except in the case of magnetically scanned beams, which scan the desired radiation field in a raster fashion. In standard linacs, however, a

scattering foil, which is placed on a carousel together with the flattening filter used in the photon mode, spreads the electron pencil beam uniformly over a large radiation field. The scattering foil must be thin in order to scatter the electrons over a relatively large treatment field at nominal SSD with a minimal bremsstrahlung production. However, a small fraction of the total electron kinetic energy is still converted into bremsstrahlung and manifests itself as the undesired X-ray contamination of the electron beam.

Electrons from a linac may be applied either as a stationary beam or, using more recent techniques, as a continuous arc beam, where the treatment head rotates around a patient during irradiation. The angle of the travel of the treatment head in a transverse plane of a patient can be smaller than or equal to 360° and corresponding treatment modalities are referred to as electron arc therapy and electron rotational therapy, respectively. The latter modality is used especially for treating the whole skin of a patient (in treatment of mycosis fungoides or Kaposi sarcoma) and in order to obtain the very large radiation fields required an extended SSD technique is used. In the technique developed for this purpose at McGill University the patients rotate around their vertical axes standing on a specially designed platform and the linac treatment head is stationary at 90° instead of the linac rotating around a stationary patient lying on the standard treatment couch.

The intermediate case between a stationary electron beam and an arc electron beam is the so called pseudo-arc beam. It is used to simulate electron arc therapy when a linear accelerator is not capable of emitting electrons simultaneously with the treatment head movement. Instead, a technician rotates the head remotely from the console by small angle steps (5 to 10 degrees) and for each stationary gantry angle an appropriate amount of radiation is delivered, effectively simulating a continuous electron arc therapy.

2.1.3 Microtron

A microtron is the latest development in the line of medical electron accelerators. In a microtron electrons are carried through a microwave cavity which is similar to a section of a waveguide in a linac. Electrons gain kinetic energy inside the cavity and then, after leaving the cavity, they are bent by a magnetic field to move on a circular path to reenter the same accelerating cavity. As the electrons receive higher and higher energies by repeated passes through the cavity, their radii in the magnetic field increase. The cavity voltage, frequency, and magnetic field strength are adjusted so as to keep the electrons entering the cavity always in phase with the accelerating electric field. Electrons travel at almost constant velocity equal to the speed of light, therefore the above condition is equivalent to the pathlength of electron orbits increasing by one microwave wavelength per revolution.

The extraction of the electrons from their orbit is achieved in a similar procedure to that used in betatrons. A narrow steel tube is used to screen the effect of the magnetic field. When the beam energy is selected, the selection tube is moved automatically to the corresponding orbit to extract the beam.

The main advantages of microtrons over linear accelerators are a higher peak energy-to-length ratio, an easy energy selection, and a small energy spread. Their main disadvantage is the relatively high capital and operating costs. In the last decade microtrons with maximum kinetic energies between 35 MeV and 50 MeV have been developed.[3]

2.2 Radiation sources used in the thesis

A Clinac-18 linear accelerator (Varian Associates, Palo Alto, California), installed at the Montreal General Hospital, has been used as the source of ionizing radiation for a vast majority of the experimental work that has been done for this thesis. The linac provides a 10 MV photon beam and 6 MeV, 9 MeV, 12 MeV, 15 MeV, and 18 MeV clinical electron beams. The 6 MeV electron beam is used solely for the rotational total skin electron irradiation and is not available for the standard electron therapy or electron arc therapy.

A Clinac-2300 C/D linear accelerator (Varian Associates, Palo Alto, California), a Theratron-780 cobalt-60 unit (AECL, Ottawa, Ontario), and a SIA-20 ophthalmic ^{90}Sr-^{90}Y eye applicator (Amersham, Arlington Heights, Illinois) have been used for the determination of the relative response of thermoluminescent detectors, described in Chapter 4.

A Clinac-2300 C/D is a dual energy linear accelerator providing 6 MV and 18 MV photon beams. Electron beams with energies of 6 MeV, 9 MeV, 12 MeV, 15 MeV, 18 MeV, and 22 MeV, are also available.

SIA-20 ophthalmic ^{90}Sr-^{90}Y eye applicator is a radioactive source used for contact treatment of phterygium, a benign eye disease. The source is in shape of a disc and it is placed in an aluminum container, which shields the full source except for the active surface. The container is fixed onto a holder which allows the source to swing around the holder. A plastic shield protects a therapist against excessive radiation. The ^{90}Sr-^{90}Y source emits electrons with a continuous energy spectrum having an end-point energy of 2.283 MeV and an effective energy of 0.93 MeV. The source used at the Montreal General Hospital

has been calibrated by the National Institute of Standards and Technology (NIST) in Gaithersburg, Maryland, and the average surface doserate in water was 68 cGy/s on June 1, 1994.[4] The half-life of the source is 28.3 years and the doserate was corrected for decay when used in our experiments.

2.3 References:

1. F.M. Khan, The physics of radiation therapy, 2nd edition, Williams & Wilkins, Baltimore, Maryland (1994).
2. H.E. Johns and J.R. Cunningham, "The Physics of Radiology", 4th edition, Charles C. Thomas, Springfield, Illinois (1984).
3. A.Brahme, B.Lind, P.Nafstadius, "Radiotherapeutic computed tomography with scanned photon beams", Int. J. Radiat. Oncol. Biol. Phys. 13, 95-101 (1987).
4. "Report of calibration; $^{90}Sr + ^{90}Y$ Beta-particle Ophthalmic Applicator Amersham Model SIA.20 S/N 1026ML", United States Department of Commerce, National Institute of Standards and Technology, Gaithersburg, Maryland (1994).

Chapter 3
Radiation measuring devices

3.1 Phantom materials

Tissue equivalent materials are used in applied radiation dosimetry to obtain information about dose distributions inside the human body irradiated with ionizing radiation. The major component of human body is water, and therefore water serves as an excellent phantom material. However, hydrostatic pressure may change the air-pressure inside the ionization chamber cavity and in general it is inconvenient to manipulate liquid phantoms. Therefore solid substitutes for water have been used widely and among the criteria for their water-equivalence are physical density, electron density, and effective atomic number similar to those of water. The most popular water-equivalent materials are polystyrene [$(C_8H_8)_n$], white polystyrene [$(C_8H_8)_n$+ TiO_2], Lucite [$(C_5H_8O_2)_n$], and solid water, which is composed of epoxy resin CB 4 (80.48% by weight), calcium carbonate (5.77%), polyethylene (10.0%), and phenolic microspheres (3.75% by weight).[1]

The phantom material that we have been using throughout this thesis is white polystyrene. Its mass density is 1.054 g/cm^3, its electron density relative to water is 1.018, and its effective atomic number is 5.74.[2,3] The material was available in the form of 0.55 mm, 1.6 mm, and 3.2 mm thick 20×20 cm^2 sheets for rectangular phantoms in studies of stationary electron beams, and as 3 cm thick cylinders with a diameter of 30 cm for cylindrical phantoms used in electron arc irradiations.

3.2 Ionization chambers

3.2.1 Theoretical considerations

Ionization chambers are the most common measuring device used in calibration and determination of dose distributions produced by photon and electron beams. Compared to other types of dosimeters they are easy to use and have a high reproducibility. Moreover, the theoretical foundations of ionization chamber dosimetry are generally well understood. Because ionization chambers can measure the absolute dose, they also provide a calibration system for secondary types of dosimetric devices, such as film and thermoluminescent dosimeters.

The main components of ionization chambers are: a cavity which is normally filled with air at room temperature and pressure; a collecting or measuring electrode connected to an external electrometer; and a polarizing or biasing electrode, connected to external power supply. An additional guard electrode has two roles: it provides the ionization chamber with a homogeneous electric field throughout the sensitive volume and it ensures that the electrometer measures no leakage currents.

When an ionization chamber is placed inside a phantom in a radiation field, the impinging radiation collides with orbital electrons of the chamber wall. These secondary electrons then enter the chamber cavity and ionize the air inside the cavity. A voltage difference applied between the collecting and polarizing electrode produces an electric field inside the air cavity. Ion pairs, created inside the sensitive volume of the air cavity, drift toward their corresponding electrodes, depending on the bias polarity. The amount of charge Q, collected on the collecting electrode, is proportional to the ionization in the air

cavity, which in turn is proportional to the dose, absorbed in the phantom at the point of measurement, according to the equation[2]:

$$D_{med} = Q N_{gas} \left(\frac{\bar{L}}{\rho} \right)_{air}^{med} P_{ion} P_{wall} P_{repl} , \qquad (3.1)$$

where the quantities are defined as follows:

D_{med} is the absorbed dose in the phantom at the point of interest;

N_{gas} is the calibration factor for the particular ionization chamber-electrometer measuring system used;

$\left(\frac{\bar{L}}{\rho}\right)_{air}^{med}$ is the ratio of the restricted stopping power of the surrounding medium to that of the air in the cavity, evaluated at the energy of the radiation beam;

P_{ion} is the ion recombination correction factor, equal to the reciprocal value of the charge collection efficiency of the ionization chamber. The charge collection efficiency is defined as the ratio of the charge collected by the collecting electrode, to the total charge produced in the air cavity. P_{ion} for a case of continuous beam as well as for a pulsed beam can be determined using the formulae given by Attix.[4]

P_{wall} is a correction factor that takes the fraction of electrons originating in the chamber wall into account and it equals to 1 for either photon or electron beams when the chamber wall and the phantom are made of the same material. In the case of thin wall of low Z material, P_{wall} for electron beams may be taken 1, even when the chamber wall composition is different from the phantom material.[5]

P_{repl} is a replacement correction, which has two major components: a gradient correction and an electron fluence correction. Gradient corrections are required when an ionization chamber is placed in a non-zero dose gradient. Electron fluence

corrections are required when the electron fluence in the cavity differs from the electron fluence in the medium after the cavity is removed.

Depending on the electrode configurations there are generally two types of ionization chamber geometries: a cylindrical type and a parallel-plate type. The chamber most frequently used for measurements of dose distributions in photon beams is a Farmer thimble chamber with a cylindrical geometry. It may be used also for dosimetry of electron beams with energies above 10 MeV.[6] For measurements of dose distributions in electron beams with energies below 10 MeV a parallel-plate type of ionization chamber is recommended.

3.2.2 Description of the Markus chamber

We have used a Markus parallel-plate end-window type chamber (PTW, Freiburg, Germany), connected to a Keithley model 35617 electrometer (Keithley Instruments Inc., Cleveland, Ohio) for measurements of percentage depth doses of clinical electron beams available at the Montreal General Hospital (see Chapter 4). In Fig. 3.1 a detailed design of the chamber is given.[7] A small sensitive volume (0.05 cm^3) and a very thin entrance window (2.3 mg/cm^2 of graphited polyethylene) are the most important characteristics of the Markus chamber, making the chamber useful for measurements of dose distributions in electron beams with energies down to 100 keV. The separation between the collecting electrode and the polarizing electrode is 2 mm, and the collecting electrode diameter is 5.4 mm. The collecting electrode edge is 0.5 mm away from the side wall leaving space for a 0.2 mm narrow guard ring and a 0.1 mm insulation groove.

For mechanical protection the entrance window is recessed 0.2 mm below the chamber body surface. A canal that runs from the sensitive volume and along the cable,

reaches the atmosphere at the connector and provides thermal equilibrium of the air cavity with the surrounding atmosphere.

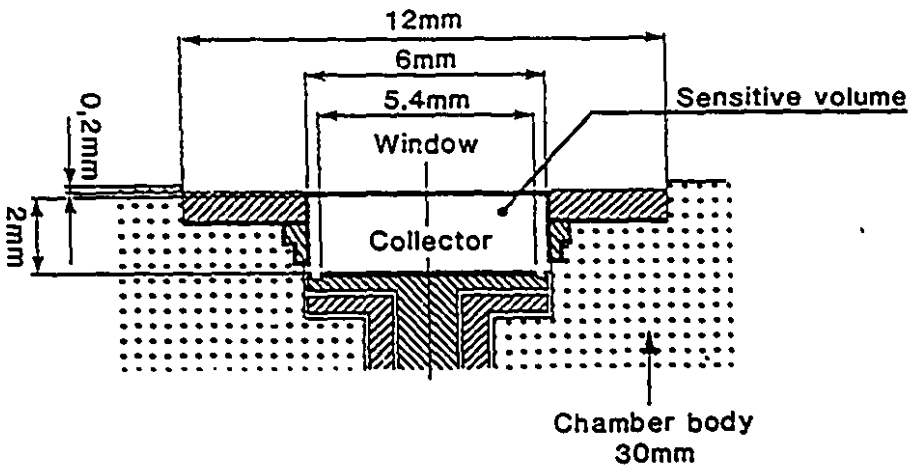

Figure 3.1 Schematic diagram of the Markus parallel-plate end-window chamber.[7]

3.3 Thermoluminescent dosimetry (TLD)

3.3.1 Introduction

Among the relative dosimetry techniques, thermoluminescent dosimetry (TLD) has gained the most widespread use because of its relative simplicity, excellent spatial resolution, and the ability for integrating the absorbed dose over extended periods of time without the need for a bias supply. The main use of TLD is in studies of photon and

electron beam dose distributions in phantoms, and occasionally in direct surface or intracavitary dose measurements in patients.

By definition, ionizing radiation absorbed in medium causes ionization, ionizing the matter either directly or indirectly. Energetic charged particles (electrons, protons, alpha particles, ions, charged pions...) cause direct ionization mainly through Coulomb interactions with valence electrons and are losing their kinetic energy continuously on their path through the absorbing material. The ionization of charged particles is characterized by their range in material which depends on their initial energy and the electron density of the absorbing material.

Energetic neutral particles (neutrons, X rays, uv rays, γ rays, neutral pions...) cause ionization indirectly through energetic charged particles they produce in several intermediate processes. These processes are stochastic and therefore neutral particles have no definite range in material; rather, they are characterized by the probability of interacting with the absorbing material. Photoelectric effect, Compton effect, and pair production are the three most probable and most investigated photon interactions with matter, yielding one or more charged particles (electrons and positrons) which interact through Coulomb interactions with orbital electrons of the medium. Neutrons interact mostly with nuclei, ejecting protons or alpha particles, which subsequently ionize the matter again through Coulomb interactions with orbital electrons. There is a variety of other reactions between neutrons and nuclei, but they are of lesser interest in radiation therapy.

A small fraction of absorbed energy can cause breaking of chemical bonds (e.g., in DNA, in polymers, etc.) and in some special materials a very small part of absorbed energy is stored in the form of metastable energy states. A fraction of this energy can be released later as visible or ultraviolet photons if the material is heated. This phenomenon of

releasing visible or uv photons by thermal means is called *thermoluminescence* (TL). Generally luminescence is the common name for several different effects where visible light is produced. Among other luminescence effects are fluorescence (photon emission happens immediately after its cause), phosphorescence (photon emission is delayed by more than 10^{-8} s), photoluminescence (material is excited by visible photons), electroluminescence (excitation by electric field), bioluminiscence (excitation by biochemical processes), and triboluminiscence (excitation by mechanical friction).[8]

Thermoluminescence has been observed in nature for centuries whenever certain fluorites or limestones have been heated. The association of luminescence, particularly thermoluminescence, with exposure of a material to the radiations emitted by radioactive salts was observed by the pioneers in radioactivity research (for example, Mme Curie in her doctoral thesis noted the TL property of CaF_2).[8] Since then many different materials exhibiting thermoluminescence have been found, including over 2000 natural minerals as well as some organic compounds.[9] However, only a handful of these materials are commonly used in radiation dosimetry, meeting the practical requirements such as large sensitivity, tissue-equivalence, low rate of signal fading at room temperature, and a wide range of linear response. These materials, sometimes referred to as phosphors, include lithium fluoride (LiF), lithium borate ($Li_2B_4O_7$), beryllium oxide (BeO), magnesium borate (MgB_4O_7), calcium sulphate ($CaSO_4$), calcium fluoride (CaF_2), aluminum oxide (Al_2O_3), and magnesium orthosilicate (Mg_2SiO_4).[9] The first four of these materials have low effective atomic numbers and are thus assumed tissue equivalent.

To exhibit the TL phenomenon, compounds are doped with various activators which characterize the thermoluminescent properties of each material. For example, $Li_2B_4O_7$ when doped with manganese has a relatively low sensitivity to radiation and exhibits an orange light emission. But doped with copper, $Li_2B_4O_7$ emits light in the blue

part of the visible spectrum and appears consequently ten times more radiosensitive, because light detection systems using photomultiplier tubes have their peak responses at the blue end of the visible spectrum.

Generally, thermoluminescent detectors are available in two different forms, either as a solid dosimeter or as loose powder. Handling the TLD powder is quite elaborate and relatively inconvenient, therefore solid TL dosimeters have gained a more widespread use in modern radiotherapy departments in comparison to powder. The solid dosimeters are used mainly as extruded and hot-pressed detectors, and are available in two geometries: a ribbon (also known as a chip) and a micro-rod, both manufactured by compression of the normal ingredients (TL material and dopping impurities) at high temperature and pressure.

The theoretical basis of TL is still poorly understood, however, the principles of TL can be qualitatively described.[10] Thermoluminescence does not exist in a pure material, but in one which contains a small amount of impurities or other crystalline imperfections. As known from solid state physics, in solids energy levels of valence electrons are merged into energy bands, which are separated by energy gaps or forbidden bands. In insulators all the valence electrons are present in the valence band while the conduction band is empty. In conductive materials the valence band is not fully occupied by electrons which are also present in the conduction band (hence the name), where they can move freely within and contribute to the electrical conductivity. The width of the energy gap (E_g) separating the conduction band from the valence band is usually a few eV in magnitude.

The presence of impurities in a crystal creates charge carrier traps, which provide metastable energy levels, because direct transitions from trap levels to the ground level are forbidden. When a thermoluminescent material is irradiated, some valence electrons absorb sufficient amount of energy to be raised to the conduction band. In the valence band a

vacancy is created due to the electron transition to the conduction band. The vacancy (hole) as well as the electron are moving through their respective allowed energy bands until they recombine (most likely) or until they get trapped in their respective traps in the energy gap. Traps form two groups: storage traps and recombination centers. When the activation energy for the hole transition to the valence band $E_{a,v}$ is smaller than the activation energy for the electron transition to the conduction band $E_{a,c}$, the hole trap and electron trap are called a storage trap and a recombination center, respectively [Fig. 3.2 (a)]. The situation is reversed when $E_{a,c}$ is smaller than $E_{a,v}$ [Fig. 3.2 (b)], the hole trap playing the role of the recombination center, while the electron trap is the storage trap.

Charge carriers remain in their respective traps until, through the thermal interaction or some other type of excitation, they receive the required amount of energy to move to the conduction band (electrons) or the valence band (holes). Thermal energy can be provided either intentionally by heating the TL material or just through stochastic thermal interactions with the environment at room temperature. Charge carriers released from storage traps will recombine with opposite charge carriers at recombination centres and the recombination will be followed by an emission of a photon, usually in the visible or ultraviolet part of the spectrum. Typical thermoluminescent emission spectra for various TL materials (phosphors) are shown in Fig. 3.3.

In order to use the TL properties of certain materials for quantitative dosimetry of ionizing radiation, a specific and reproducible pattern of a heating process has to be applied to the dosimeters. Prior to irradiation, the TL dosimeters have to undergo an annealing procedure, in which they are exposed to a very high temperature for a sufficient amount of time to empty all the remaining excited energy levels. The annealing procedure includes a reproducible cooling of dosimeters down to the room temperature. After the annealing procedure the dosimeters are ready for irradiation.

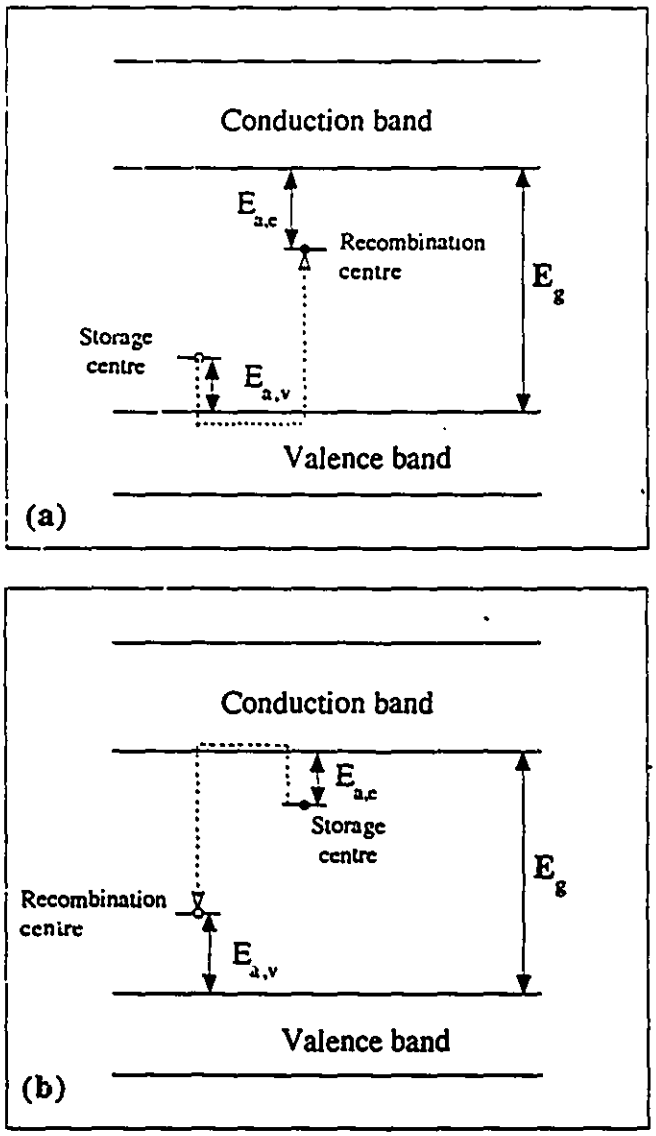

Figure 3.2 A simplified scheme of the thermoluminescent process after irradiation of the TL material. Two opposite processes are possible: (a) The activation energy for the trapped vacancy $E_{a,v}$ is smaller than the activation energy for the trapped electron $E_{a,e}$. The filled vacancy and electron traps are then referred to as storage and recombination centres, respectively. When the vacancy absorbs a sufficient amount of energy (equal or larger than $E_{a,v}$), it travels to the valence band and subsequently recombines with a trapped electron at the recombination centre. (b) The activation energy for the trapped electron $E_{a,e}$ is smaller than the activation energy for the trapped vacancy $E_{a,v}$. The electron and vacancy levels are now referred to as storage and recombination centres, respectively. When the electron absorbs a sufficient amount of energy (equal or larger than $E_{a,e}$), it travels to the conduction band and subsequently recombines with a trapped vacancy at the recombination centre.

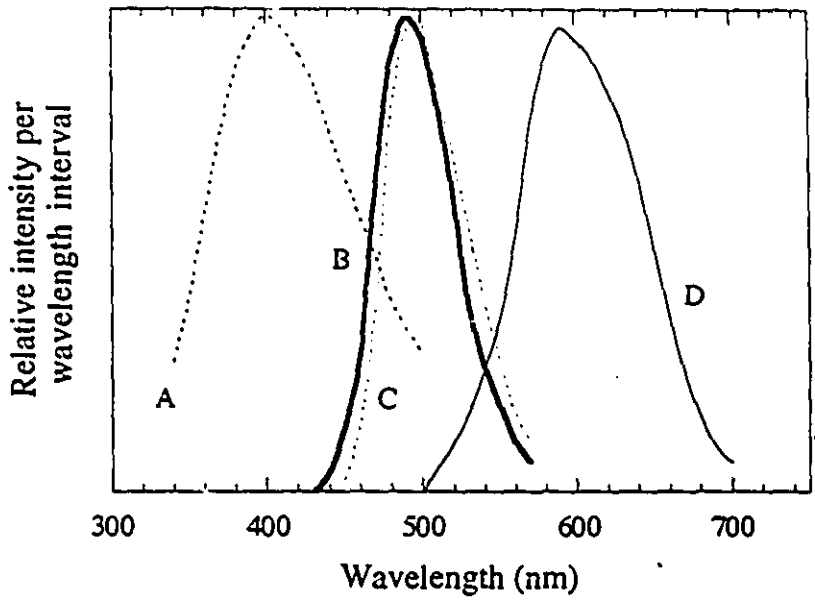

Figure 3.3 Thermoluminescent emission spectra of frequently used phosphors. A: LiF:Mg:Ti (TLD-100); B: CaF_2:Mn ; C: $CaSO_4$:Mn ; D: $Li_2B_4O_7$:Mn .[8]

Approximately half an hour after irradiation, the dosimeters are ready for the read-out, but because of other time constraints usually the read-out takes place the day after irradiation. A dosimeter is placed on the heating planchet of a TLD reader and the light emitted during heating is measured, most commonly with a photomultiplier (PM) tube. To perform a read-out in a reproducible fashion, a heating sequence where the temperature increases linearly with time is normally used. If we record the PM tube current I vs. the planchet temperature T (or time of heating t, since the two are related by a linear relationship), we obtain the so-called *glow curve* or *thermogram* of the TL dosimeter, which usually consists of several distinguishable peaks.

A typical example of a TL thermogram obtained during the heating of a previously irradiated LiF TL dosimeter is shown in Fig. 3.4. The shape of the glow curve and the number of its peaks depend upon the choice of the TL material, temperature at which the material is irradiated, type of radiation, and upon the choice of the applied thermal procedure which consists of the rate of heating and cooling of non-irradiated dosimeters as well as the heating sequence used for the read-out. The absorbed dose is proportional to the area under the glow curve (which is equal to the charge collected on the PM tube anode) or to the height of the particular high-temperature peak, if the parameters determining the shape of the glow curve do not change between calibration and subsequent read-outs. We have chosen the area under the glow curve as a relative measure of absorbed dose, and used a computer algorithm to analyze the glow curve readouts in order to increase the accuracy of the dose measurements with the TL technique.

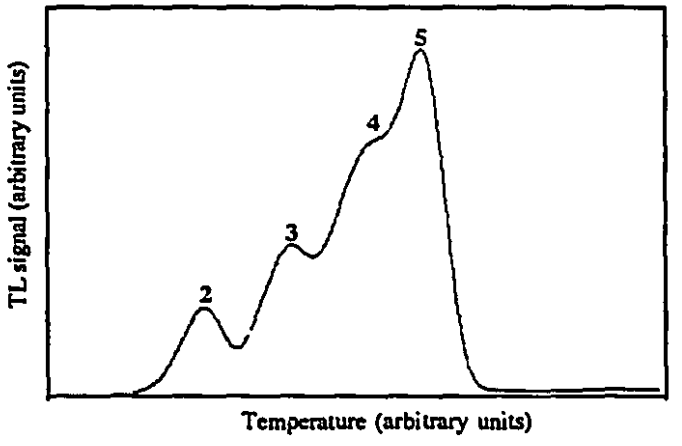

Figure 3.4 A typical glow curve for TLD-100 dosimeter, obtained 1 day after the irradiation of the dosimeter with a strontium-90 electron beam. Dosimetric peaks are labelled according to the standard nomenclature.

After irradiation the electrons in the metastable states will slowly return to the ground level energy states through thermal interaction with surroundings, if the readout of dosimeters is not performed immediately after irradiation. This effect is referred to as

fading of the TL signal. The rate of emptying of metastable states is proportional to $\exp(- \Delta E / kT_S)$, where ΔE is the activation energy of a particular trap, k is the Boltzman constant ($k = 1.38 \times 10^{-23}$ J/K), and T_S is the storage temperature (in °K).

It has been found that exposure of irradiated dosimeters to visible or ultraviolet light also can cause fading of the TL signal.[8] In addition, when non-irradiated dosimeters are exposed to light, this can induce a spurious TL signal and increase the signal background level significantly. To prevent these problems we stored TL dosimeters in a dark drawer after the annealing and prior to as well as after the irradiation. During the readout the artificial illumination of the room was kept at low intensity.

3.3.2 TLD reader and software

A TLD reader is a device in which a TL dosimeter undergoes heating to a high temperature and which collects the emitted light and measures its quantity. A typical reader consists of four main components: a phosphor heating system; a light collection and detection system; a signal measuring system; and a display and recording system.

A well-designed phosphor heating system is a crucial component of a TLD reader. It should provide excellent thermal contact with the heat source, high thermal conductivity, and low thermal capacity to eliminate thermal gradients in the phosphor. In most commercial readers ohmic heating is used for the heating of a TLD planchet (a tray where a dosimeter is placed for read-out) indirectly by bringing it into contact with an electrically heated element. Modern readers can provide user-programmable heating sequences with adjustable heating rates.

The purpose of the light collection and detection system is to collect the light emitted by the phosphor efficiently (and rejecting the undesired infrared thermal glow from the heating planchet) and converting it into an electrical signal, suitable for display and recording. Because the amount of the light emitted from TL dosimeters is very small, the most suitable detector to collect the emitted light is a photomultiplier (PM) tube. PM tubes used in TLD readers usually have 11 or 13 dynode stages with the typical total gain of 10^6. The gain is critically dependent on the number of dynode stages and on the voltage difference between successive pairs of dynodes. To maintain a ± 1% stability in gain, a ± 0.1% stability in voltage is required.[8] The photocathode temperature must also be stable to maintain the gain stability.

The signal-measuring system measures the electric signal which is produced by the PM tube. This signal can be measured and displayed in several ways. .In the pulse counting mode the PM current is converted into a series of fixed-amplitude voltage pulses whose frequency is proportional to the current. The total number of pulses corresponds to the integrated thermoluminescence. In the current measuring mode or charge integration mode the PM current is amplified by a DC amplifier. The third possible method is photon counting where each pulse formed at the PM anode corresponds to a single photoelectric event at the photocathode.

A Harshaw Model 2000 TL analyzer has been used for reading of TL dosimeters in this work. The analyzer consists of two separate components, the Model 2000-A TL detector and the Model 2000-B automatic integrating picoammeter. The system uses a planchet mounted in a sample drawer to heat the phosphor. The temperature of the planchet is increased linearly with time to a preselected value, which has been 250°C in our case. The TL signal is collected and focused onto the photocathode of a PM tube by a lens system. The PM tube is a 2-inch diameter tube with an 11 stage dynode system. The PM

tube converts the optical signal emitted by the TL dosimeter to an electric current which is then integrated between preselected temperatures of the planchet: 120°C and 250°C in our experiments. To collect the whole range of possible signals, the automatic selection of the current range has been used.

The Harshaw TL analyzer is interfaced with a Macintosh II personal computer (Apple, Cuppertino, California). Both the planchet temperature and the PM tube current are digitized by the computer's analog-to-digital converters (ADC). The custom-written program[11] developed for the analysis of TLD-100 dosimeters enables the user to display the glow curve and the temperature ramp of an individual dosimeter read-out in real time. After the read-out, the collected charge has to be entered into the computer via the keyboard. Glow curves can be stored in the computer hard disk memory in order to display and analyze them after the read-out. The two vertical lines that appear on the display are the temperature limits T_1 and T_2 between which the charge is integrated by the analyzer, as shown in Fig. 3.5 (a). The user can first subtract the background portion of the glow curve to separate the true TL signal from the background signal and improve the accuracy of the dose distribution information. This is done by bringing the integration limits to temperatures below the rising part of the first glow curve peak so that they encompass only low-level background, and interactively (by a mouse) choosing the "Subtract background" procedure. This procedure then calculates the mean background signal per temperature interval defined by integration limits, and subtracts it over the whole temperature range. Next, the user can smooth the glow curve by choosing the "Smooth" option.

The subtraction of unstable peaks improves the precision and reproducibility of dose distribution measurements with TL techniques. Any unstable peak A (usually peak 2, because due to standard delay between the irradiation and read-out the peak 1 is not

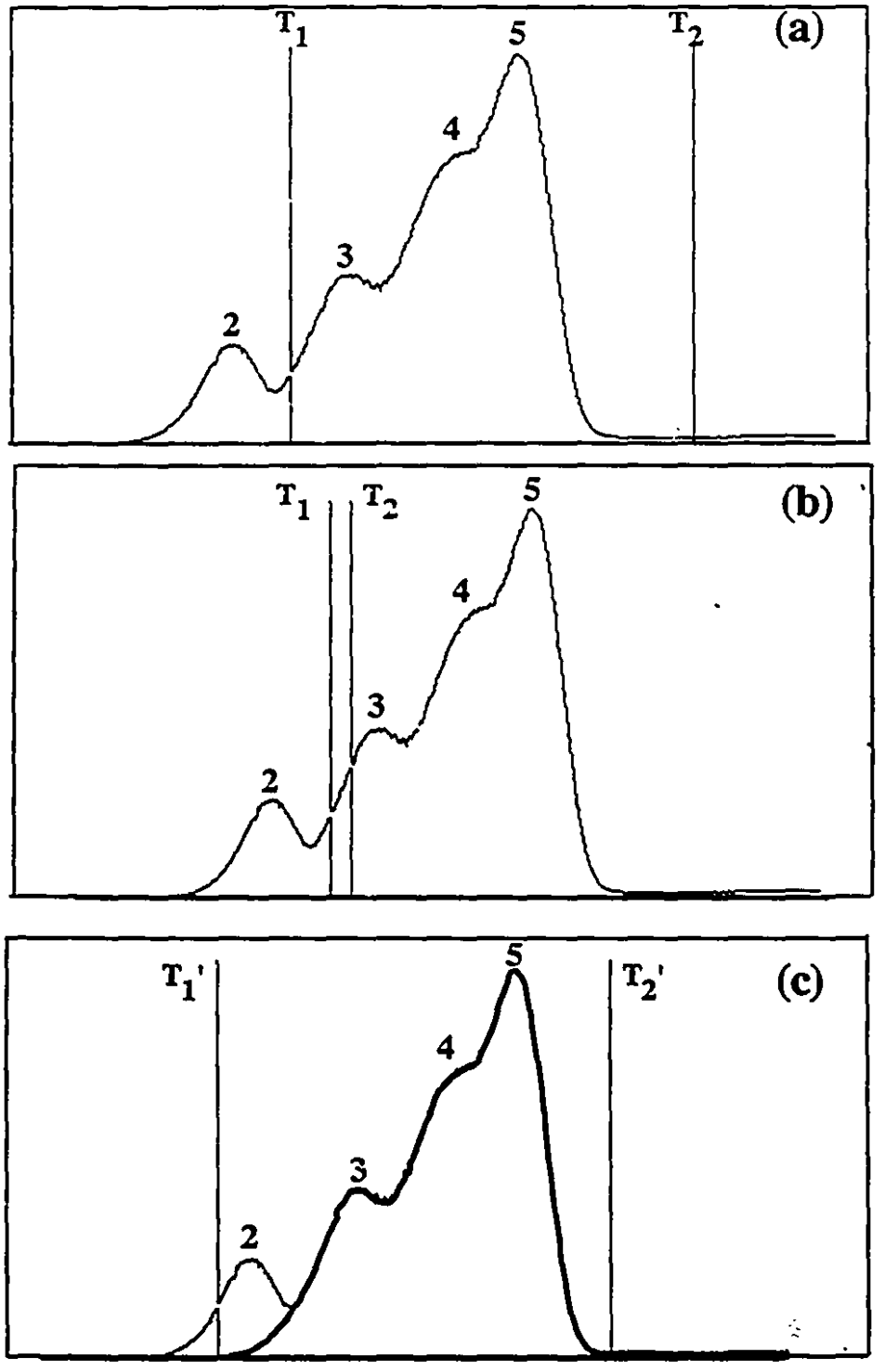

Figure 3.5 The three stages in software subtraction of unstable peak 2 of the TLD-100 glow curve (see text for details): (a) original glow curve; (b) placing of integration limits on the leading edge of peak 3; (c) the leading edge of peak 3 is completely restored and the integration is performed under the whole curve (bold curve).

observed) can be removed by placing the integration limits T_1 and T_2 on the linearly rising portion of the following peak B and choosing the "Fit peak" procedure [Fig. 3.5 (b)]. Two points on the glow curve, $I(T_1)$ and $I(T_2)$, determined by the position of the integration limits, are taken and all the peaks, lying at lower temperatures, are removed as the rising part of the peak B is restored by analytical approximation. For each separate thermogram peak the TL intensity (I) of its leading edge can be approximated by[11]

$$I(T) = k \exp(-a/T), \qquad (3.2)$$

where k and a are the constants and T is the absolute temperature. If the peak separation is large enough to allow the selection of T_1 and T_2 on the leading part of peak B such that there is no contribution to TL intensity from the peak A, Eq.(3.2) can be used to subtract the lower temperature peaks by finding a least-squares fit for a and k and extrapolating the leading edge of peak B intensity to zero, according to Eq. (3.2). The corrected integrated TL signal intensity may be read from the computer screen window after placing the integration limits T_1' and T_2' such that $I(T_1') = 0$ and that $I(T_2')$ reaches the minimum after peak 5.

In this thesis, 1× 1× 6 mm^3 rods and 3×3× 0.4 mm^3 chips of TLD-100 material (Harshaw, Solon, Ohio) have been used. TLD-100 is the most frequently used commercially available phosphor, produced by a homogeneous melting of lithium fluoride, magnesium fluoride, lithium cryolite and lithium titanium fluoride, resulting in a LiF phosphor containing 300 ppm of manganese and 10-20 ppm of titanium.[8] For the TLD-100 material, standard annealing is done for 1 hour at 400°C and optionally for another 24 hours at 80°C.[10] We have used only the high temperature annealing to save time. Annealing has been performed in a Thermolyne 2000 Furnace (Sybron Corporation, Dubuque, Iowa). TLD rods were placed into small glass tubes to prevent sticking of any

impurities to their surface, and the glass tubes were placed into a custom-made aluminum annealing plate with 36 holes to assure good thermal contact. In order to maintain the identity of individual detectors the holes were made in a rectangular grid and identified individually. A big aluminum plate has been used as a heat sink onto which the annealing plate with dosimeters was placed after removal from the oven. The cooling from 400°C to room temperature took approximately half an hour.

Three different glow curves for TLD-100 material (1× 1× 6 mm^3 rods) are shown in Figures 3.6 (a) to (c). The x-axis represents the temperature of the planchet of the TLD reader and the two vertical lines display integration limiting temperatures of 120°C and 250°C. Between these two temperatures, the charge collected from the PM tube is measured and the measured value is entered through a keyboard into a computer. The first glow curve [Fig. 3.6 (a)] has been obtained just a few seconds after irradiation with the strong strontium-90 source, described in Chapter 2, page 21. The irradiation took place very close to the TLD reader, making the delay between the irradiation and the read-out of the dosimeter as short as possible. On this glow curve we are able to distinguish five separate peaks in the temperature range between room temperature and 250°C. The background forms an appreciable portion of the signal and it is attributed to several low-temperature peaks, which are smeared over the low-temperature portion of the glow curve.

The second glow curve [Fig. 3.6 (b)] has been obtained a day after irradiation with the strontium source. This time delay between the irradiation and readout was the procedure for the TLD measurements of dose distributions performed in this thesis. Peak 1 has disappeared completely and the relative height of peak 2 to peak 5 has decreased. The low-temperature background from Fig. 3.6 (a) has also vanished.

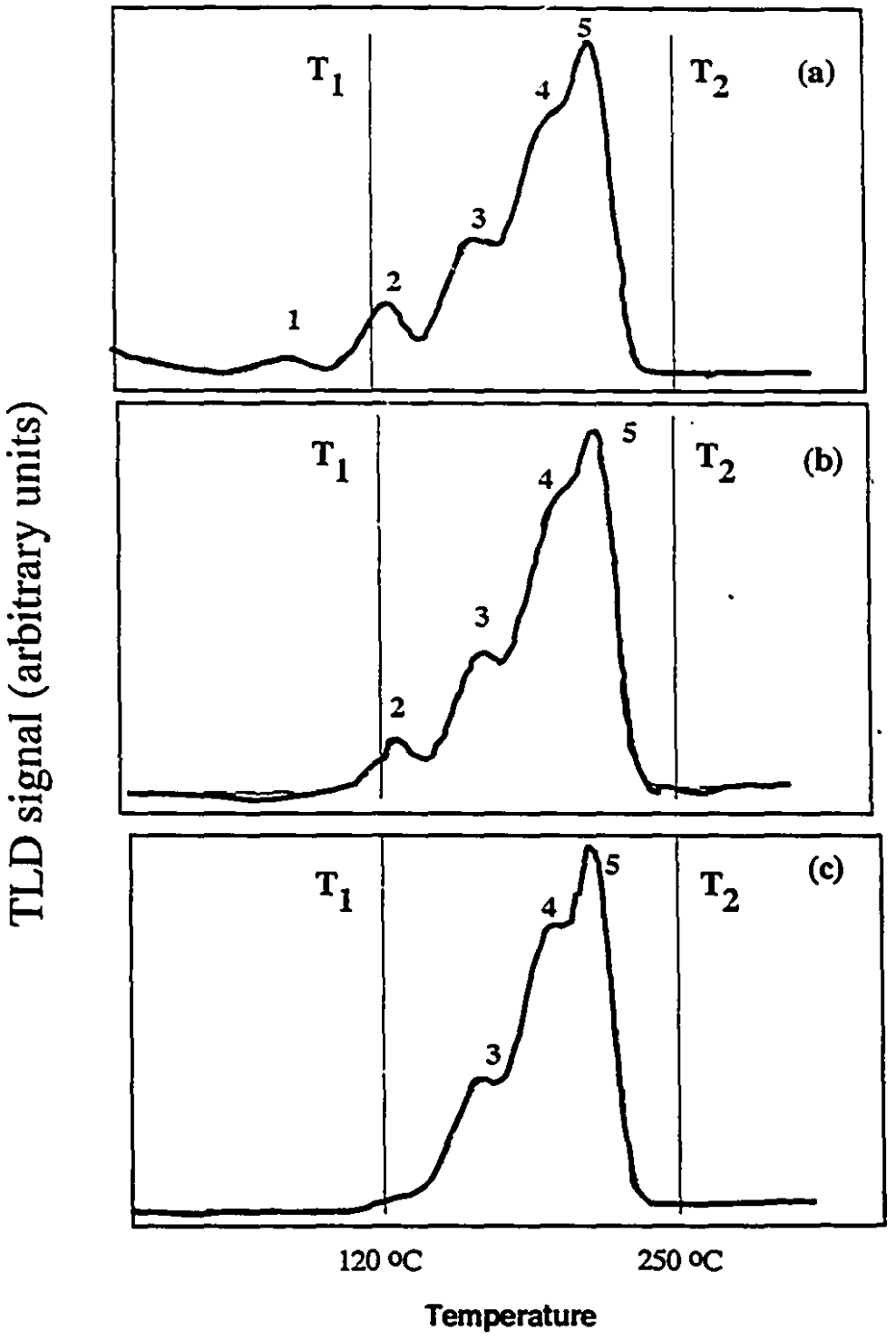

Figure 3.6 Glow curves obtained from TLD-100 micro-rod dosimeters. Vertical lines show temperatures of 120°C and 250°C, between which the TLD reader measures the collected signal. Glow curve has been obtained: (a) one minute, (b) one day, (c) 10 days after irradiation with strontium-90 source. The peaks are labeled as quoted in Table 3.2.

The third glow curve [Fig. 3.6 (c)] has been obtained ten days after irradiation with a strontium source. In this case peak 2 has disappeared completely and peak 3 is less pronounced than it was on the previous two glow curves.

In the literature, peak 6 is also mentioned for TLD-100, and it appears at 285°C.[8] On our three glow curves we cannot see this peak because the planchet temperature during the dosimeter readout rises only to 250°C. The energy stored in this peak is released during the annealing procedure at 400°C. In Table 3.1, we list all glow peaks of TLD-100 with their respective temperatures and half-lives. Peak temperatures also depend on heating rate.

Based on results shown in Fig. 3.6 we can reach the following conclusions. Because peak 1 has a very short half-life, its contribution to the glow curve decays in a few minutes after irradiation and therefore the readout of TL dosimeters should be performed at least half an hour after irradiation in order to get reliable and reproducible results. Peak 2 is also relatively short-lived and usually we want remove it from the glow curve. Various methods to accomplish this are available, one among them is the heating of irradiated dosimeters prior to readout for 10 minutes at 80°C. In this thesis, the above described software method was used instead to subtract the contribution of peak 2 to the total TL signal. Other thermoluminescent glow curve peaks have much longer life-times and are used to obtain the dose information from the glow curve.

Peak No.	temperature (°C)	half-life
1	60	10 min
2	120	1 day
3	170	3 months
4	190	8.5 years
5	210	80 years
6	285	hundreds of years.

Table 3.1 Temperatures and half-lives of glow curve peaks of TLD-100 thermoluminescent material.[8]

3.3.3 Linearity of thermoluminescent dosimeters

The dose response of TL phosphors is linear up to a certain dose and beyond this dose the response curve exhibits a supralinear behaviour. For very high doses the response saturates because there is a limited number of storage traps available in the material. Each TL material has its own characteristic dose response curve, which is determined by kind and amount of impurities in the phosphor on one side and the applied annealing procedure on the other.

Before we started measuring electron dose distributions with TL dosimeters, we determined the extent of the linear portion of the dose response curve for the $1 \times 1 \times 6$ mm^3 TLD-100 micro-rods. For this purpose a series of measurements was performed for each clinical electron beam at the depth of dose maximum in the phantom in the dose range between 10 cGy and 400 cGy. After readout the TL signal vs. dose curve has been plotted

for each electron beam energy and is shown in Figures 3.7 (a) to (d). The point where the linear relationship ceases to hold can be seen clearly. The corresponding dose value is found to be close to 200 cGy for all electron beam energies. After this point the supralinear region begins where the TL signal increases faster than linearly with absorbed dose. Our TLD-100 dosimeters can be used either within their linear range or a proper TL signal vs. dose calibration has to be applied for dose determination. The first alternative is much less demanding and in this thesis the dose delivered to a TL dosimeter never exceeded 200 cGy, except in the experiment for the determination of the limit of linearity range itself.

We also investigated the linearity of the TL response for relatively small electron beam doses. The dose in the polystyrene phantom was determined by an ionization chamber (see Section 3.2) and by the TLD technique. Figure 3.8 shows that the ion chamber dose vs. TLD dose curve does not go through the origin. A small offset of the linear curve by approximately 1.4 cGy has been found. This is attributed to the background signal of the TLD reader, and the dark current of the photomultiplier tube is mainly responsible for this effect. Although the software for the analysis of the thermoluminescent glow curves allows a graphic subtraction of the uniformly distributed background signal, it is currently not capable of a numerical subtraction. However, the magnitude of the error is approximately 1 cGy and in the dose range of 100-150 cGy this error can be neglected. Moreover, at low doses we can account for this effect and subtract the background numerically after the analysis.

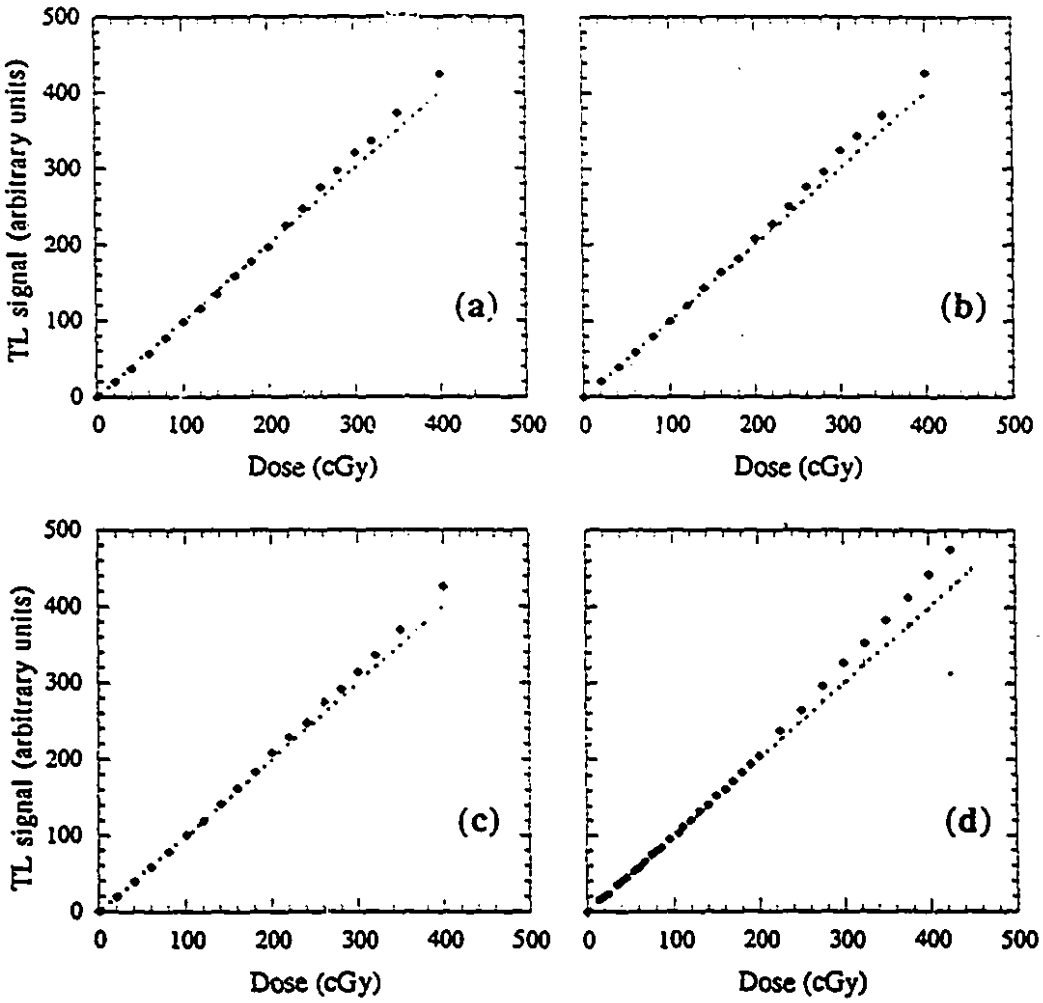

Figure 3.7 Thermoluminescent signal dependence on absorbed dose for (a) 9 MeV, (b) 12 MeV, (c) 15 MeV, and (d) 18 MeV electron beam. For all electron energies the supralinear response of our TL dosimeters begins at approximately 200 cGy.

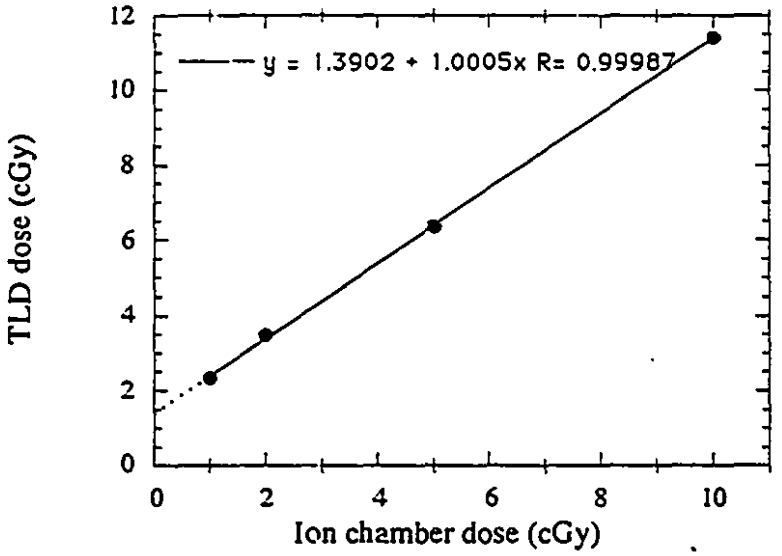

Figure 3.8 Linearity of TLD-100 response for small electron beam doses.

3.3.4 Calibration of thermoluminescent dosimeters

When a batch of TL dosimeters is obtained and intended for use in dosimetry, the dosimeters have to be calibrated individually prior to further use, because, even though they appear identical, their response to the same dose can vary by as much as ±10%, mainly because of slight variations in mass and surface area of individual dosimeters. In this work, 36 TL detectors have been used and following the calibration procedure the whole batch, embedded in a thin polystyrene sheet, was irradiated in a polystyrene phantom with a dose of 100 cGy at the calibration depth. The calibration depth, equal to the depth of dose maximum, was 15 mm for 9 MeV and 12 MeV electron beams, and 10 mm for 15 MeV and 18 MeV electron beams. The field size was 10×10 cm^2 at an SSD of 100 cm. For each energy a separate calibration consisting of 5 identical irradiations was performed.

Another effect similar to signal fading has also been observed. The absolute TL signal per unit dose decreases with the cumulative dose previously absorbed during a lifetime of any individual dosimeter, in addition to the daily fluctuations in the response of any thermoluminescent dosimeter to the unit absorbed dose (also called TL sensitivity). The exact cause of this effect has not been determined, but it might be attributed either to radiation damage (most likely), to handling of the dosimeters, or to repeated heating procedures causing thermal damage. In Fig. 3.9 we show the absolute TL sensitivity dependence on total absorbed dose for six reference dosimeters. It has been obtained by keeping track of total accumulated dose of the reference dosimeters, which have always been given 100 cGy at the reference depth. The average absolute TL signal from the reference dosimeters batch has been monitored for a 6 months period and it has been plotted against the cumulative dose absorbed by the batch. From Fig. 3.9 it can be seen that neglecting the daily fluctuations, the absolute TL signal decreased by more than 20%, with dosimeters having absorbed 140 Gy.

However, the ratio of the TL signals for two dosimeters which always undergo the same thermal procedure (annealing, cooling, and readout cycle) will be proportional to the ratio of their respective absorbed doses, assuming that the doses are within the linear range of dosimeters. Therefore the TLD can be used only as a relative dosimeter, by giving a known dose to the reference dosimeter and comparing its response with the one that was exposed to an unknown dose.

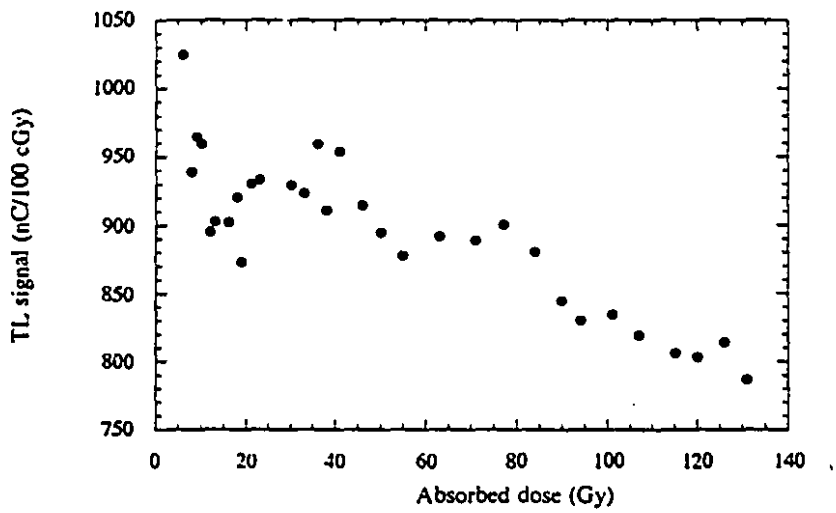

Figure 3.9 Absolute TL sensitivity dependence on cumulative absorbed dose in TLD-100 thermoluminescent dosimeters, averaged for 6 dosimeters.

To increase the accuracy of measurements, a common method is to use several dosimeters as reference dosimeters and to average their response. In this work we used 6 micro-rod dosimeters as the reference dosimeters. To obtain an individual calibration factor for each of the remaining 30 micro-rods which were used as dose detectors, the mean response of six reference dosimeters to the dose of 100 cGy, X_{mean}, was calculated for each calibrating irradiation and then the individual readings of 30 dosimeters X_i ($i = 1, 2, 3, ..., 30$) obtained with the same dose were divided with this number to obtain a calibration factor C_i for individual dosimeters,

$$C_i = X_i / X_{mean} . \qquad (3.3)$$

The whole procedure was repeated five times, and finally the mean calibration factor $\overline{C_i}$ was determined for each dosimeter as the mean value of the five obtained calibrations. Since we obtained 5 different calibration factors, we were able to estimate a standard

deviation of each mean calibration factor $\overline{C}_i$, which was well within 2%, but for most dosimeters the standard deviation was even within 1%.

The same calibration procedure described above has been done for all electron energies available on the Clinac-18 linear accelerator. For different electron energies we expected to obtain identical calibration factors $\overline{C}_i$ within the standard deviation for any particular dosimeter and the results, which are shown in Table 3.2, have substantiated our expectations.

To measure a dose distribution of a particular electron beam with calibrated dosimeters the following procedure was performed: a batch of six reference dosimeters was placed at the depth of dose maximum in a phantom and was irradiated with a known amount of dose D_o, which was usually 100 cGy. Next, the other dosimeters were irradiated at specific measurement points in the phantom. The next step was to read all the dosimeters. After their individual responses Y_i were known, the mean response of the six reference dosimeters Y_{mean} was determined. A dose D_i absorbed by any of the 30 other dosimeter was calculated from the dosimeter response Y_i by the following relationship:

$$D_i = D_o \frac{Y_i}{Y_{mean}\,\overline{C}_i} \quad . \qquad (3.4)$$

When the reference dosimeters are irradiated in one kind of phantom material (medium 1) but measurement is performed in a different kind of phantom or in tissue (medium 2), the measured signal in medium 2 (Y_i) has to be corrected by a stopping power ratio of two media to obtain the dose in medium 2 ($D_{med\,2}$):

$$D_{med\,2} = D_i\, S^{med\,2}_{med\,1} \quad . \qquad (3.5)$$

Dosimeter No.	9 MeV	12 MeV	15 MeV	18 MeV
1	1.018	1.030	1.010	1.004
2	0.954	0.953	0.950	0.949
3	0.971	0.955	0.961	0.952
4	0.959	0.939	0.944	0.927
5	1.054	1.050	1.040	1.035
6	1.024	1.000	1.010	1.022
7	0.963	0.938	0.955	0.951
8	1.005	0.992	0.982	0.985
9	0.967	0.941	0.938	0.927
10	1.066	1.040	1.042	1.042
11	1.028	1.020	1.023	1.023
12	0.915	0.908	0.900	0.900
13	0.992	0.975	0.995	0.990
14	1.030	1.020	1.010	1.012
15	0.980	0.959	0.952	0.960
16	0.971	0.972	0.971	0.958
17	0.996	0.989	0.989	0.985
18	0.964	0.963	0.979	0.956
19	0.960	0.930	0.956	0.942
20	1.016	0.997	1.020	1.014
21	0.992	0.977	0.995	0.972
22	0.999	0.977	0.994	0.980
23	1.091	1.080	1.080	1.068
24	0.991	0.988	0.994	0.997
25	0.962	0.954	0.944	0.949
26	0.964	0.935	0.948	0.940
27	0.967	0.957	0.959	0.961
28	1.032	1.020	1.010	1.005
29	0.784	0.810	0.802	0.852
30	1.053	1.060	1.050	1.055

Table 3.2 Mean calibration factors $\overline{C}_i$ are shown for each dosimeter intended for measurements of electron beam dose distributions in this thesis. They were obtained separately for all energies of clinical electron beams available on Clinac-18 linac.

The stopping power ratio should in principle be calculated at the mean electron energy at the depth of measurement, but it is practically constant for two solid or liquid media over the wide range of energies (400 keV - 30 MeV).

There was no need for this kind of correction in determining the dose by TL dosimeters in this project, since the calibration of TLDs and all our measurements were performed in polystyrene phantoms, thus the stopping power ratio in Eq. (3.5) being equal to 1.

3.4 References:

1. C. Constantinou, F.H. Attix, B.R. Paliwal, "A solid water phantom material for radiotherapy X-ray and γ-ray beam calibrations" , Med. Phys. 9, 436-441 (1982).
2. F.M. Khan, K.P. Doppke, K.R. Hogstrom, G.J. Kutcher, R. Nath, S.C. Prasad, J.A. Purdy, M. Rosenfeld, B.L. Werner, "Clinical electron-beam dosimetry: Report of AAPM Radiation Therapy Committee Task Group No.25", Med. Phys. 18, 73-109 (1991).
3. H.E. Johns and J.R. Cunningham, "The Physics of Radiology", 4th edition, Charles C. Thomas, Springfield, Illinois (1984).
4. F.H. Attix, "Determination of A_{ion} and P_{ion} in the new AAPM Radiotherapy dosimetry protocol" , Med. Phys. 11, 714-716 (1984).
5. Task Group 21, Radiation Therapy Committee, "A protocol for the determination of absorbed dose from high-energy photon and electron beams" , Med. Phys. 10, 741-771 (1983).

6. International Atomic Energy Agency, "Absorbed Dose Determination in Photon and Electron Beams: An Internatonal Code of Practice", Technical report series No. 277, Vienna (1987).

7. S.C. Klevenhagen, "Physics and dosimetry of therapy electron beams", Medical Physics Publishing, Madison, Wisconsin (1993).

8. A.F. McKinlay, "Thermoluminescence Dosimetry" , Medical Physics Handbooks 5, Adam Hilger Ltd, Bristol, UK (1981).

9. The Hospital Physicists' Association: "Practical aspects of Thermoluminescence Dosimetry", Conference Report Series- 43 (1984).

10. J.R. Cameron, N. Suntharalingam, G.N. Kenney, "Thermoluminescent Dosimetry", The University of Wisconsin Press, Madison, Milwaukee, and London (1968).

11. C. Pla and E.B. Podgorsak, "A computerized TLD system", Med. Phys. **10**, 462-466 (1983).

Chapter 4

The energy response of TLD-100 thermoluminescent dosimeters

4.1 Introduction

The response to beam type and energy is generally more complicated for TLD than film. For film it is accepted that the dose calibration (H&D) curve is independent of beam type and energy (except at very low photon energies), while for TLD the reports on response to beam type and energy vary considerably, with some investigators reporting no energy dependence[1] and others[2] reporting large changes in TLD response with beam type and energy.

The current consensus seems to be that the TLD response per unit dose is energy independent for photon beams (except at very low photon energies) but depends on beam energy for clinical electron beams. For example, Holt et al.[2] reported a TLD response per unit dose of 0.87 or less for low energy electrons (up to 3 MeV) in comparison to that for 25 MeV electrons. Paliwal and Almond[3] stated that the TLD dose response is inherently energy independent but the dosimeter acts as a cavity. This implies that to determine the dose in the TLD material, Burlin cavity theory[4], which accounts for cavity dimensions relative to the range of electrons in the cavity material, should be used. Thus the TLD energy dependence will be more pronounced at low electron energies or with larger thermoluminescent dosimeters.

The use of TLD in electron beam dosimetry is inherently more complicated than its use in photon dosimetry since for each electron beam energy one obtains a different dose-response curve. In addition, as the electron beam penetrates into material it gradually loses

its energy so that with depth in material both the dose and energy vary, making an accurate dose measurement with TLD more difficult.

Here we present results of our study of the dose response of TLD-100 LiF dosimeters to electron beams and show that, despite the considerable energy dependence of the TLD dose response curves, thermoluminescent dosimeters may be used reliably in measurements of electron beam dose distributions. This conclusion is especially important for measurements of dose distributions in electron arc therapy which cannot be determined easily with ionization chambers or film.

4.2 Materials and methods

The relative dose response of the TL dosimeters was determined by comparing the TLD signal with the ionization chamber data. The TLD signal was obtained by averaging the results obtained from a batch of six dosimeters each with its own sensitivity factor determined in a cobalt-60 radiation field (Theratron-780, AECL, Ottawa, Ontario).

The mean energy E_z of the electron beam at depth z in the polystyrene phantom was estimated using Harder's relationship:[5]

$$\bar{E}_z = \bar{E}_o (1 - z/R_p) \quad , \qquad (4.1)$$

where R_p is the measured physical range of the electron beam in the phantom material and $\bar{E}_o$ is the mean electron beam energy at the phantom surface, estimated from the following relationship:[5]

$$\bar{E}_o = k R_{50} \quad . \qquad (4.2)$$

R_{50} is the depth in phantom at which the ionization is 50% of the maximum ionization value and k is a constant equal to 2.40 MeV/cm for polystyrene.[5]

With our access to electron beams in the nominal energy range between 6 MeV and 22 MeV we could easily determine the TLD dose response in this energy range. To obtain lower electron energies we irradiated the TL dosimeters at larger depths in phantom and then used Equations (4.1) and (4.2) to determine the mean electron energy at the point of measurement. However, at large depths in phantom the photon contamination of the electron beam constitutes an appreciable fraction of the total dose, making an accurate determination of the TL dose response to low energy electron beams difficult.

To alleviate the bremsstrahlung problem and to obtain a reliable low energy dose response point we used a strontium ophthalmic applicator providing electrons with an effective energy of 0.9 MeV and a surface dose rate of 68 cGy/s on June 1, 1994 (calibrated at the National Institute for Standards and Technology, Washington, D.C.). The TL dosimeters were irradiated on the polystyrene phantom surface at an applicator-dosimeter distance of 8 cm in order to reduce the dose rate to a more practical level of 41 cGy/min. The dose rate at this distance was determined with an end-window ionization chamber through a comparison of its readings on the applicator surface (collection efficiency: 99%) and at a distance of 8 cm (collection efficiency: 100%). The effective electron energy at the position of the dosimeter did not change significantly by moving the dosimeter to a distance of 8 cm (in air) from the source.

4.3 Results and discussion

In Fig. 4.1 we show the relative responses of the 0.4 mm and 1 mm thick TL dosimeters irradiated at the depth of dose maximum (d_{max}) in the polystyrene phantom with

electrons in the nominal energy range between 6 MeV and 22 MeV. The relative responses of the TL dosimeters are normalized to the response per unit dose measured with cobalt-60 gamma rays. The electron energies at the point of irradiation were determined with Equations (4.1) and (4.2) using the relevant values for parameters R_{50} and R_p given in Table 4.1. The 0.9 MeV points in Fig. 4.1 were obtained by irradiating the TL dosimeters on the polystyrene phantom surface with the strontium ophthalmic applicator.

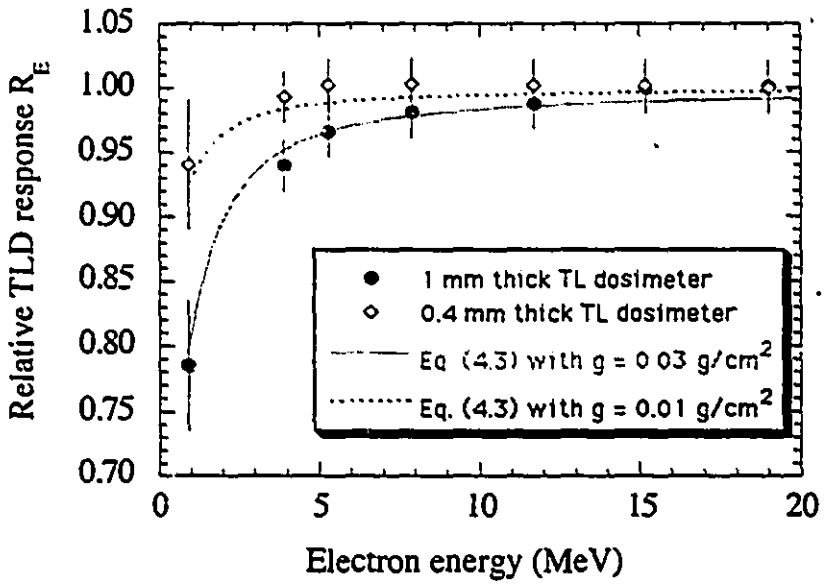

Figure 4.1 The relative TLD response R_E for 1 mm and 0.4 mm thick TL dosimeters measured at d_{max} in polystyrene phantom for various electron beams in the energy range from 1 MeV to 20 MeV. The solid and dotted curves represent a Burlin fit to measured data [Eq.(4.3)]. All data are normalized to $R_E = 1$ for cobalt-60 irradiation.

As shown in Fig. 4.1 and Table 4.1, at high electron energies both dosimeter thicknesses produce a response per unit dose equal to that of the cobalt beam. However, as the electron energy decreases the relative response of the TL dosimeters gradually decreases from the unity value, producing a pronounced drop in sensitivity at an electron energy of 0.9 MeV. The sensitivity drop for the 1 mm thick dosimeters is larger than that

for the 0.4 mm thick dosimeters, giving at 0.9 MeV a relative TLD response of 0.785 for the 1 mm thick dosimeters compared to 0.940 for the 0.4 mm thick dosimeters.

Nominal electron energy (MeV)	R_{50} (cm)	R_p (cm)	$\bar{E}_o$ (MeV)	E_{dmax} (MeV)	R_E (0.4 mm)	R_E (1 mm)	β (cm^2/g)
0.9	0.12	0.60	0.9	0.9	0.94	0.785	15.7
6	2.35	2.90	6.0	3.9	0.993	0.940	3.18
9	3.55	4.25	8.7	5.3	1.003	0.966	2.27
12	4.90	5.90	11.7	7.9	1.003	0.981	1.47
15	6.40	7.60	14.8	11.7	1.002	0.988	0.959
18	7.55	9.20	17.5	15.2	1.002	0.999	0.721
22	9.00	10.9	20.9	19.0	1.000	1.000	0.565

Table 4.1 Parameters of clinical electron beams and TL dosimeters. The 0.9 MeV electrons were obtained with a Sr-Y-90 ophthalmic applicator; 6 MeV and 22 MeV electrons with a 2300 C/D linac; 9, 12, 15, and 18 MeV electrons with a Clinac-18 linac. R_{50} represents the depth in phantom at which the ionization reaches 50% of its maximum value. R_p is the practical range in polystyrene of the electron beam with mean energy $\bar{E}_o$ at the phantom surface and mean energy E_{dmax} at the depth of dose maximum. R_E (0.4 mm) and R_E (1 mm) are the relative TLD responses measured at d_{max} in phantom for 0.4 mm and 1 mm thick dosimeters, respectively, normalized to 1 for the response to cobalt-60 photons. Effective mass attenuation coefficient β is calculated with Eq. (4.5) at d_{max}.

According to the Burlin cavity theory the relative response R_E of the TL dosimeters as a function of electron energy and cavity dimensions is given by the following expression:[3]

$$R_E = \frac{[d\ S_{med}^{cav}]_E}{[d\ S_{med}^{cav} + (1-d)\ (\frac{\mu_{en}}{\rho})_{med}^{cav}]_{Co}} \quad , \tag{4.3}$$

where

$$d = \frac{1 - e^{-\beta g}}{\beta g} \qquad (4.4)$$

S_{med}^{cav} is the stopping power ratio of cavity and medium material, and $\left(\frac{\mu_{en}}{\rho} \right)_{med}^{cav}$ is the ratio of the average photon energy absorption coefficients for the cavity and medium material. In Eq. (4.4) g is the mean path of electrons in the cavity and β represents an effective mass attenuation coefficient for electrons given by a semiempirical relationship[3] as:

$$\beta = 14\rho_o\left(\frac{E_o}{E}\right)^{1.09} \qquad (4.5)$$

with $\rho_o = 1$ g/cm^2, $E_o = 1$ MeV, and E the kinetic energy of the electron.

The solid and dashed curves in Fig. 4.1 represent the relative TLD responses of the 1 mm and 0.4 mm thick dosimeters, respectively, calculated from Equations (4.3) and (4.4). With $g = 0.03$ g/cm^2 for the 1 mm thick dosimeters and $g = 0.01$ g/cm^2 for the 0.4 mm thick dosimeters the agreement between the calculated and measured relative responses is reasonable, suggesting that the TL dosimeters indeed behave as Burlin cavities. However, not all assumptions which underlie the Burlin cavity theory are fulfilled in our study since the electrons penetrate the dosimeter mainly from one direction rather than isotropically. Hence the dosimeter thickness in the beam direction might be a more relevant quantity than a geometrically determined mean pathlength of electrons.

It is evident from Fig. 4.1 that the TLD sensitivity per unit dose depends strongly on electron energy and thickness of dosimeters. This puts the reliability of the TLD technique in determining the electron dose distributions into serious question, since the electron energy strongly depends on the depth in phantom ranging from the maximum

value on the phantom surface to zero at depths equal to practical range R_p of electrons in the phantom material. Therefore the use of TLD sensitivity factors obtained at the depth of dose maximum for larger and smaller depths in phantom is likely to yield erroneous dose distributions, especially at depths close to R_p where the electron energies are very small, resulting in low relative TLD response, as shown in Fig. 4.1.

To investigate this problem we measured percentage depth doses for various electron beams with a parallel plate ionization chamber (Markus, PTW) and with 1 mm thick TL dosimeters. The ionization chamber measurements were done with positive and negative biasing electrode polarities and the dose distributions were determined from the mean ionization data following the TG#25 protocol.[5] The TLD depth dose data were normalized using the relative response obtained at d_{max} for the particular electron beam energy.

A comparison between dose distributions determined with the ionization chamber to those determined with TLD is given in Fig. 4.2. Surprisingly, the agreement between dose distributions measured with the two techniques is excellent (within ±3%) in the whole depth dose range from the surface to R_p. This is true even at depths close to R_p where the electron energies approach zero and the TL sensitivity, as suggested in Fig. 4.1, experiences a significant drop. While at large depths the TLD data were found to be consistently below the ionization chamber data, the difference between the two sets is small and of no clinical significance.

It could be argued that for the portion of the depth dose curve close to the range of electrons two small numbers were compared and the measurement uncertainties could have exceeded 10%. However, this problem was obviated by using a larger irradiation dose at

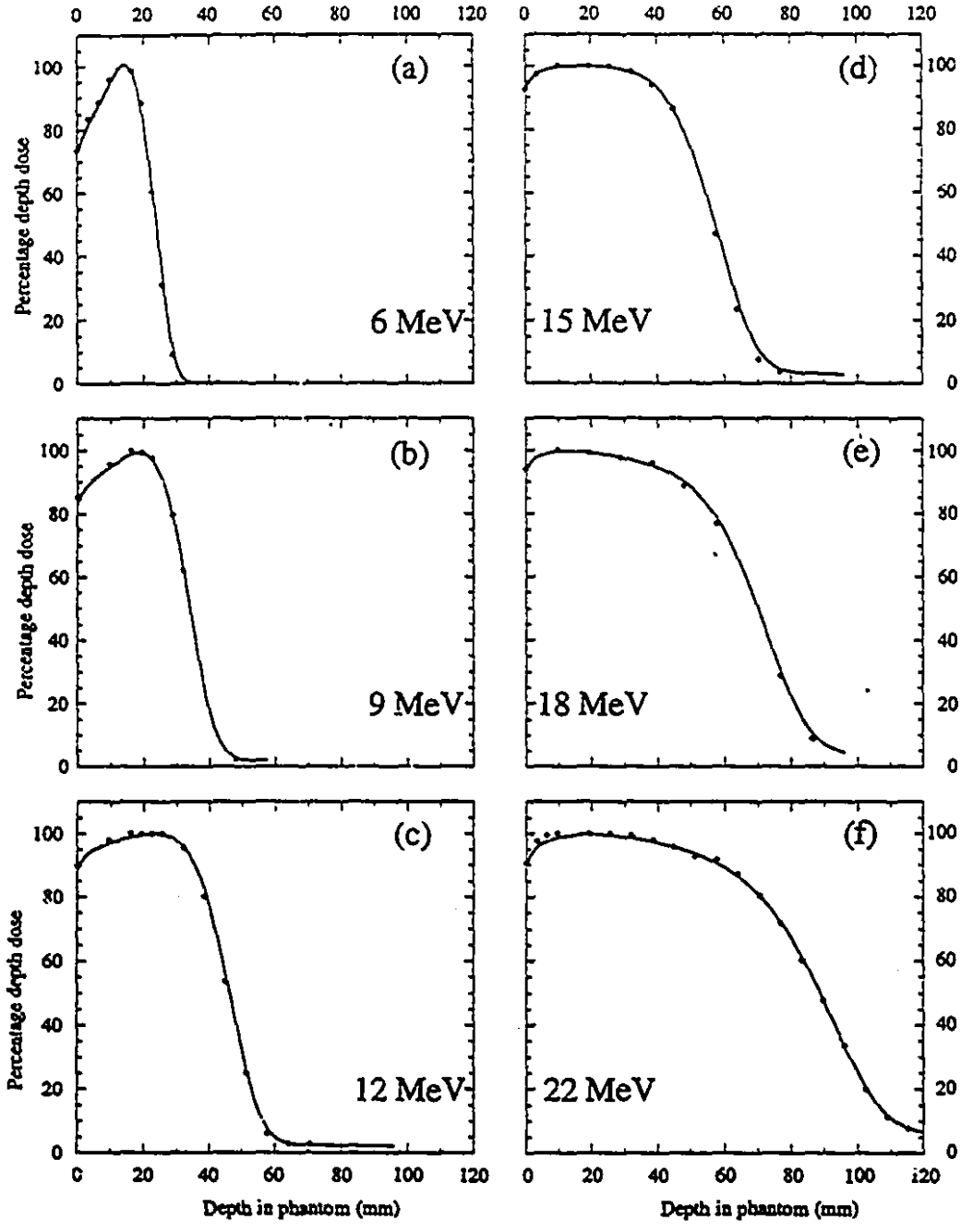

Figure 4.2 Percentage depth doses for various stationary clinical electron beams measured in polystyrene with an ionization chamber (solid curves) and TLD techniques (data points). SSD = 100 cm, field size = 10×10 cm^2.

large depths in phantom to obtain a TLD signal on the order of that obtained at d_{max} thus maintaining the readout uncertainty in the range of ±2%.

Data from Figures 4.2 (b) and 4.2 (e) for electron energies of 9 MeV and 18 MeV, respectively, were then used to supplement the data of Fig. 4.1. The TLD response relative to the cobalt-60 response was determined at various depths in phantom in the range between d_{max} and R_p. As shown in Fig. 4.3, the relative TLD response follows the Burlin curve of Fig. 4.1 for electron energies above 3 MeV. For depths where the mean electron energies are below 3 MeV, however, the relative TLD response starts to increase with decreasing energy and returns to the value of 1 at depths of R_p and beyond. This, of course, one may expect since at depths close to R_p the dose measured by TLD is not only contributed by low energy electrons which exhibit a low relative response R_E but also by a sizeable proportion of megavoltage bremsstrahlung photons with a relative response $R_X = 1$. Figure 4.3 shows that even for high nominal energies of clinical electron beams (18 MeV) the relative TLD sensitivities vary by only 4% between the d_{max} and R_E value of 1 and the 5 MeV value of 0.96. For the 9 MeV nominal energy electron beam the variation between the d_{max} value of 0.96 and the values for R_E and 2 MeV of 1 and 0.93, respectively, is similar amounting to 4% .

To investigate this effect quantitatively we simulated the 9 MeV and 18 MeV clinical electron beams with the Monte Carlo method using the EGS4 code[7], a user written interface, and the PRESTA algorithm.[8] The measured depth doses shown in Fig. 4.2 were calculated with the Monte Carlo technique, and the electron and bremsstrahlung components of the total dose were separated to determine their relative contributions as a function of the depth in phantom. The relative electron dose fractions f_E for the 9 MeV and 18 MeV electron beams are plotted in Fig. 4.4 (a) as a function of the depth in phantom and in Fig. 4.4 (b) as a function of electron kinetic energy which is related to the depth in

phantom through Eq. (4.1). The relative bremsstrahlung dose fraction f_X for electron beams is obviously given as

$$f_X = 1 - f_E \ . \tag{4.6}$$

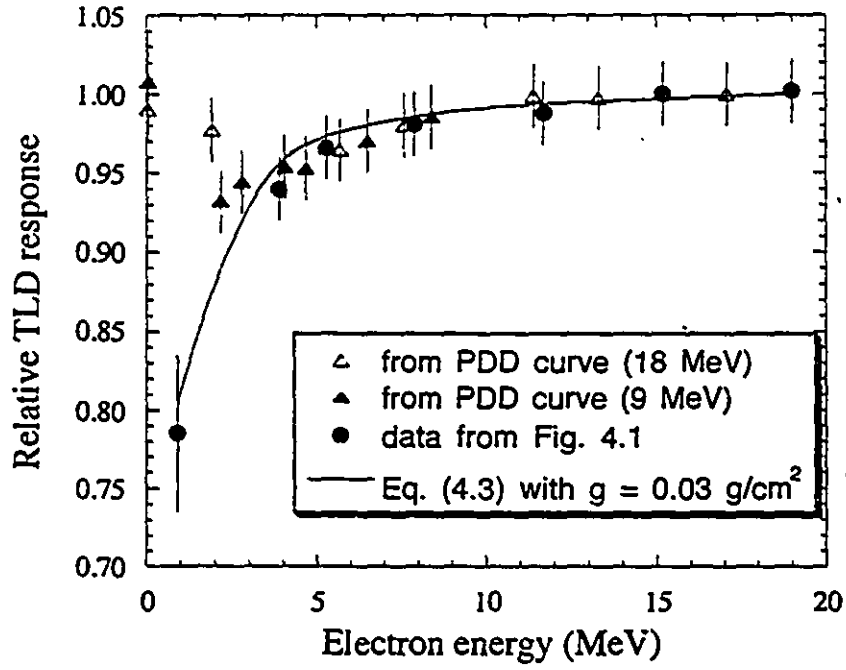

Figure 4.3 Relative TLD response for 1 mm thick TL dosimeter as a function of electron energy. Solid curve and solid circles represent data from Fig. 4.1. Full triangles and open triangles represent data measured at various depths in phantom with energy determined through Eq. (4.1). Full triangles are for the 9 MeV clinical electron beam and open triangles for the 18 MeV clinical electron beam.

The relative TLD response R for a clinical electron beam is thus governed by two components (electron and bremsstrahlung) and may be written as:

$$R = f_E R_E + f_X R_X \ , \tag{4.7}$$

or

$$R = 1 - f_E (1 - R_E) ; \qquad (4.8)$$

incorporating Eq. (4.5) and $R_X = 1$ into Eq. (4.7).

Combining R_E calculated with the Burlin theory (Eq. (4.3) with $g = 0.03$ g/cm^2, Fig. (4.1) and f_E calculated with Monte Carlo techniques (Fig. 4.4), we now use Eq. (4.7) to calculate the relative TLD response for 1 mm thick dosimeters in the dose range between the phantom surface and the practical range R_p. The results are shown with solid curves for the 9 MeV and 18 MeV electron beams in Figures 4.5 (a) and 4.5 (b), respectively. Figure 4.5 also shows the Burlin theory fit (dotted curves) and the relative TLD responses measured at d_{max} (solid circles) from Fig. 4.1. The solid triangles in Fig. 4.5 (a) and the open triangles in Fig. 4.5 (b) represent the relative TLD response measured at various depths in phantom for the two electron beams. The excellent agreement between the measured and calculated R clearly confirms the validity of Eq. (4.7). Furthermore, it suggests that properly calibrated TL dosimeters may be used in dosimetry of clinical electron beams with reasonable confidence despite the dependence of the dosimeter response upon the electron kinetic energy. The mixed electron/photon field at depths close to R_p ensures that the total TLD response remains within a few % of its value attained at megavoltage photon or high energy electron beams in the whole range of electron beam depth doses from the phantom surface to depths far beyond the practical range.

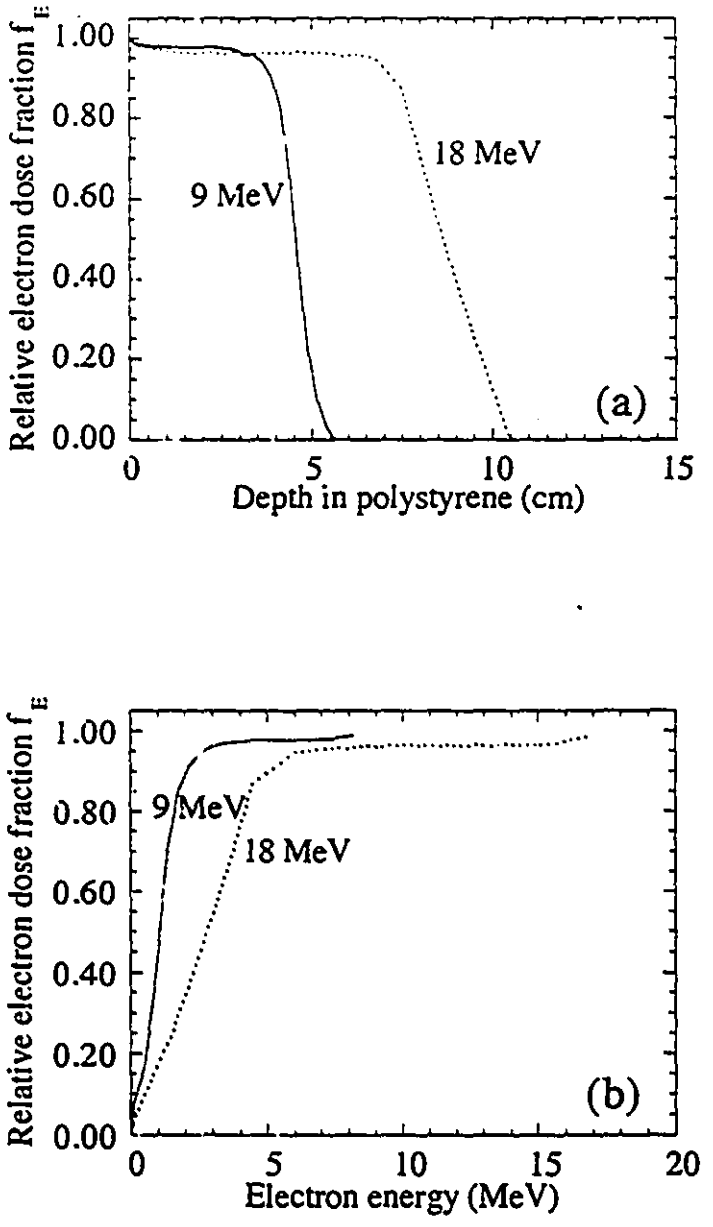

Figure 4.4 Relative electron dose fraction for 9 MeV and 18 MeV clinical electron beams, calculated with Monte Carlo techniques: (a) as a function of depth in polystyrene and (b) as a function of electron energy.

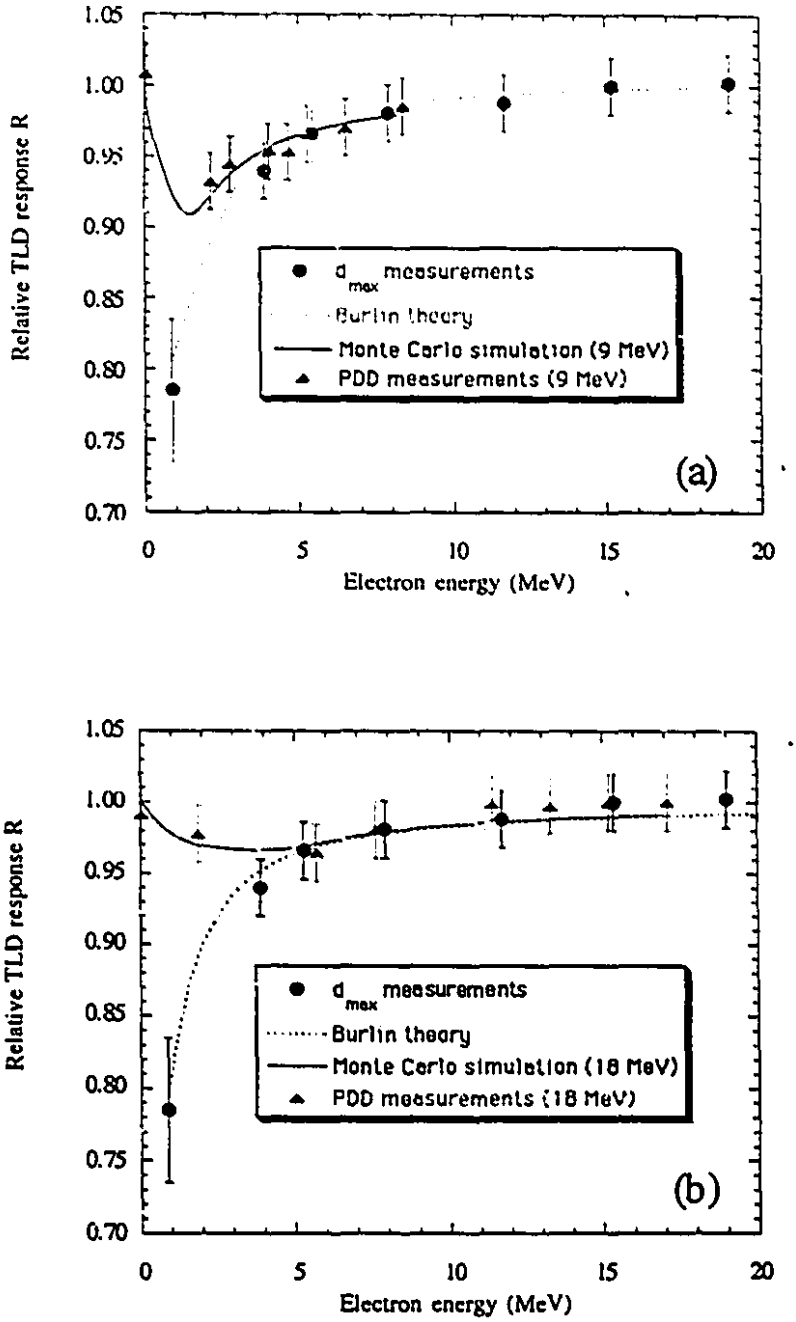

Figure 4.5 Relative TLD response for 1 mm thick TL dosimeters as a function of electron energy: (a) for 9 MeV clinical electron beam and (b) for 18 MeV clinical electron beam. Solid curves: calculated from Eq. (4.6) with Burlin theory and Monte Carlo techniques. Full triangles: measured data at various depths in phantom for 9 MeV clinical electron beam (from Fig. 4.3). Open triangles: measured data at various depths in phantom for 18 MeV clinical electron beam (from Fig. 4.3). Dotted curves: Burlin theory (from Fig. 4.1). Solid circles: measured at d_{max} in phantom (from Fig. 4.1).

4.4 Conclusions

Thermoluminescent dosimeters behave like Burlin cavities and, when used in electron beam dosimetry, their sensitivity relative to that obtained in a cobalt-60 beam depends on electron energy and size of the dosimeter. At electron energies above 15 MeV the TLD response per unit dose is equal to that in cobalt-60 beams; at lower electron energies, however, the response per unit dose decreases with energy, the decrease being more pronounced for thicker dosimeters. For LiF 1× 1× 6 mm^3 rods the relative response to electrons is equal to 0.96 at an electron kinetic energy of 5 MeV and 0.785 at 0.9 MeV.

In measurements of electron dose distributions one can, in the first approximation, make the assumption that the TL dosimeters read the dose directly. The readout may be based on a dose calibration in a cobalt-60 photon beam or in an electron beam at the depth of dose maximum in phantom. The calibration in an electron beam at d_{max} is recommended, especially for low energy electron beams, since it reduces the error associated with neglecting the TLD energy response in comparison with the calibration in a cobalt-60 photon beam. Ignoring the TLD energy response will produce some discrepancy between the measured and the true dose level at depths larger than the depth of dose maximum in the phantom.

At depths approaching the range of electrons in the medium where the electron energy is close to zero one would expect the largest error. However, at these depths the total dose contains a sizeable photon contribution for which the TLD has a relative response of 1. This causes the relative TLD response, which is the sum of the photon and electron contribution, to approach 1 at depths close to and beyond the range of electrons in the medium.

The TLD dose response curve for clinical electron beams exhibits a decrease from unity by at most a few percent with a decreasing energy (i.e., increasing depth in phantom), a minimum for an energy which depends on beam initial energy, and a gradual return to unity for lower electron energies (close to and beyond the range of electrons in the medium) caused by an ever increasing proportional contribution of photons to the total electron beam dose.

4.5 References:

1. N. Suntharalingham and J.R. Cameron, "The response of LiF to high energy electron beams", Ann. N. Y. Acad. Sci. **161**, 77 (1967).
2. J.G. Holt, G.R. Edelstein, T.E. Clark, "Energy Dependence of the Response of Lithium Fluoride TLD Rods in High Energy Electron Fields", Phys. Med. Biol. **20**, 559-570 (1975).
3. B.R. Paliwal and P.R. Almond, "Applications of Cavity Theories for Electrons to LiF Dosemeters", Phys. Med. Biol. **20**, 547-558 (1975).
4. T.E. Burlin, "A general theory of cavity ionization", Br. J. Radiol. **39**, 727-734 (1966).
5. F.M. Khan, K.P. Doppke, K.R. Hogstrom, G.J. Kutcher, R. Nath, S.C. Prasad, J.A. Purdy, M. Rosenfeld, B.L. Werner, "Clinical electron-beam dosimetry: Report of AAPM Radiation Therapy Committee Task Group No.25", Med. Phys. **18**, 73-109 (1991).
6. C. Pla and E.B. Podgorsak, "A computerized TLD system", Med. Phys. **10**, 462-466 (1983).
7. W.R. Nelson, H. Hirayama. D.W.O. Rogers, The EGS4 code system, SLAC report **265** (1985).
8. A.F. Bielajew and D.W.O. Rogers, "PRESTA: the parameter reduced electron-step transport algorithm for electron Monte Carlo transport", Nucl. Instrum. Methods B **18**, 165-181 (1987).

Chapter 5
Electron arc therapy

5.1 Physical aspects of Electron arc therapy

5.1.1 Introduction

For treatments involving large curved surfaces of a patient's body (as post-mastectomy treatment of the chest wall, ribs, skull, or entire limb) a single large electron field is not the treatment of choice, because the oblique incidence of electrons on some parts of the treatment surface and the non-uniform SSD produce a significantly nonhomogeneous dose distribution inside the treatment volume.[1] Intuitively, a better solution is an arc electron beam, composed of many small single electron beams, where the electron beam incidence onto the surface is always close to perpendicular. The isocentre is placed approximately equidistant from the entire treatment surface. However, as simple as this sounds, it is actually difficult to transfer the idea into clinical practice, mainly because of practical difficulties with patient setups and dose distribution calculations. Standard treatment planning systems give poor agreement with measured dose distributions for electron arc treatment.

The treatment using electron arc therapy was first described by Becker and Weitzel[2] in 1956 using electrons of kinetic energy smaller than 15 MeV from a fixed isocentre betatron. Using electrons with a wide range of energies (10 MeV to 43 MeV), also produced by a fixed isocentre betatron, Rassow[3] described small angle pendulum therapy and its different clinical applications. Because the electron arc technique is relatively complicated, only a small number of centres around the world use this treatment modality.

Each center developed its own approach to solving the problems posed by the clinical applications of the electron arc therapy.

Not all isocentric electron accelerators are equipped with an electron arc mode, however, the so-called electron pseudo-arc technique, initially developed by Boyer et al.[4] can be used to simulate the electron arc therapy. In the pseudo arc technique an electron arc is replaced by a series of overlapping stationary electron fields and for each stationary beam the appropriate amount of radiation is delivered. In this technique, the electron field is defined by the x-ray collimator jaws and the electron collimation is achieved on the patient's skin surface with special lead shielding placed directly onto the patient. It has been shown by Bjarngard et al.[5] that an inter-field angle (the increment in gantry angle between the two adjacent stationary electron fields of pseudoarc) should be smaller than 30° to achieve a uniform dose distribution.

Several parameters affect the dose distribution resulting from electron arc therapy. These parameters are: the field width, source-isocentre distance, isocentre depth, electron beam energy, beam collimation (primary, secondary, and tertiary), surface curvature of the patient, and the number of monitor units given per degree for continuous arc or per each stationary beam for pseudoarc. Khan et al.[6] investigated the effects of the field size and isocentre depth on the radial percentage depth doses in order to develop a technique suitable for routine clinical use with 13 MeV electrons. They found that the surface dose decreases and that the depth of dose maximum increases with an increasing depth of isocentre. A similar effect has been found with a decreasing field width. As shown by Ruegsegger et al.[7], the effect can be explained by looking at the time a point spends in the beam as a function of the isocentre depth or SSD. The time increases with the distance from the source, therefore shifting the depth of dose maximum toward the isocentre.

It was found by Blackburn and Moreland[8] that, as the patient contour varied from the patient's superior to inferior thorax, the dose absorbed by the patient was modified by an inverse-square law change with change in SSD. To overcome this problem Leavitt et al.[9] developed an electron arc technique where the X-ray jaws were open to a fixed field of 30×30 cm^2 and a secondary collimator, consisting of two aluminum blocks, was mounted on a tray with the central portion of the tray removed. The blocks could then be opened or closed symmetrically about a central point producing a rectangular or trapezoid shape field to compensate for the change in output intensity caused by SSD changes. Later, this technique was improved[10,11] by implementing a computer-controlled multivane collimator system with 18 independently controlled vanes, providing a variable aperture width along the radiation field.

At McGill University a different approach to electron arc therapy was developed in 1986. The original concept of the characteristic angle beta was introduced and it was shown that the dose distribution for the electron arc treatment with an electron beam of a given energy can be deduced from this single parameter.[12,13] X-ray jaws were used to define the radiation field and the electron collimation was achieved by lead shielding placed on the patient's skin. In comparison to secondary electron collimation placed on the accessory tray, this improved the azimuthal homogeneity of the dose distribution, because the profiles of electron beams defined by X-ray collimators are Gaussian-like and the field junctions do not cause hot or cold spots in dose distributions.

The characteristic angle β is defined geometrically for any point on the surface of a phantom or a patient and its definition can be understood as follows: For the sake of simplicity let us consider a cylindrical phantom placed in the electron arc beam with the linac isocentre inside the cylinder. For a particular point P on the phantom surface, let us look at two beams with the same field size, shown schematically in Fig. 5.1; one beam's

leading edge intersects the phantom at point P, as does the other beam's trailing edge. The characteristic angle β is defined as the angle between the central axes of these two beams. The intuitive meaning of this angle can be explained as the measure of the time during which the point P is "seen" by the moving beam.

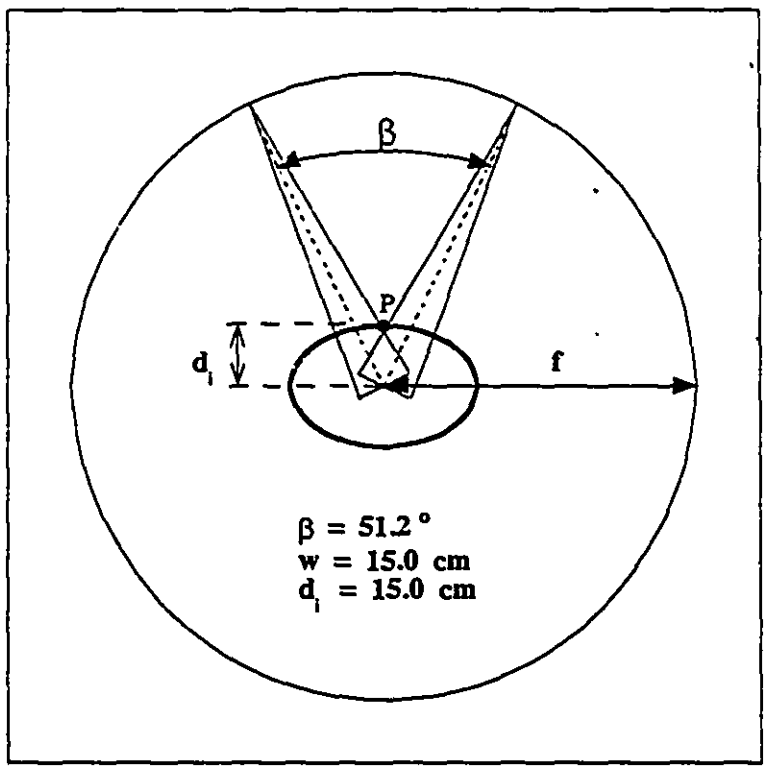

Figure 5.1 The geometric definition of the characteristic angle β: f is the source-axis distance and d_i is the depth of the isocentre; the field width w is defined at the isocentre.

The other relevant quantities in electron arc therapy are the field width w at the isocentre, the virtual source-isocentre distance f, and the depth of isocentre d_i (see Fig. 5.1). The position of the virtual source for a particular electron beam is found by measuring the dose per monitor unit at a constant depth in phantom (output) on the central axis of the beam with changing the source-detector distance. The plot of $(\text{output})^{-1/2}$ versus distance (given by optical distance indicator) will yield a straight line and its intercept with the x-axis will give the position of the virtual electron source with respect to the x-ray source of the linac. For the Clinac-18 linac installed at Montreal General Hospital the virtual source was found to be 85 cm from the isocentre for all electron beam nominal energies.

From a simple geometric consideration the following expression relating w, d_i, and f with β can be derived:[12]

$$w = \frac{2\, d_i \sin(\beta / 2)}{1 - \frac{d_i}{f}\cos(\beta / 2)} \qquad (5.1)$$

From this equation we can express the angle β as the function of w, f, and d_i as follows:

$$\left(\frac{4\, d_i^2}{w^2} - 1\right)\tan^2\left(\frac{\beta}{2}\right) + 4\left(\frac{d_i^2}{fw}\right)\tan\left(\frac{\beta}{2}\right) + \left(\frac{d_i^2}{f^2}\right) = 0. \qquad (5.2)$$

Figure 5.2 shows the dependence of the field width w on β calculated from Eq. (5.1) for different depths d_i of the isocentre and f = 85 cm. In the small angle β approximation the field width increases linearly with β, as follows from Eq. (5.1):

$$w = \frac{f\, d_i}{f - d_i}\beta \qquad (5.3)$$

Pla et al.[12] showed experimentally that, beams with the same nominal energy, but different combinations of w, f, and d_i which yield the same angle β through Eq. (5.2), give the same radial percentage depth dose. Because in practice electron arc treatment angle is much larger than the geometrically defined angle β, the radial PDDs are independent of the treatment arc angle and depend only on beam energy and angle β. It was also shown[13] that from the dose D_A for the reference point A on the surface one can calculate the dose D_Q for an arbitrary point Q on the surface with the following relationship:

$$D_Q = D_A \left[\frac{f - d_i(A)}{f - d_i(Q)}\right]^2 \left(\frac{\beta_Q}{\beta_A}\right) \quad , \qquad (5.4)$$

where β_A and β_Q are the characteristic angles for points A and Q, respectively.

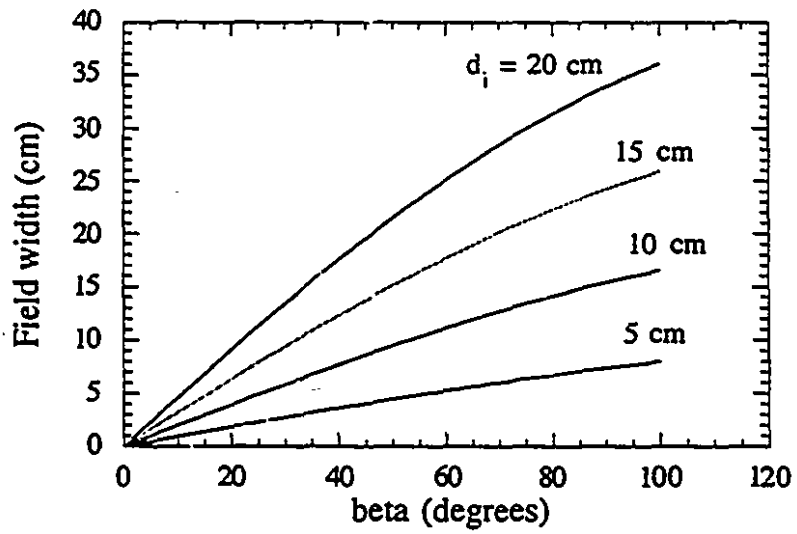

Figure 5.2 The field width w dependence on the angle β with the isocentre depth d_i as parameter. The virtual source-axis distance f = 85 cm.

5.1.2 Clinical application of electron pseudoarc beam

In the Radiation Oncology department of the Montreal General Hospital the majority of the electron arc therapy patients were treated to the chest wall, and a few patients were treated to head and neck sites.

In planning the treatment, first the length of the treatment field and the limits of the arc rotation (angle α) are defined. Computed tomography images are taken in the treatment position to determine the depth of the treatment volume. The isocentre depth (d_i) is chosen by approximating the treatment surface contour to a circle, where the isocentre is placed at the centre of the best-fit circle. The electron beam nominal energy is selected according to the required depth of the treatment, and the characteristic angle β is determined. Next the width w of the electron beam at the isocentre, is calculated with Eq. (5.1). This width is then taken for all stationary beams forming the pseudoarc treatment.

For a given patient set-up even the best choice of the isocentre location cannot prevent large variations in d_i, and a constant number of MU per each stationary beam will result in large variations in the target dose. In these cases the target dose homogeneity is improved by varying the number of monitor units per each stationary beam. The dose at each pseudoarc angular increment is calculated from the following relationship, which is the inverse of Eq. (5.4):[13]

$$MU(Q) = MU(A)\left[\frac{f - d_i(Q)}{f - d_i(A)}\right]^2\left(\frac{\beta_A}{\beta_Q}\right) \qquad (5.4)$$

where MU(A) is the number of monitor units used for the beam at reference point A on patient surface, MU(Q) the number of monitor units calculated for the beam at an arbitrary point Q on the surface.

A Clinac-18 linac is used for the treatment with the pseudoarc technique and most clinical applications have been done with the 9 MeV and 12 MeV electron beams. Secondary collimation (i.e., electron cones) is not used in the McGill technique; the X-ray collimators define the radiation field at the isocentre, and the tertiary collimation is applied by lead shielding placed onto a custom made cast, which is fitted to the patient as shown in Fig. 5.3. The patient set-up is time consuming, while irradiation can be performed relatively fast. In general, the patients tolerate the irradiation well, and the response to treatment is good although in the majority of patients the treatment is palliative since the disease at the time of treatment is very advanced.

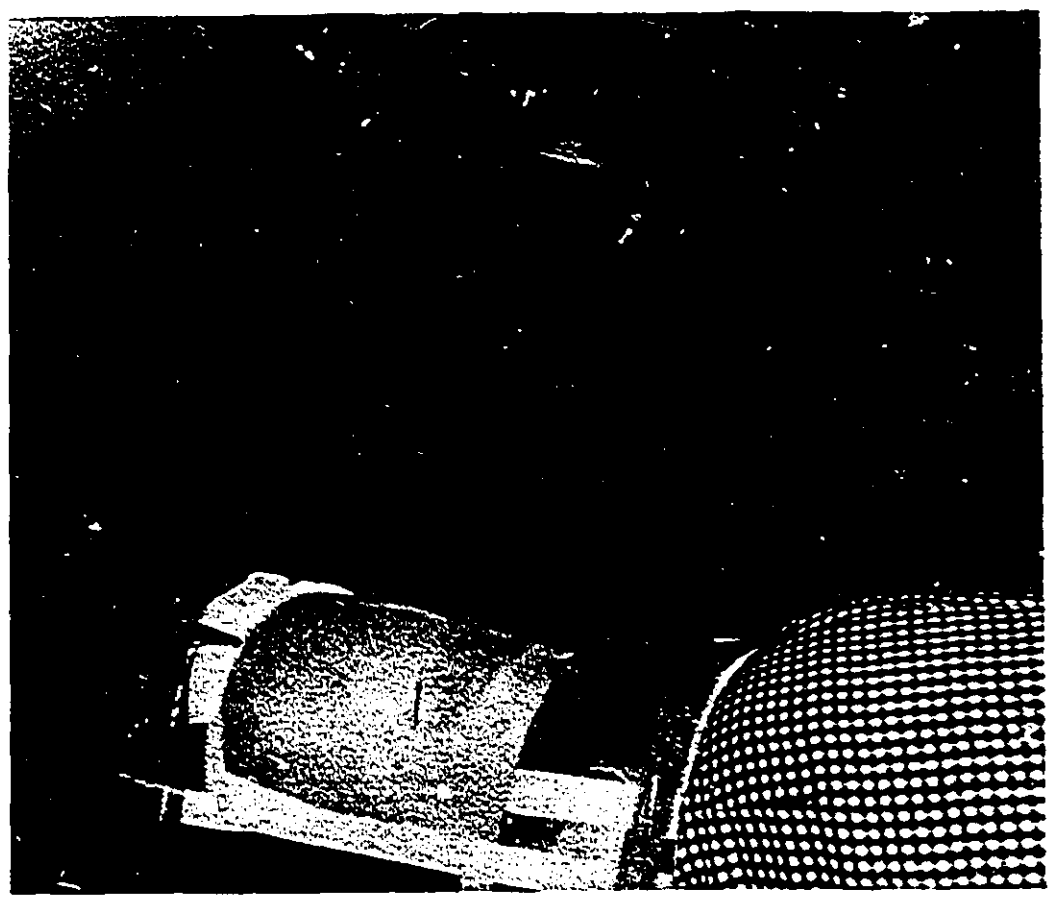

Figure 5.3 A patient set-up for treatment of a large chest wall tumour with the electron arc therapy. The X-ray collimators are used to define the field at the isocentre. The tertiary collimation is applied by placing lead shielding onto a custom made cast which is fitted to the patient. The lead shielding length in the direction of rotation is designed to shield the entire width of the electron arc field.

5.1.3 Calibration of electron arc beam

To use the electron arc modality the output of a linac has to be known. In practice this means knowing the absorbed dose at a particular point in phantom or in tissue assuming the number of monitor units given per degree, when one is using continuous arc modality, or the number of monitor units given per each stationary beam when using pseudoarc modality.

Several different methods for electron arc beam calibration have been developed. In principle, the dose per arc can be determined in two ways, either by integration of the stationary beam profiles or by direct measurement.[14] The first method requires a dose distribution for a stationary beam and the dose calibration as well. The dose at the point is calculated as the sum of contributions from many stationary fields, corrected by inverse square law for the air gap between the treatment surface and the circle of radius r around the isocentre.

The direct measurement of dose per arc requires a cylindrical phantom made of a tissue equivalent material with a hole to accommodate the chamber at the depth of dose maximum. The depth of dose maximum can be calculated from the isodose chart produced for the treatment and will generally be different for different beam parameters, limiting the usefulness of a single phantom. A better solution may be a cylindrical phantom with many little holes for TL dosimeters drilled at different depths. However, TL dosimetry itself is only a relative dose measuring technique, hence the calibration of TLD with the ionization chamber is required to determine the absolute dose, as discussed in Chapters 3 and 4.

Pla et al.[15] investigated the output of an electron pseudo-arc beam, i.e., the dose at the depth of dose maximum per monitor unit given per a given stationary beam. They have

shown that the output increases linearly with the field width w. This conclusion makes sense, because with increasing the field width, a larger number of stationary beams contributes to the dose at the reference point at the depth of dose maximum. However, for different isocentre depths the output is governed by the inverse square law, as found experimentally.[15]

$$\frac{\dot{D}_B}{\dot{D}_A} = \left\{\frac{f - d_i(A)}{f - d_i(B)}\right\}^2 , \qquad (5.4)$$

where $\dot{D}_A$ and $\dot{D}_B$ are the dose rates at d_{max} at points A and B with the isocentre depths $d_i(A)$ and $d_i(B)$, respectively. The inverse-square law relationship between two points at d_{max} holds in general as long as it is applied to various d_i and w combinations which give the same angle β. There is a physical explanation for this since two points with different d_i but the same β will be in the beam for the same amount of time. The dose rate at d_{max} will then depend on the relative distance between the point of interest and the virtual source, and this dependence is governed by the inverse-square law. Then in principle one needs to calibrate the dose rate only for one (d_i, w) combination and then the dose rate for all the other clinically applied combinations can be calculated, using Eq. (5.4).

5.1.4 Treatment planning of electron arc beam

Before a patient is treated with electron arc therapy, a treatment plan has to be calculated by a physicist or dosimetrist and approved by a physician. Current treatment planning systems are not capable of generating the isodose distributions of sufficient accuracy for electron arc treatments, and a few specialized programs have been developed at various radiotherapy centres to fill the void.

A treatment planning model for electron arc irradiation has been proposed by Leavitt et al.[9] They calculated the dose at the point as the sum of stationary fields superimposed in fixed angular increments, extending over the whole arc. Multiple electron energies within the same arc, variable MU per degree, and variable shaped secondary and tertiary collimation have been implemented by this model to optimize the uniformity of the dose distribution across the treatment volume. Hogstrom et al.[16] modified the pencil-beam algorithm for stationary fields to calculate the dose distribution for arc beams to reduce the computation time to acceptable levels. This algorithm considers the total arc as a single broad beam defined by the irradiated surface of the patient. The broad beam is modelled as a collection of strip beams, with each strip characterised by its planar fluence, mean projected angular direction, and a root-mean-square spread about the mean direction. The dose distribution is calculated using these parameters and the pencil-beam theory.

Courteau developed a treatment planning model based on the characteristic angle-β concept.[17] A reference point on the patient surface is defined by the entry point of the beam pointing vertically down (reference beam). A radial percentage depth dose is chosen which gives the angle β for the reference point. The field width w can be calculated using Eq. (5.1) and this width is used throughout the rest of the calculation. Then the angle β can be calculated for all surface points within the arc. The number of MUs for the reference beam can also be calculated. In the next step the number of monitor units for each beam and the dose distribution are calculated. This algorithm differs from the fixed pencil beam technique in that the depth dose curve is the primary parameter, and can be chosen to suit the physician's dose prescription.

5.2 Measurements of radial percentage depth doses

5.2.1 Introduction

The dose distributions in electron arc beams differ from the dose distributions in stationary electron beams. The oblique incidence and collimation of the arc beam are the two major factors affecting the dose distribution. It has been known for stationary electron beams that the surface dose increases and the depth of dose maximum decreases with an increasing angle of incidence (defined to be 0° for perpendicular incidence). Furthermore, because electron arc beams are collimated only by the photon collimators before reaching a patient or a phantom, a significant portion of the electron arc beam has a large angle of incidence.

Since for a given energy the depth doses for electron arc beams with the same angle β are almost identical, one has to measure the dose distributions for a set of beams with various angles β by changing only one parameter in Eq. (5.2). The most convenient method is to fix d_i and to change w. After the depth doses for all clinically relevant situations are known, the appropriate angle β can be calculated and the appropriate dose distribution for a particular angle β obtained.

5.2.2 Materials and methods

As discussed above, for any nominal energy of the electron arc beam the radial percentage depth dose depends only on a geometrically defined angle β. As a part of this thesis, a detailed measurement of radial percentage depth doses for all available energies on Clinac-18 linear accelerator has been performed in a polystyrene cylindrical phantom. The phantom consisted of four 3 cm thick cylinders having 15 cm in radius. The radial PDDs

were measured along a line perpendicular to the contour of the phantom with the TL dosimetry technique described in Chapter 3. A 6 mm thick polystyrene cylindrical slice with holes made for TL dosimeters was sandwiched between two cylinders on each side. Thermoluminescent dosimeters were placed on the phantom surface and at depths of 5, 10, 15, 20, 25, 30, 35, 40, 45, 50, 60, 70, 80, 90, 100, and 150 mm. A special custom-made jig was used to press the phantom slices together in order to avoid air pockets inside. For all radial percentage depth dose measurements, the arc angle α extended over 200° symmetrically with respect to the measurement line, and the isocentre of the linac coincided with the geometric centre of the phantom. The virtual source to axis distance (SAD) was 85 cm and the phantom was aligned with the beam by wall lasers. The field size at the isocentre was determined by the field size indicator. We measured radial percentage depth doses for angles β equal to 5°, 10°, 15°, 20°, 30°, 40°, 50°, 60°, 70°, 80°, 90°, and 100°. The angle β was changed by changing field widths w from 1.6 cm (for β =.5°) to 26 cm (for β = 100°). For each radial percentage-depth dose curve, two sets of data have been measured and the mean value of the two measurements have been calculated.

5.2.3 Results and discussion

The measured radial PDDs of electron arc beams with energies of 9 MeV, 12 MeV, 15 MeV and 18 MeV are shown as families of curves in Figures 5.4 and 5.5. A few general features for all beam energies can be noticed. The surface percentage dose is increasing and the depth of dose maximum is decreasing with increasing β. The range of an electron beam depends mainly on the beam energy and is only slightly sensitive to the angle β. The slope of the radial percentage depth dose beyond the depth of dose maximum is sharper for beams with smaller β, i.e., as β increases, the dose fall-off becomes more gradual.

For a given electron energy and angle β the depth of dose maximum can be determined directly from the measured radial percentage depth doses. However, because the spatial resolution of our measurements has been only 5 mm, we have chosen a method which improves the accuracy of the determination of d_{max}. Three data points are taken into account for each particular beam, one with the highest measured dose and the two neighbouring points. A quadratic parabola is fitted to these three points for each beam and the depth where the parabola has the maximum is determined. We can justify this method because we are looking at the vicinity of maximum and in the first approximation we can fit a quadratic polynomial to any function changing slowly around the maximum. An example of determining d_{max} from the radial PDD curve is shown in Fig. 5.6 for 12 MeV electron arc beam with $\beta = 30^{o}$.

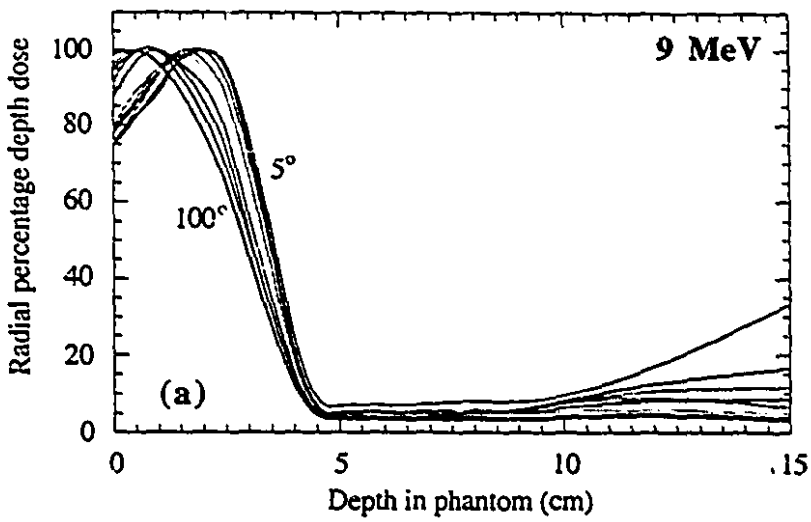

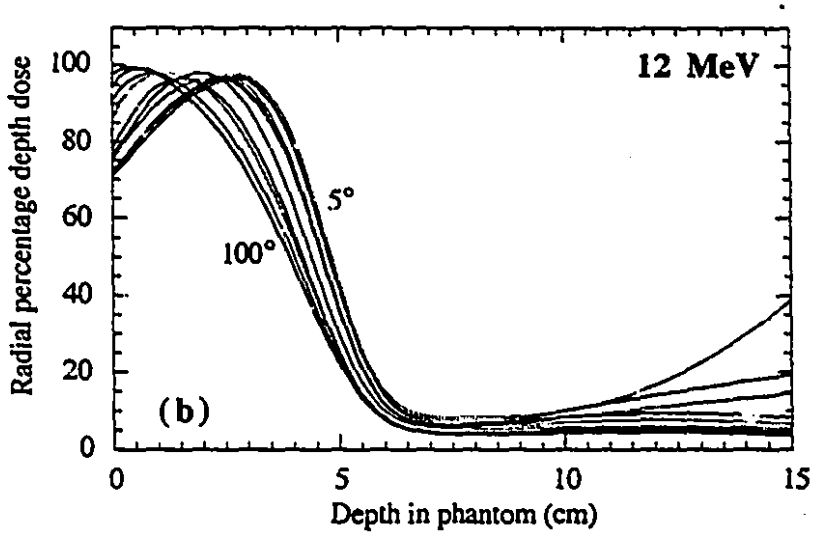

Figure 5.4 Radial percentage depth doses for electron arc beams with various angles β measured in a polystyrene cylindrical phantom with a radius of 15 cm (a) electron energy = 9 MeV and (b) electron energy = 12 MeV. In the angle-β range from 5° to 20° the curves are shown with a 5° increment, and from 20° to 100° with a 10° increment; the isocentre was at the centre of the phantom; d_i = 15 cm.

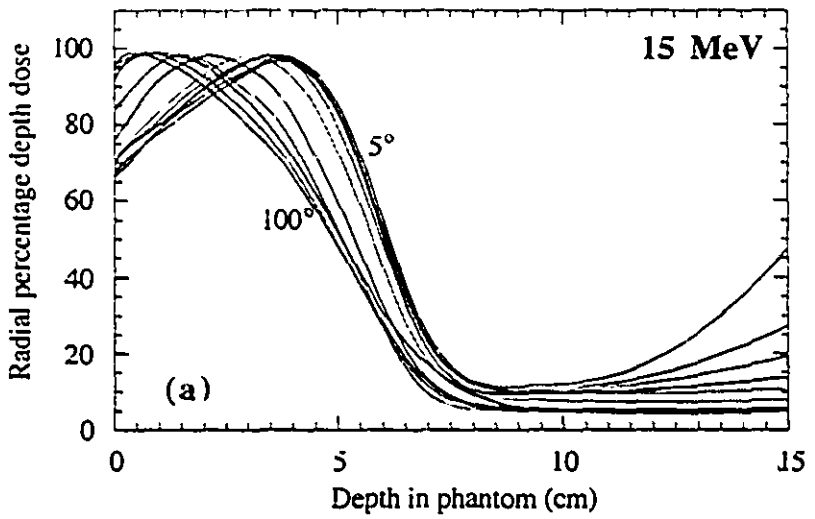

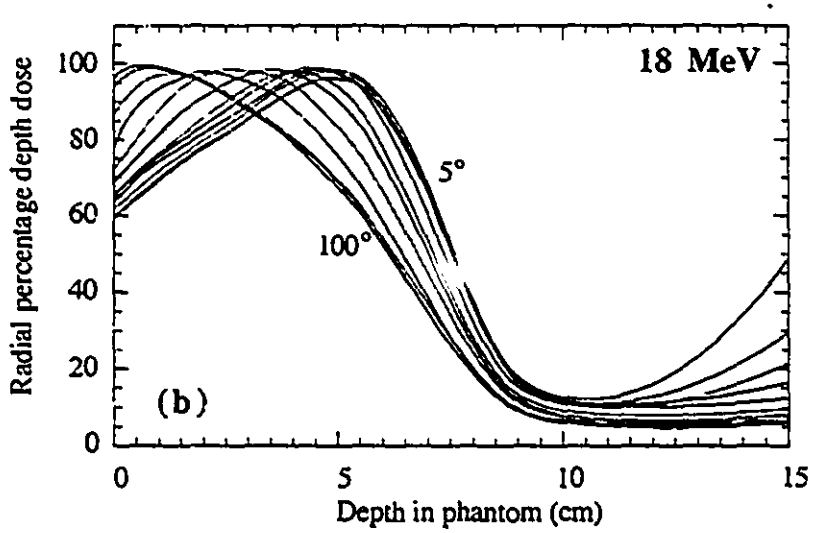

Figure 5.5 Radial percentage depth doses for electron arc beams with various angles β measured in a polystyrene cylindrical phantom with a radius of 15 cm (a) electron energy = 15 MeV and (b) electron energy = 18 MeV. In the angle-β range from 5° to 20° the curves are shown with a 5° increment, and from 20° to 100° with a 10° increment; the isocentre was at the centre of the phantom; d_i = 15 cm.

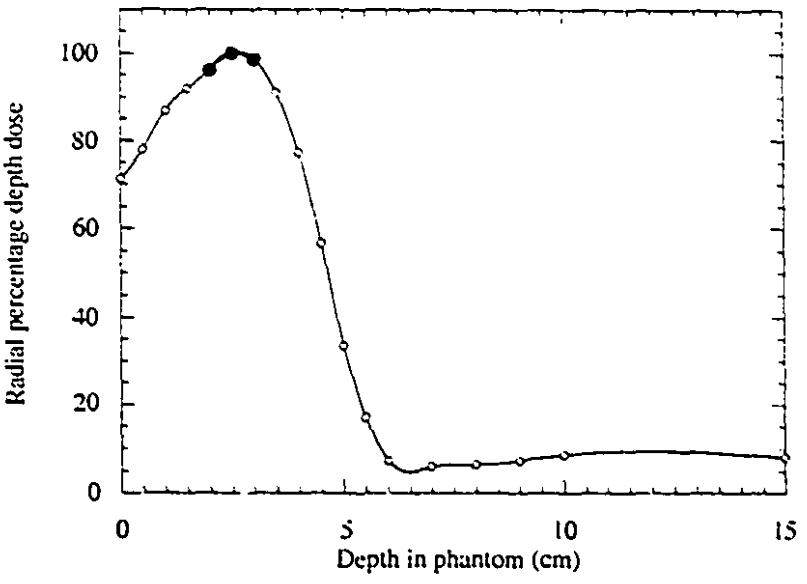

Figure 5.6 An example of accurate d_{max} determination from the radial percentage depth dose curve for 12 MeV arc beam with a β of 30°. Circles represent measured data. Solid circles show the maximum dose point and two adjacent points. A second order polynom is fitted to these three points and its maximum is determined. The abscisa of the maximum gives the depth of dose maximum, 2.6 cm in this example.

Figure 5.7 shows the depths of dose maxima as a function of angle β obtained by this method. Data for the four beam energies suggest a linear dependence of d_{max} on the angle beta, therefore a linear fit is shown for each electron energy. The slope of the d_{max} vs. β relationship is also essentially a linear function of electron beam energy and is plotted in Fig. 5.8 for the data of Fig. 5.7.

In Figures 5.9 and 5.10 we plot the depths of the 85% and 50% depth doses versus the angle β for each beam energy, respectively. The depth of the 85% depth doses has been chosen because it has some clinical significance and is sometimes referred to as the treatment range. Generally, both the depths of the 85% and 50% depth doses are

decreasing with increasing β. While for the depth of the 85% depth doses this dependence is linear for the 9 MeV and 12 MeV electron beams, the deviation from the linear relationship is observed for higher energies, especially for the 18 MeV beam. The 50% depth dose data match a straight line very well for all electron beam energies. The absolute value of the slope of the linear fit is increasing with the beam energy for the depth of the 85% depth dose line and for the depth of the 50% depth dose line.

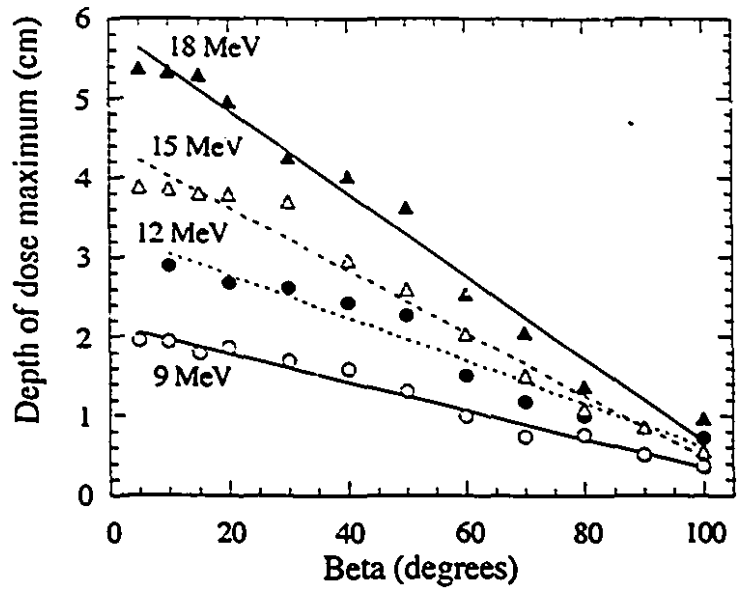

Figure 5.7 Depth of dose maximum dependence on angle beta for electron arc beams of various energies: solid circles: 9 MeV, open circles: 12 MeV, solid triangles: 15 MeV, open triangles: 18 MeV. Linear fit is shown for each electron beam energy.

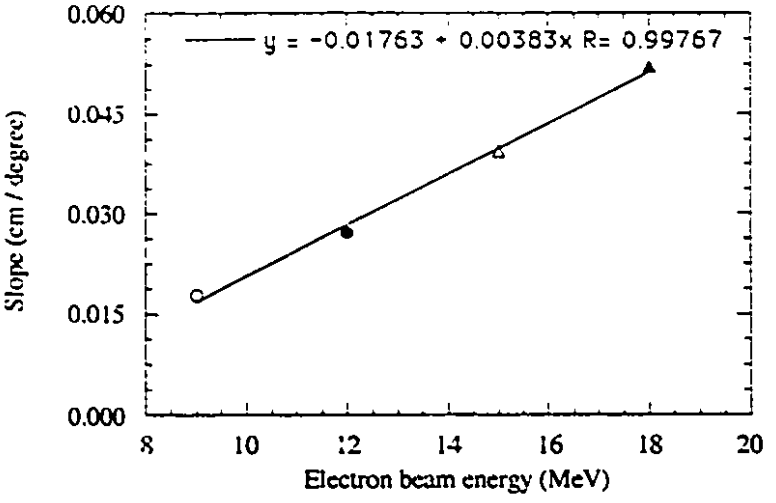

Figure 5.8 The energy dependence of the d_{max} *vs.* β linear relationship slope, shown in Fig. 5.7.

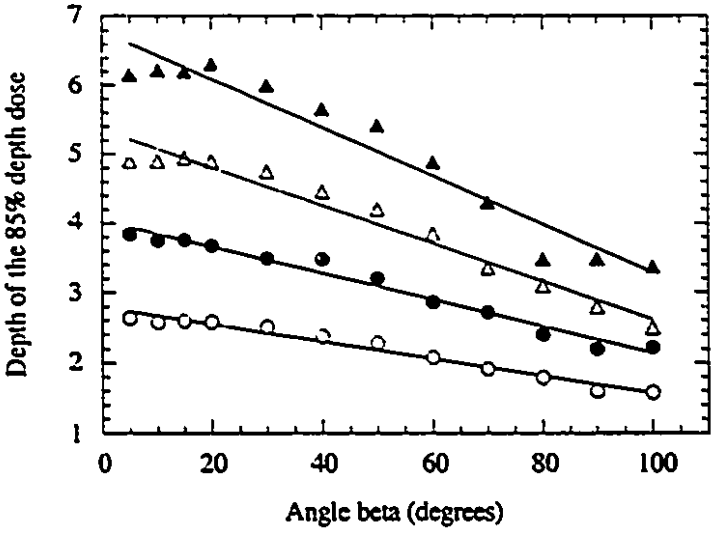

Figure 5.9 The depth of the 85% depth dose dependence on angle β for electron arc beams with various energies. Open circles, solid circles, open triangles, and solid triangles represent data for the 9 MeV, 12 MeV, 15 MeV, and 18 MeV electron beams, respectively. Linear fits are also shown for all the energies.

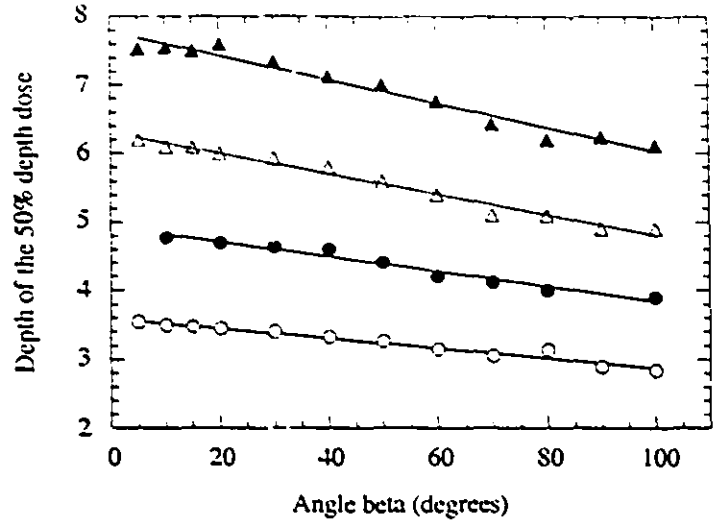

Figure 5.10 The depth of the 50% depth dose dependence on angle β for electron arc beams with various energies. Open circles, solid circles, open triangles, and solid triangles represent data for the 9 MeV, 12 MeV, 15 MeV, and 18 MeV electron beams, respectively. Linear fits are also shown for all the energies.

5.2.4 Dependence of radial depth doses on electron beam energy

Pla et al.[18] proposed the following empirical relationship relating the dose at the depth d for the electron arc beam with nominal energy E to the dose at the depth d_o for the beam with nominal energy E_o :

$$D(d,E) = D(d_o,E_o)\frac{\beta\{d_i - d_{max}(E)\}}{\beta\{d_i - d_{max}(E_o)\}} \quad , \qquad (5.5)$$

where the depth of dose maximum is represented by d_{max} , and the depths d and d_o are related by the equation:

$$d = d_o\frac{R_p(E)}{R_p(E_o)} \quad ; \qquad (5.6)$$

Similarly $d_{max}(E)$ and $d_{max}(E_o)$ are also related by:

$$d_{max}(E) = d_{max}(E_o) \frac{R_p(E)}{R_p(E_o)} \quad ; \tag{5.7}$$

where $R_p(E)$ and $R_p(E_o)$ are the physical ranges of the stationary electron beams with energies E and E_o, respectively. These equations describe simple scaling of depth for beams with different energies.

From the radial percentage depth doses shown in Figures 5.4 and 5.5, we have been able to verify the accuracy of Eq. (5.5). We have taken the data set of radial percentage depth doses for the 9 MeV electron arc beam with angles β ranging from 5° to 100° as our original data set. Using Eq. (5.5) we have calculated the radial depth doses for the 9 MeV electron arc beam from the measured data obtained for the 12 MeV, 15 MeV, and 18 MeV electron arc beams, normalized them to 100% and compared the calculated radial percentage depth doses with the corresponding measured radial percentage depth doses for the 9 MeV beam. The comparison for different angles β is shown in Figures 5.11 (a) to (e).

Equations (5.5) through (5.7) are symmetric and the inverse calculation of the radial percentage depth doses for the 12 MeV, 15 MeV, and 18 MeV electron arc beams from the measured radial percentage depth doses for the 9 MeV beam may also be performed. We have chosen the above alternative to make the figures more illustrative.

The comparison indicates excellent agreement between the calculated and the measured data for all depths beyond d_{max}. In the build-up region, on the other hand, the agreement for large angles β is excellent but deteriorates for small angles β which, as shown in Fig. 5.4, have a larger build-up region. The discrepancy increases with an increase in energy difference $E - E_o$ and is increasing approximately linearly from d_{max} to the surface. To improve the agreement we propose to modify Equations (5.5) through (5.7)

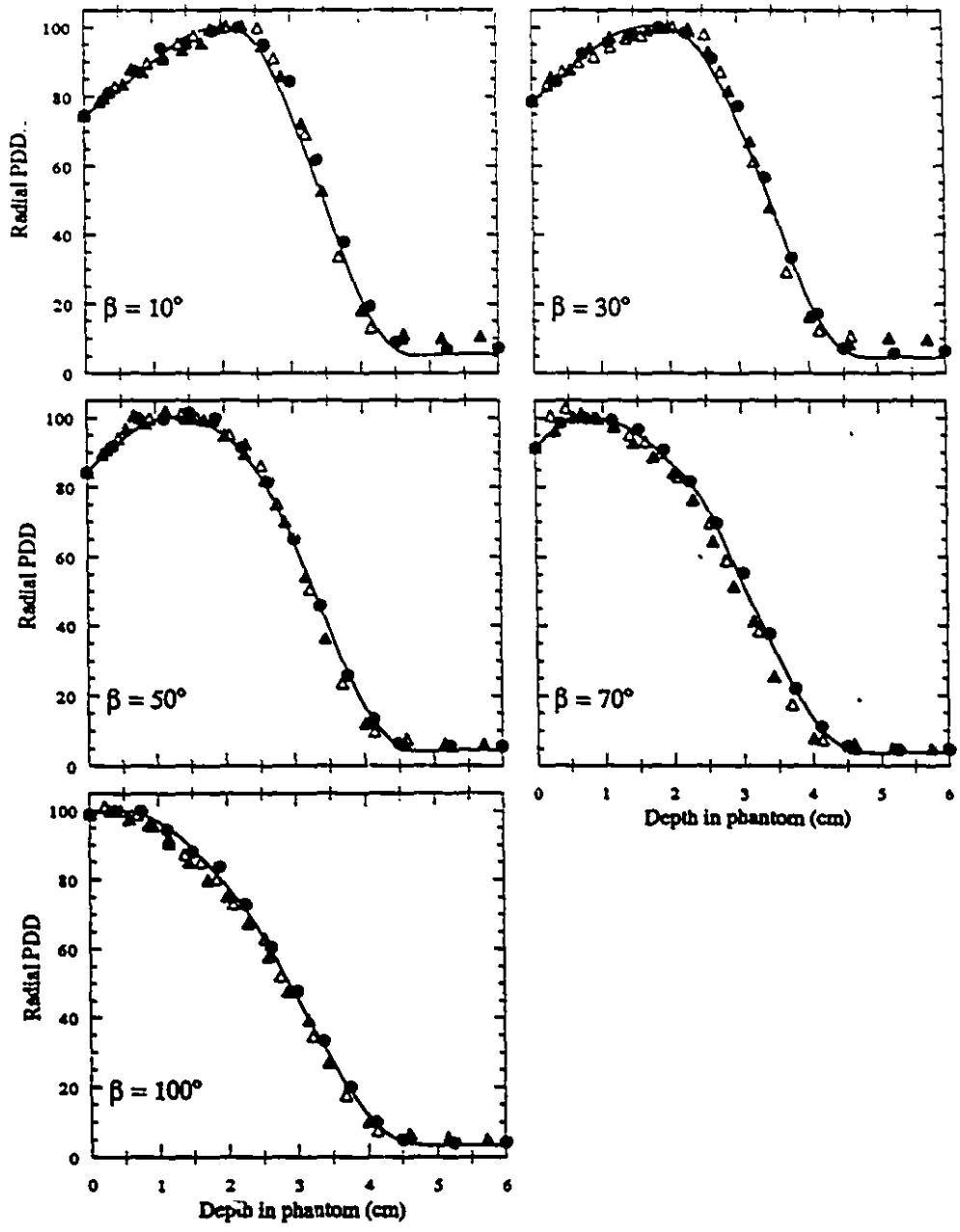

Figure 5.11 Radial percentage depth doses for the 9 MeV electron arc beam, calculated from measured data for the 12 MeV (solid circles), 15 MeV (solid triangles), and for 18 MeV (open triangles) electron arc beams, for various characteristic angles: (a) 10°, (b) 30°, (c) 50°, (d) 70°, and (e) 100°. Solid lines show measured radial percentage depth dose for the 9 MeV electron arc beam.

in order to obtain a better agreement between the calculated and measured data in the build-up region. Using the measured surface percent dose value $D'_s(E)$ for the beam with energy E, we introduce an empirical correction factor $f_{corr}(E)$ at depth d taken as a linear function ranging from $D'_s(E)/D_s(E)$ on the surface to 1 at the depth of d_{max}. The correction factor is then equal to:

$$f_{corr}(E) = \frac{D'_s}{D_s} + \frac{D_s - D'_s}{D_s} \frac{d}{d_{max}} \quad , \qquad (5.8)$$

where $D_s(E)$ is the surface percent dose calculated from Eq. (5.5) by taking $d = 0$. Beyond d_{max} the correction factor is equal to 1, i.e., it need not be applied.

Taking this empirical correction factor into account, we recalculate the radial percentage depth doses for the 9 MeV electron arc beams from the data for the 12 MeV, 15 MeV, and 18 MeV electron arc beams. The results are shown in Figures 5.12 (a) to (e). Now the agreement between the measured and the calculated data is excellent in the whole range of depths from the surface to the practical range of electrons. However, we should emphasize that this calculation is wrong for the isocentre dose because the isocentre depth is fixed and cannot be scaled by Eq. (5.6). As will be discussed below, the increase of the dose beyond the depth equal to the range of electrons is attributed to the bremsstrahlung tails of stationary electron beams superimposed at the isocentre. The depth of the increased dose is determined by the depth of isocentre only and is not related to the beam energy.

After we have determined the depth of dose maximum for a variety of electron arc beams with different energies, we can verify the validity of Eq. (5.5). To calculate $d_{max}(E)$ we need the values for physical range of stationary electron beams. They are shown in Table 5.1.

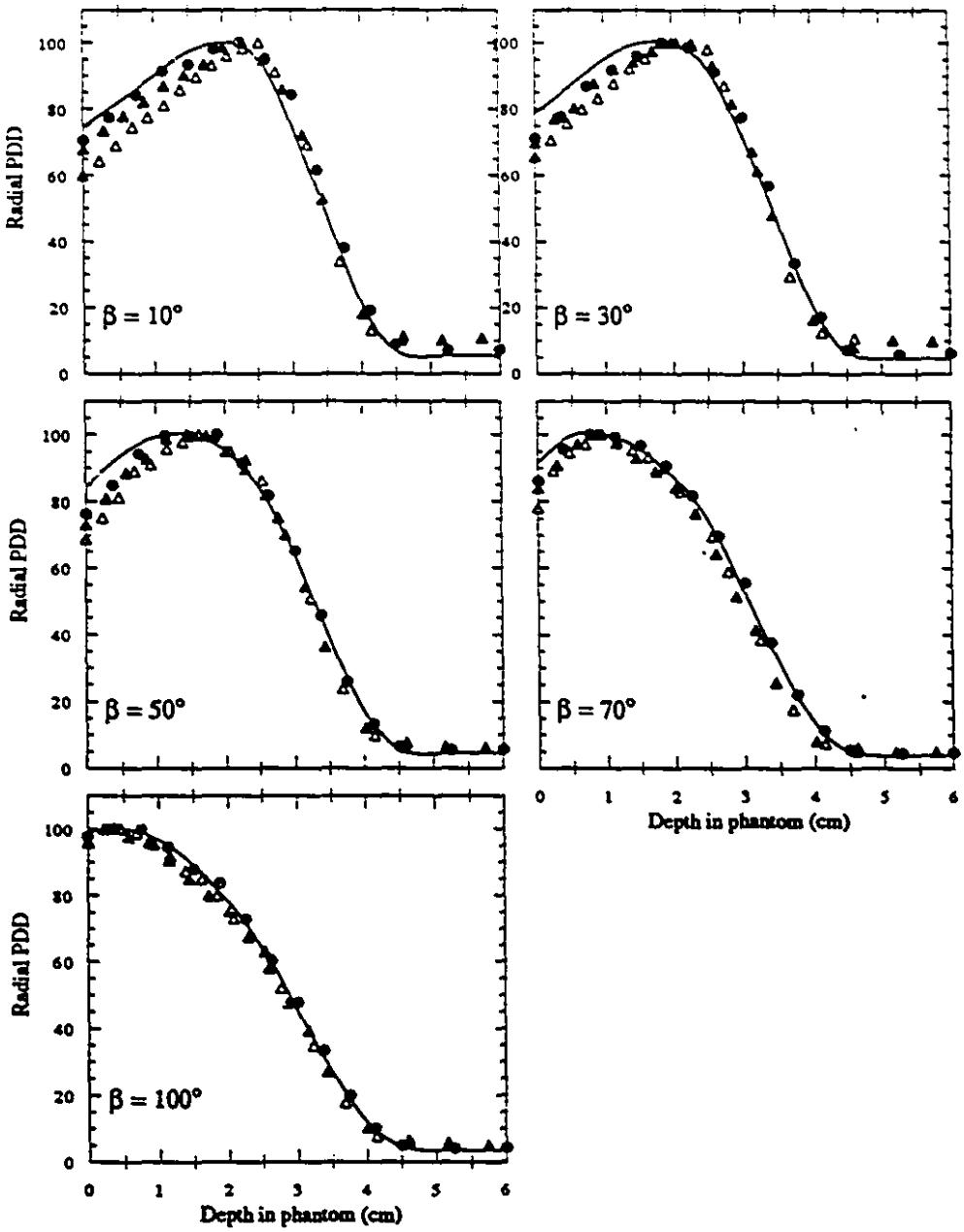

Figure 5.12 Calculated radial percentage depth doses including the correction factor of Eq. (5.8) for the 9 MeV electron arc beam, calculated from data for the 12 MeV (solid circles), 15 MeV (solid triangles), and for 18 MeV (open triangles) electron arc beams for various characteristic angles: (a) 10°, (b) 30°, (c) 50°, (d) 70°, and (e) 100°. Solid lines show the corresponding measured radial percentage depth doses for the 9 MeV electron arc beam.

E (MeV)	R_p (mm)
9	42
12	56
15	71
18	85

Table 5.1 Practical ranges (R_p) of clinical electron beams with nominal energy E available from the Clinac-18 linac. Data are taken from percentage depth dose curves [Fig. 4.2 (b) to (e)] using TG-25 protocol[19]. Field size 10×10 cm^2 has been used for all beams.

We have chosen $E_o = 9$ MeV to verify the validity of Eq. (5.7). A comparison between the measured and the calculated data for d_{max} (E) is shown in Fig. 5.13. We have found that Eq. (5.7) underestimates the depth of dose maximum for electron arc beams with higher energies by as much as 30% for the 18 MeV beam and for the small angles beta. At the first glance, this implies that our use of the Equations (5.5) to (5.7) for predicting the dose D(d,E) from the dose $D_o(d_o,E_o)$ has not been justified. However, close to the depth of dose maximum the dose is changing slowly with the depth and therefore the agreement between the measured and the calculated D(d,E) can be better understood.

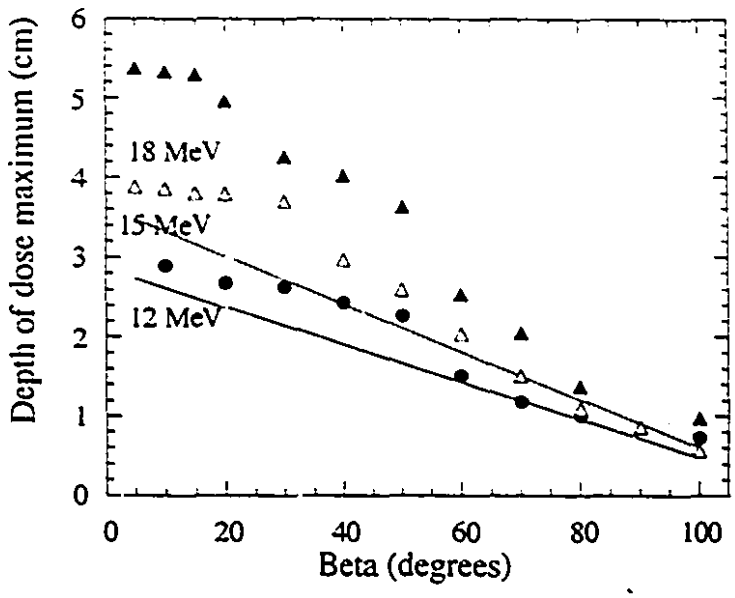

Figure 5.13 Comparison of measured and calculated values of d_{max} for electron arc beams with energies of 12 MeV, 15 MeV, and 18 MeV. Straight lines represent linear fits of calculated data for each energy and points represent the measured data from Fig. 5.7.

5.2.5. Surface dose

In electron arc therapy a high surface dose is often required for successful treatment. In addition to the treatment range R_{85}, the surface dose is an important parameter of choice to the radiation oncologist. The surface dose dependence on the angle β and on the nominal electron energy may be determined from the radial PDD measurements, and the results are shown in Fig. 5.14. Generally, for constant electron beam energy the surface dose increases with increasing β, and for a given angle β it decreases with increasing nominal energy. For small β the surface dose depends strongly on the nominal beam energy, however, for angles β larger than 60° the surface dose values for different electron energies tend to converge to the value of 100%. This latter finding can be explained by the oblique incidence of a large portion of the beam at large angles β. This is in agreement with

the observation that for large angles of incidence in stationary electron beams the d_{max} shifts toward the surface[12,20] thus bringing the surface percentage dose close to 100%.

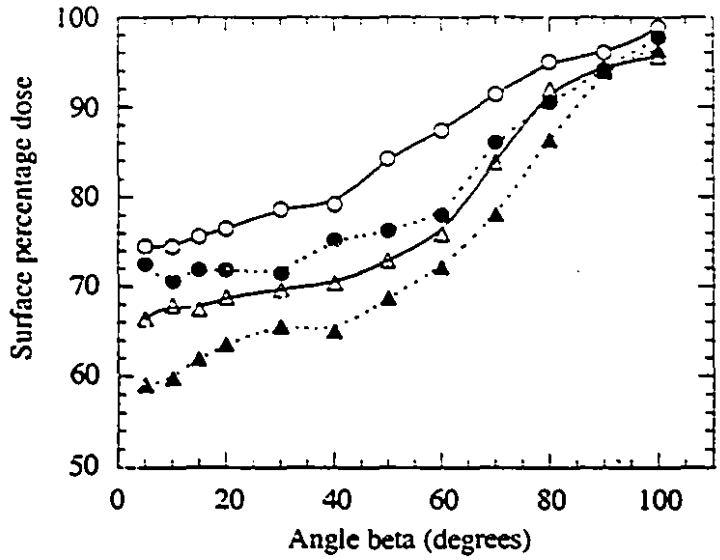

Figure 5.14 The surface percentage dose dependence on the angle β for various electron energies. Open circles, solid circles, open triangles, and solid triangles represent data for 9 MeV, 12 MeV, 15 MeV, and 18 MeV electron arc beams, respectively.

For the angle β equal to 100° the corresponding field width is 26 cm for an SAD of 85 cm, which is almost equal to the diameter of the phantom (30 cm). For the beam periphery the angle of incidence can be calculated from simple geometric relationship and it is equal to 60°. This assumption is quite conservative, because for the electron beam collimated only with X-ray collimators the beam profiles spread over their geometrically defined boundary, pronouncing the obliquity effect even more.

When the radiation oncologist prefers the dose distribution with a high surface dose, the electron arc irradiation with large angle β should be chosen. As it will be

discussed below, large β is also preferable in order to avoid high photon contamination dose at the isocentre.

5.3 Photon contamination of electron arc beams

In electron arc irradiation one is usually concerned with the dose distributions for the depths ranging from 0 (the surface) to R_p. Between d_{max} and R_p the depth dose is decreasing with an approximately constant gradient to a value of approximately 10% of the maximum dose (Figures 5.4 and 5.5). However, we must not ignore the fact that in an arc irradiation all the stationary beams are aimed toward the isocentre, and small contributions of the stationary beam dose at the depth of the isocentre can potentially add up to a significant and, for the patient, hazardous level. Therefore we have to address the photon contamination of electron arc beams and find a solution to obviate this problem.

From radial percentage depth dose measurements we can determine the dose at the isocentre. The isocentre percentage dose dependence on the angle β and on beam energy is shown in Fig. 5.15. The dose at the isocentre increases with decreasing β and the effect is quite pronounced for small angles β. For a fixed angle β the isocentre dose increases with increasing beam energy. This is not difficult to explain: as the β decreases, the field width w is becoming smaller (if the other geometric parameters are fixed), therefore a fewer number of stationary beams contribute to the dose at the depth of dose maximum. At the same time, contributions of all beams contribute to the isocentre dose. Although the position of the isocentre is to a large extent fixed by the patient geometry, the isocentre must be placed deep enough in order to assure only the photon contamination contributes to the isocentre dose, since any electron beam contribution to the dose at the isocentre depth would lead to sharp excessive dose at the isocentre. For $d_i > R_p$ the isocentre percentage dose is roughly inversely proportional to the β and proportional to the extent of the arc α.

The increase of the isocentre percent dose with increasing energy is expected since the bremsstrahlung contribution to the dose of a stationary electron beam also increases with the electron beam energy.

All our measurements were done for an arc angle α of 200°. For very small angle β (5°) and for high nominal energies of the electron arc beam (above 15 MeV) the isocentre dose reaches 50% of the maximum dose and for α larger a would be even greater. In clinical work this could be dangerous, especially when the isocentre coincides with a sensitive structure inside the patient (e.g., spinal cord). As shown in Fig. 5.15, the danger can be easily avoided using reasonably wide radiation fields with the angle β larger than 10° (this corresponds to the surface field width larger than 5 cm for an isocentre depth of 15 cm) for which the isocentre dose decreases rapidly to more acceptable levels.

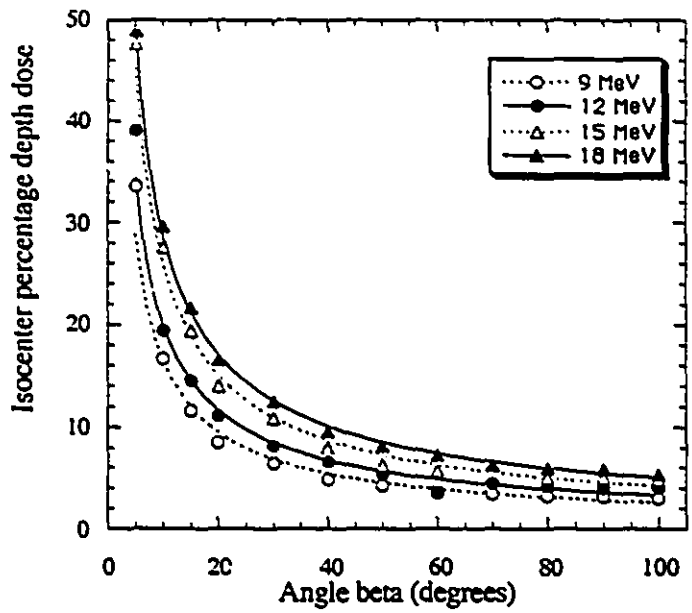

Figure 5.15 The isocentre percentage dose dependence on the angle β for the 9 MeV, 12 MeV, 15 MeV, and 18 MeV electron arc beams measured in polystyrene with d_i = 15 cm. Arc angle α = 200°, depth of isocentre is larger than the physical range of the electron beams in polystyrene.

5.4. Conclusions

Electron arc therapy is a technique of great importance in radiotherapy in treatment of superficial lesions following large curved surfaces. The approach developed at McGill University offers a choice of different beam parameters to a physician to achieve the most suitable dose distribution inside the target volume. The two most important parameters to consider clinically are the surface dose and the depth of the 85% percent isodose surface, and the bremsstrahlung contamination at the isocentre.

In this work we have extended the validity of the characteristic angle-beta concept to electron arc beams with nominal energies of 18 MeV. We have shown that the depth of the dose maximum as well as the radial depths of the 85% and 50% depth doses decrease linearly with angle β for all electron beam energies available on the Varian Clinac-18 linac. We have also verified the validity of the equation relating the depth dose distributions in electron arc beams with different energies for the depths beyond d_{max}. Furthermore, using a correction factor, we are currently able to calculate the radial depth-dose distributions for an arbitrary electron arc beam with nominal energy E from the depth dose data measured for a particular electron beam with a nominal energy of E_o.

We have also investigated the dependence of the surface dose and the isocentre dose on the angle β and on the nominal energy of the electron arc beam. For a fixed electron beam nominal energy the surface dose increases with increasing β and for a fixed angle β, the surface dose decreases with an increasing beam nominal energy.

The isocentre dose attributed to the photon contamination of the electron beam is proportional to the arc angle α and is inversely proportional to the characteristic angle β. For fixed α and β the isocentre dose increases with an increasing beam nominal energy.

5.5 References:

1. M.R. McKenzie, C.R. Freeman, M. Pla, J. Guerra, L. Souhami, C. Pla, E.B. Podgorsak, "Clinical experience with electron pseudoarc therapy", Br. J. Radiol. **66**, 234-240 (1993).
2. J. Becker, G. Weitzel, "New forms of moving radiation from a 15 MeV Siemens betatron", Strahlentherapie **101**, 180-190 (1956).
3. J. Rassow, "On the telecentric small-angle pendulum therapy with high electron energy betatron", Electromedica **1**, 1-6 (1972).
4. A.L. Boyer, G.D. Fullerton, J.G. Mira, "An electron beam pseudoarc technique for irradiation of large area of chest wall and other curved surfaces", Int. J. Radiat. Oncol. Biol. Phys. **8**, 1969-1974 (1982).
5. B.E. Bjarngard, G.T.Y. Chen, R.W. Pionter, G.K. Svensson, "Analysis of dose distribution in whole body superficial electron therapy", Int. J. Radiat. Oncol. Biol. Phys. **2**, 319-324 (1977).
6. F.M. Khan, G.D. Fullerton, J.M.-F. Lee, V.C. Moore, S.H. Levitt, "Physical aspect of electron-beam arc therapy", Radiology **124**, 497-500 (1977).
7. D.R. Ruegsegger, S.D. Leruđe, D. Lyle, "Electron-beam arc therapy using a high energy betatron", Radiology **133**, 483-489 (1979).
8. B.E. Blackburn and R. Moreland, "An improved method of electron arc therapy for chest wall irradiation", Int. J. Radiat. Oncol. Biol. Phys. **6**, 1373 (1980).
9. D.D. Leavitt, L.M. Peacock, F.A. Gibbs, J.A. Stewart, "Electron arc therapy: Physical measurement and treatment planning techniques", Int. J. Radiat. Oncol. Biol. Phys. **11**, 987-999 (1985).
10. D.D. Leavitt, J.R. Stewart, J.H. Moeller, W.L. Lee, G.A. Takach Jr., "Electron arc therapy: design, implementation and evaluation of a dynamic multi-vane collimator system", Int. J. Radiat. Oncol. Biol. Phys. **17**, 1089-1094 (1989).

11. D.D. Leavitt, J.R. Stewart, J.H. Moeller, L. Earley, "Optimization of electron arc therapy doses by multi-vane collimator control", Int. J. Radiat. Oncol. Biol. Phys. **16**, 489-496 (1989).

12. M. Pla, C. Pla, E.B. Podgorsak, "The influence of beam parameters on percentage depth dose in electron arc therapy", Med. Phys. **15**, 49-55 (1988).

13. M. Pla, E.B. Podgorsak, C.R. Freeman, L. Souhami, J. Guerra, "Physical aspects of the angle-β concept in electron arc therapy", Int. J. Radiat. Oncol. Biol. Phys. **20**, 1331-1339 (1991).

14. F.M. Khan, The physics of radiation therapy, 2nd edition, Williams & Wilkins, Maryland, U.S.A. (1994).

15. M. Pla, E.B. Podgorsak, C. Pla, "Electron dose rate and photon contamination in electron arc therapy", Med. Phys. **16**, 692-697 (1989).

16. K.R. Hogstrom, R.G. Kurup, A.S. Shiu, G. Starkschall, "A two-dimensional pencil beam algorithm for calculation of arc electron dose distributions", Phys. Med. Biol. **34**, 315-341 (1989).

17. Pierre Courteau, "Electron arc therapy dose calculation using the angle-β concept", McGill University, M.Sc. Thesis (1993).

18. M. Pla, E.B. Podgorsak, C. Pla, "The characteristic angle-β concept in electron arc therapy", Radiol. Oncol. **28**, 49-57 (1994).

19. F.M. Khan, K.P. Doppke, K.R. Hogstrom, G.J. Kutcher, R. Nath, S.C. Prasad, J.A. Purdy, M. Rosenfeld, B.L. Werner, "Clinical electron-beam dosimetry: Report of AAPM Radiation Therapy Committee Task Group No.25", Med.Phys. **18**, 73-109 (1991).

20. F.M. Khan, F.C. Deibel, A. Soleimani-Meigooni, "Obliquity correction for electron beams", Med. Phys. **12**, 749-753 (1985).

Chapter 6
Conclusions and future work

6.1 Conclusions

In this thesis we have examined the physical parameters of the electron arc irradiation technique, developed in 1986 at McGill University. Our investigations of dose distributions in electron arc therapy were based on thermoluminescent (TL) dosimetry techniques, and an extensive evaluation of these for use in electron beam dosimetry is provided in the thesis. All measurements were done with TLD-100 dosimeters in the form of $1 \times 1 \times 6$ mm^3 micro-rods. A batch of 30 dosimeters has been calibrated against 6 reference dosimeters. For the reference dosimeters the dose response and energy response relative to cobalt-60 beam have been determined and the dose response was found linear up to a dose of 200 cGy. The energy response of the TL dosimeters at d_{max} decreases with decreasing nominal energy of the electron beam. As long as the photon contamination fraction of the dose in a clinical electron beam is small, the energy response of the TL dosimeter for a given clinical electron beam is also decreasing with increasing depth and decreasing mean electron energy. Close to the depth equal to R_p the photon contamination fraction increases and the energy response starts to increase and attains the value of 1 at the depth equal to the physical range of electrons and beyond.

We have measured in a cylindrical polystyrene phantom the radial depth doses for electron arc beams for various angles β, for all nominal electron beam energies (9 MeV, 12 MeV, 15 MeV, and 18 MeV) available on our Clinac-18 linac. We have shown that the characteristic angle-β approach, previously shown[1] to be valid for the electron arc beams with the nominal energy of 9 MeV, 12 MeV, and 15 MeV, is also appropriate for electron arc beams with the nominal energy of 18 MeV.

We have found that the depth of dose maximum, the depth of the 85% depth dose, and the depth of the 50% depth dose decrease linearly with an increasing angle β for a fixed electron beam energy. For various nominal energies of the electron beam, the slope of the d_{max} vs. β curve increases significantly with increasing energy, while the increase in the slope is less pronounced for the depth of the 85% depth dose vs. β curve, and the effect is the smallest for the depth of the 50% depth dose vs. β curve.

We have also investigated the dependence of the surface dose and the isocentre dose on the angle β and on the nominal energy of the electron arc beam. For a constant electron beam nominal energy the surface dose increases with increasing β and for a fixed angle β, the surface dose decreases with an increasing beam nominal energy.

The isocentre dose attributed to the bremsstrahlung contamination of the electron beam is proportional to the extent of arc angle α and is inversely proportional to the characteristic angle β. For fixed α and β the isocentre dose increases with an increasing beam nominal energy.

6.2 Future work

A preliminary study by Pla et al.[1] indicated that the characteristic angle-beta concept could be extended to nonhomogeneous materials using a simple density scaling of the radiological path to determine the dose at arbitrary points. Percentage depth doses were measured in a composite cylindrical phantom consisting of a wood cylinder (density

$\rho = 0.3$ g/cm^3) surrounded by a polystyrene tube. The radial percentage depth doses were calculated with the following empirical relationship:

$$D(d,\rho) = D(d_o,\rho_o)\frac{\beta\{d_i - d_{max}(\rho)\}}{\beta\{d_i - d_{max}(\rho_o)\}} \quad , \tag{6.1}$$

where

$$d_{max}(\rho) = [d_{max}(\rho_o) - t]\frac{\rho}{\rho_o} + t \quad , \tag{6.2}$$

and

$$d = [d_o - t]\frac{\rho}{\rho_o} + t \quad ; \tag{6.3}$$

Here t stands for the thickness of the polystyrene tube of density ρ_o ; d and d_o are depths in the phantom. Equations (6.1) to (6.3) describe a simple scaling of depth for materials with various densities.

To confirm the validity of this relatively simple concept a thorough investigation of electron arc beam percentage depth doses in a variety of composite phantoms is required. This would in turn improve the accuracy of the treatment planning algorithms for electron pseudoarc beam for an arbitrary density distribution inside the patient contour. This is especially important in chest wall irradiations where the densities range from very low values (lungs) to high values (hard bone). Adequate density information may be obtained from CT data but currently cannot be used reliably in treatment planning algorithms dealing with electron arc therapy.

With installation of a new Clinac 2300-C/D linac at the Montreal General Hospital a new interesting field arises, as the linac is capable of continuous electron arc therapy. A thorough investigation would indicate whether or not the characteristic angle-β concept may be implemented to continuous arc irradiation. We certainly believe that the characteristic

angle-β concept could be relatively easily expanded from the pseudoarc approach to the continuous electron arc approach. However, this contention will have to be verified by experimental work in the future.

6.3 Reference:

1. M. Pla, E.B. Podgorsak, C. Pla, "The characteristic angle-β concept in electron arc therapy", Radiol. Oncol. 28, 49-57 (1994).

List of figures

List of tables

Bibliography

(numbers in parentheses indicate the pages in text where the references are referred to)

1. F.H. Attix, "Determination of A_{ion} and P_{ion} in the new AAPM Radiotherapy dosimetry protocol", Med. Phys. 11, 714-716, 1984. ..... (26)

2. J. Becker, G. Weitzel, "New forms of moving radiation from a 15 MeV Siemens betatron", Strahlentherapie 101, 180-190, 1956. ..... (70)

3. A.F. Bielajew and D.W.O. Rogers, "PRESTA: the parameter reduced electron-step transport algorithm for electron Monte Carlo transport", Nucl. Instrum. Methods B 18, 165-181, 1987. ..... (62)

4. B.E. Bjarngard, G.T.Y. Chen, R.W. Pionter, G.K. Svensson, "Analysis of dose distribution in whole body superficial electron therapy", Int. J. Radiat. Oncol. Biol. Phys. 2, 319-324, 1977. ..... (71)

5. B.E. Blackburn and R. Moreland, "An improved method of electron arc therapy for chest wall irradiation", Int. J. Radiat. Oncol. Biol. Phys. 6, 1373, 1980. ..... (72)

6. A.L. Boyer, G.D. Fullerton, J.G. Mira, "An electron beam pseudoarc technique for irradiation of large area of chest wall and other curved surfaces", Int. J. Radiat. Oncol. Biol. Phys. 8, 1969-1974, 1982. ..... (71)

7. A.Brahme, B.Lind, P.Nafstadius, "Radiotherapeutic computed tomography with scanned photon beams", Int. J. Radiat. Oncol. Biol. Phys. 13, 95-101, 1987. ..... (21)

8. T.E. Burlin, "A general theory of cavity ionization", Br. J. Radiol., 39, 727-734, 1966. ..... (54)

9. J.R. Cameron, N. Suntharalingam, G.N. Kenney, "Thermoluminescent Dosimetry", The University of Wisconsin Press, Madison, Milwaukee, and London, 1968. ..... (31, 40)

10. C. Constantinou, F.H. Attix, B.R. Paliwal, "A solid water phantom material for radiotherapy X-ray and γ-ray beam calibrations" , Med.Phys. 9, 436-441, 1982 ..... (24)

11. Pierre Courteau, "Electron arc therapy dose calculation using the angle-β concept" , McGill University, M.Sc. Thesis, 1993. ..... (80)

12. R.D. Evans, "The atomic nucleus", McGraw-Hill, New York, 1958. ..... (9)

13. K.R. Hogstrom, R.G. Kurup, A.S. Shiu, G. Starkschall, "A two-dimensional pencil beam algorithm for calculation of arc electron dose distributions" , Phys. Med. Biol. 34, 315-341, 1989. ..... (80)

14. J.G. Holt, G.R. Edelstein, T.E. Clark, "Energy Dependence of the Response of Lithium Fluoride TLD Rods in High Energy Electron Fields", Phys. Med. Biol. 20, 559-570, 1975. ..... (54)

15. The Hospital Physicists' Association: "Practical aspects of Thermoluminescence Dosimetry", Conference Report Series- 43, 1984. ..... (30)

16. International Atomic Energy Agency, "Absorbed Dose Determination in Photon and Electron Beams: An International Code of Practice", Technical report series No. 277, Vienna, 1987. ..... (27)

17. H.E. Johns and J.R. Cunningham, "The Physics of Radiology", 4th edition, Charles C. Thomas, Springfield, Illinois. 1984. ..... (8, 14, 24)

18. F.M. Khan, The physics of radiation therapy, 2nd edition, Williams & Wilkins, Maryland, U.S.A., 1994. ..... (2, 14, 78)

19. F.M. Khan, F.C. Deibel, A. Soleimani-Meigooni, "Obliquity correction for electron beams", Med. Phys. 12, 749-753, 1985. ..... (96)

20. F.M. Khan, K.P. Doppke, K.R. Hogstrom, G.J. Kutcher, R. Nath, S.C. Prasad, J.A. Purdy, M. Rosenfeld, B.L. Werner, "Clinical electron-beam dosimetry: Report of AAPM Radiation Therapy Committee Task Group No.25", Med. Phys. 18, 73-109, 1991. ..... (7, 24, 26, 55, 60, 92)

21. F.M. Khan, G.D. Fullerton, J.M.-F. Lee, V.C. Moore, S.H. Levitt, "Physical aspect of electron-beam arc therapy", Radiology 124, 497-500, 1977. ..... (71)

22. S.C. Klevenhagen, "Physics and dosimetry of therapy electron beams", Medical Physics Publishing, Madison, Wisconsin, 1993. ..... (27, 28)

23. D.D. Leavitt, L.M. Peacock, F.A. Gibbs, J.A. Stewart, "Electron arc therapy: Physical measurement and treatment planning techniques", Int. J. Radiat. Oncol. Biol. Phys. **11**, 987-999, 1985. ..... (72, 80)

24. D.D. Leavitt, J.R. Stewart, J.H. Moeller, W.L. Lee, G.A. Takach Jr., "Electron arc therapy: design, implementation and evaluation of a dynamic multi-vane collimator system", Int. J. Radiat. Oncol. Biol. Phys. **17**, 1089-1094, 1989. ..... (72)

25. D.D. Leavitt, J.R. Stewart, J.H. Moeller, L. Earley, "Optimization of electron arc therapy doses by multi-vane collimator control", Int. J. Radiat. Oncol. Biol. Phys. **16**, 489-496, 1989. ..... (72)

26. M.R. McKenzie, C.R. Freeman, M. Pla, J. Guerra, L. Souhami, C. Pla, E.B. Podgorsak, "Clinical experience with electron pseudoarc therapy", Br. J. Radiol. **66**, 234-240, 1993..... (70)

27. A.F. McKinlay, "Thermoluminescence Dosimetry" , Medical Physics Handbooks 5, Adam Hilger Ltd, Bristol, UK, 1981. ..... (30, 34, 36, 37, 40, 43, 44)

28. W.R. Nelson, H. Hirayama, D.W.O. Rogers, The EGS4 code system, SLAC report **265**, 1985. ..... (62)

29. B.R. Paliwal and P.R. Almond, "Applications of Cavity Theories for Electrons to LiF Dosemeters", Phys. Med. Biol. **20**, 547-558, 1975. ..... (54, 58, 59)

30. C. Pla and E.B. Podgorsak, "A computerized TLD system", Med. Phys. **10**, 462-466, 1983. ..... (38, 40)

31. M. Pla, C. Pla, E.B. Podgorsak, "The influence of beam parameters on percentage depth dose in electron arc therapy", Med. Phys. **15**, 49-55, 1988. ..... (72, 74, 96)

32. M. Pla, E.B. Podgorsak, C.R. Freeman, L. Souhami, J. Guerra, "Physical aspects of the angle-β concept in electron arc therapy", Int. J. Radiat. Oncol. Biol. Phys. **20**, 1331-1339, 1991. ..... (10, 72, 75, 76)

33. M. Pla, E.B. Podgorsak, C. Pla, "Electron dose rate and photon contamination in electron arc therapy" , Med. Phys. **16**, 692-697, 1989. ..... (78, 79)

34. M. Pla, E.B. Podgorsak, C. Pla, "The characteristic angle-β concept in electron arc therapy", Radiol. Oncol. **28** 49-57, 1994. ..... (10, 89, 102, 103)

35. J. Rassow, "On the telecentric small-angle pendulum therapy with high electron energy betatron", Electromedica **1**, 1-6, 1972. ..... (70)

36. "Report of calibration: $^{90}Sr + ^{90}Y$ Beta-particle Ophthalmic Applicator Amersham Model SIA.20 S/N 1026ML", United States Department of Commerce, National Institute of Standards and Technology, Gaithersburg, Maryland, 1994. ..... (23)

37. D.R. Ruegsegger, S.D. Lerude, D. Lyle, "Electron-beam arc therapy using a high energy betatron", Radiology **133**, 483-489, 1979. ..... (71)

38. S.C. Saris, G.R. Solares, D.E. Wazer, G. Cano, S.E. Kerley, M.A. Joyce, L.S. Adelman, O.K. Harling, H. Madoc-Jones, R.G. Zamenhof, "Boron neutron capture therapy for murine malignant gliomas" , Cancer Research 52, 4672-4677 (1992). ..... (9)

39. J.M. Sisterson, "Clinical use of protons and ion beams from a world-wide perspective", Nucl. Instrum. Meth. **B 10/11**, 1350-1352 (1989). ..... (8)

40. N. Suntharalingham and J.R. Cameron, "The response of LiF to high energy electron beams", Ann. N. Y. Acad. Sci. **161** 77-83 (1967). ..... (54)

41. Task Group 21, Radiation Therapy Committee, "A protocol for the determination of absorbed dose from high-energy photon and electron beams" , Med. Phys. **10**, 741-771 (1983). ..... (26)